CERN/SPSC/78-06
SPSC/P92
30 January 1978

C replacema

PROPOSAL

A 4π SOLID ANGLE DETECTOR FOR THE SPS USED AS A PROTON-ANTIPROTON COLLIDER AT A CENTRE OF MASS ENERGY OF 540 GeV

A. Astbury[8], B. Aubert[2], A. Benvenuti[4], D. Bugg[6], A. Bussière[2], Ph. Catz[2], S. Cittolin[4], D. Cline*)[4], M. Corden[3], J. Colas[2], M. Della Negra[2], L. Dobrzynski[5], J. Dowell[3], K. Eggert[1], E. Eisenhandler[6], B. Equer[5], H. Faissner[1], G. Fontaine[5], S.Y. Fung[7], J. Garvey[3], C. Ghesquière[5], W.R. Gibson[6], A. Grant[4], T. Hansl[1], H. Hoffmann[4], R.J. Homer[3], M. Jobes[3], P. Kalmus[6], I. Kenyon[3], A. Kernan[7], F. Lacava**)[4], J.Ph. Laugier[9], A. Leveque[9], D. Linglin[2], J. Mallet[9], T. McMahon[3], F. Muller[4], A. Norton[4], R.T. Poe[7], E. Radermacher[1], H. Reithler[1], A. Robertson[8], C. Rubbia†)[4], B. Sadoulet[4], G. Salvini**)[4], T. Shah[8], C. Sutton[8], M. Spiro[9], K. Sumorok[3], P. Watkins[3], J. Wilson[3], R. Wilson***)[4]

III Physikalisches Institut, Technische Hochschule Aachen, Germany.[1]
LAPP (IN2-P3) , Annecy, France.[2]
University of Birmingham, U.K.[3]
CERN, Geneva, Switzerland.[4]
Laboratoire de Physique Corpusculaire, College de France, Paris.[5]
Queen Mary College, London, U.K.[6]
University of California, Riverside, California, USA.[7]
Rutherford Laboratory, Chilton, Didcot, Oxon, U.K.[8]
Centre d'Etudes Nucléaires, Saclay, France.[9]

(Aachen-Annecy-Birmingham-CERN-College de France-Queen Mary College-Riverside-Rutherford-Saclay Collaboration)

---

*) Visitor from University of Wisconsin, Madison, Wisconsin, USA.

**) Visitor from University of Roma, INFN Roma, Italy.

***) Visitor from Harvard University, Cambridge, Mass., USA.

†) Spokesman.

TABLE OF CONTENTS

TABLE OF CONTENTS (Cont'd)

TABLE OF CONTENTS (Cont'd)

1. INTRODUCTION

1.1. PREFACE. Early in 1976 it had been pointed out[1] that the main accelerator ring of the SPS could be transformed into a proton-antiproton colliding beam device capable of reaching a centre of mass energy of 2 x 270 GeV and eventually 2 x 400 GeV. On purely technical grounds the scheme cannot compete with entirely new projects; still it would offer a peak luminosity which is only a few times smaller than that of the ISR and threfore open up the possibilities of an early exploration of several crucial issues; such as for instance, the existence of weak intermediate bosons and of the spectacular new hadronic phenomena hinted at by cosmic-ray experiments.

Two working groups were set-up at CERN in April of the same year having in mind to examine the technical feasibility and the physics potentials of the scheme. The conclusions of the groups were presented at an Open Meeting on Nov. 24, 1976 and are contained in a report[2]. As a consequence of these recommendations three distinct activities have begun at CERN. The first one, is directed towards the realization of the antiproton source; a second one to study experimentally the stochastic and electron cooling needed in order to achieve the required luminosity and finally a third group has concentrated on the physics requirements and on the feasibility of a general purpose detector. A first workshop was held at CERN in the period March 28 - 2nd April 1977 and a second in the period July 11 - 18. A third final meeting has taken place in October. This systematic work has prompted over 50 reports, which have been published as '$p\bar{p}$-Notes' and several other scientific reports . Final conclusions have been presented at an open meeting Nov. 11, 1977.

The present proposal is the direct result of these studies. Several of the proponents have been with this project for at least two years and have an active role in the cooling experiments (ICE) and in the design of the antiproton facility. We believe that our close contact with the accelerator group has been very beneficial and it will continue

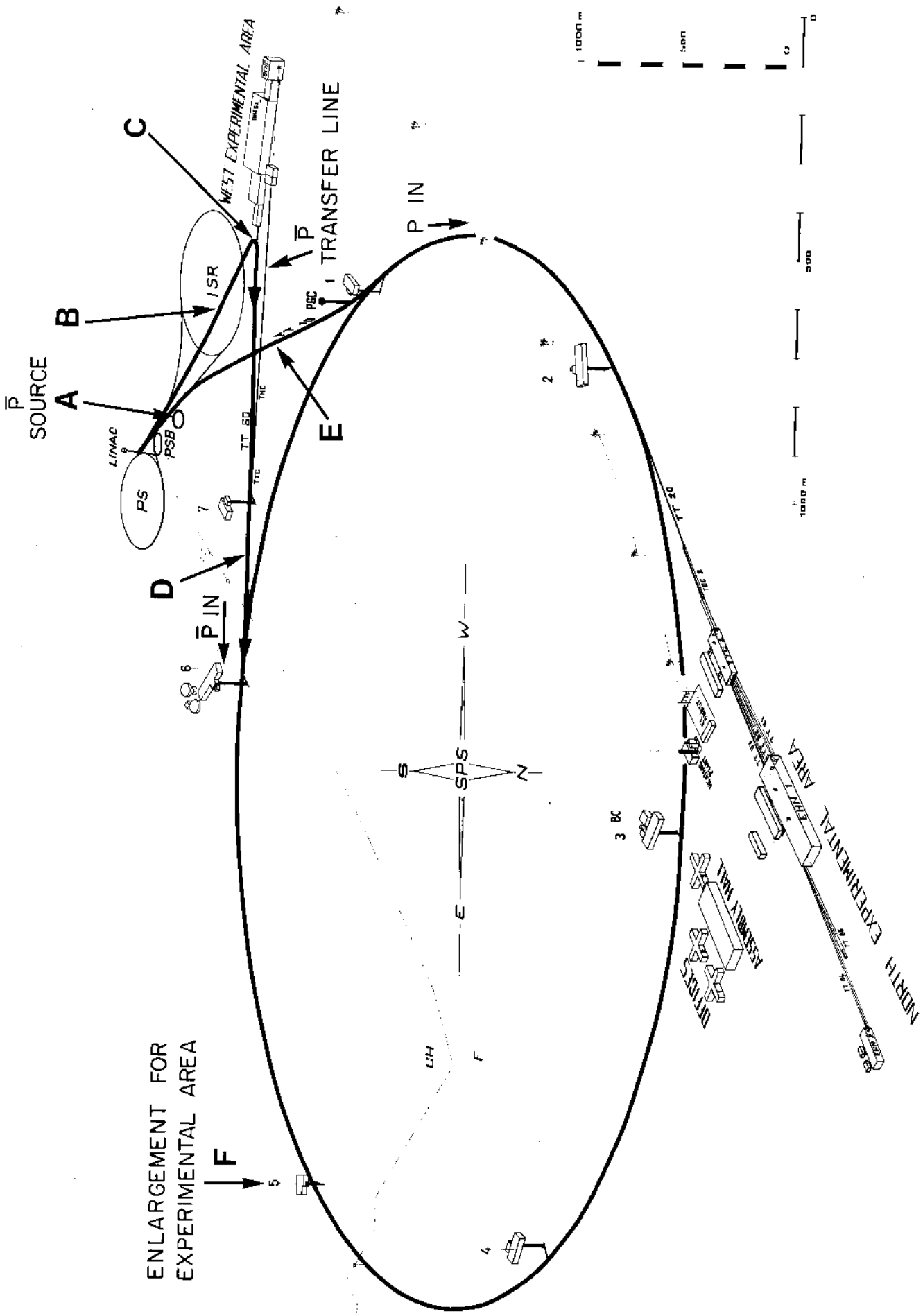

Figure 1.1. General Lay-out of the p-$\bar{p}$ Collider.

to be important especially during the initial phase of running-in of the experimental programme.

1.2. WORKING PRINCIPLE AND EXPECTED PERFORMANCE. We shall briefly outline the general scheme of operation of the SPS as a $p\bar{p}$ collider. For technical points and a more detailed discussion we shall refer to the report of S. Van der Meer group[3]. Figure 1.1. shows a sketch of the SPS. Antiprotons of about 3.5 GeV are produced with 26.5 GeV/c protons from the PS and stacked in a specially designed $\bar{p}$-accumulator ring (A) (block letters refer to Fig. 1.1). When a sufficient number of particles ($N_{\bar{p}} \simeq 6 \times 10^{11}$) has been accumulated and its phase space has been suitably compressed by cooling techniques, antiprotons are extracted in the form of five bunches which travel along the existing tunnel (B) between the PS and the West Experimental Area. At the crossover (C) between this tunnel and TT60 (the extraction line from the SPS) antiprotons are sharply bent by almost 170° and they find their way to the SPS through the standard proton extraction line (D) operated at appropriately reduced current. In this way, five equidistant $\bar{p}$ bunches are stored inside the SPS with the nominal momentum of 3.5 GeV/c. Particles are then accelerated to 15 GeV/c with the help of additional RF cavities to cover the extended frequency range. Five proton bunches are injected at the nominal injection energy from the PS through the standard line TT10 (E) and proton and antiproton bunches are simultaneously accelerated with the main RF system to 270 GeV, energy at which the SPS is held for the duration of the run. Initially a luminosity lifetime of a few hours is anticipated[4]. In a second phase with some improvements of the vacuum and eventually of the RF system it is hoped that the lifetime could reach many hours.

The experiment will be located in one of the long straight sections. We propose to use LSS5 (F) since it is the closest to the surface and it is not occupied by major accelerator components. The luminosity will be increased by acting on the betatron functions around the collision point. This is realised by adding focussing elements[5] which are

energised only after acceleration. An increase of about forty times in the luminosity is anticipated.

The luminosity is easily estimated[6] from standard proton and antiproton emittances:

$$L = 1.43 \times 10^{7} \times N_p \times N_{\bar{p}}/n \qquad cm^{-2}\ sec^{-1}$$

where n is the number of (identical) bunches, N_p and $N_{\bar{p}}$ are respectively the total number of protons and antiprotons. Setting $N_p = N_{\bar{p}} = 6 \times 10^{11}$ and $n = 5$ we get $L = 1.0 \times 10^{30}\ cm^{-2}\ sec^{-1}$. Tune shifts and bunch-bunch luminosities are shown in Fig. 1.2. We remark

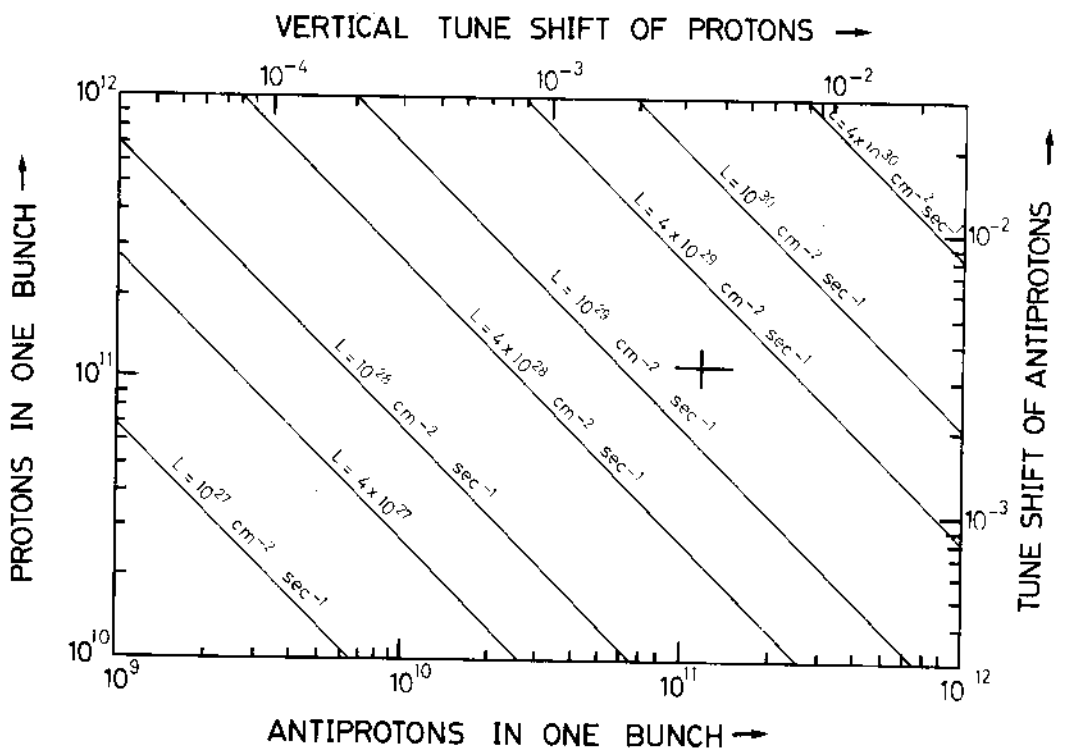

Figure 1.2. Bunch-bunch luminosities and tune shifts of $E_p = E_{\bar{p}} = 270$ GeV and standard emittances[6].

(+ indicates our setting)

that for $\sigma_{tot} \simeq 50$ mb the interaction rate is $N = 1.0 \times 10^{30} \times 5 \times 10^{-26} = 5 \times 10^{4}$ int/sec and there is about 23% probability of

Table I.1. Parameters of SPS used as a $p\bar{p}$-collider and of relevance to the detector design.

Nominal energy	E_o	270 + 270	GeV
Equivalent accelerator energy	E_{eq}	160	TeV
Total number of particles/beam	$N_p, N_{\bar{p}}$	6×10^{11} (4 mA)	
Number of bunches filled, each beam	n_b	5 (6)	
Time separation between bunches	Δt	4.6(3.8)	μs
Luminosity, peak with low-β	L_o	$1.0 \times 10^{30} cm^{-2}$	sec^{-1}
Beam-beam tune shift (max, at $L_o = 10^{30}$)	ΔQ	$4.8\ 10^{-3}$	
Interaction probability at each crossing of two bunches:			
(i) beam-beam (σ_{tot} = 50 mb)	P_{bb}	0.23	
(ii) beam-gas over 50 m at $P = 10^{-10}$ Torr	P_{bg}	1.4×10^{-3}	
Total free length of low-β insertion	l_f	± 14	m
Size of diamond, at 270 GeV and nominal emittances (s.d):			
(i) vertical	σ_v	0.08	mm
(ii) horizontal	σ_x	0.336	mm
(iii) length	l_b	∿ 30	cm
Luminosity lifetime due to gas, at $P_{av} = 2 \times 10^{-9}$ Torr	τ_e	8	hours
Momentum spread, each beam	$\Delta p/p$	5×10^{-4}	

interaction at each bunch crossing.

A luminosity of $\sim 10^{30}$ cm^{-2} sec^{-1} is required in order to test predictions of Unified Gauge Theories. However a first phase with a much lower luminosity is highly significant since we could perform a systematic study of the basic hadronic phenomena around 0.6 TeV in the centre of mass. This initial phase is very fundamental since it would test extrapolations of the main ISR/FNAL discoveries (large p_T phenomena, jet structure, shrinking, scaling and so on) and the extraordinary indications of cosmic ray experiments which hint the onset of a new hadronic threshold at about 100 TeV on a stationary target, or equivalently 500 GeV in the centre of mass. For instance even for a luminosity as low as L = 10^{27} cm^{-2} sec^{-1} our detecting apparatus could collect about 50 events/sec or equivalently 150,000 events/hour in a region in which cosmic rays have so far provided a handful of only partially reconstructed events.

A list of relevant parameters is given in Table 1.1.

2. PHYSICS OBJECTIVES

2.1. INTRODUCTION. There are several considerations, both theoretical and experimental which substantiate our strong belief that new and fundamental phenomena will emerge from experiments with energies of order 1 TeV in the centre of mass. They are based on new and fundamental progress in theoretical understanding, extrapolation of existing ISR, FNAL and SPS results and the observations of cosmic ray experiments.

Gauge theories, the discoveries of neutral currents and of the rising neutrino cross-section open the perspective of unification between weak and e.m. interactions. This possibility rests on the existence of intermediate vector bosons in the 40 to 150 GeV mass range which are well within the capabilities of the detector presently proposed.

The observation of J/ψ and of Υ indicate the presence of massive quarks associated with new quantum numbers. If even more massive quarks exist in nature, there should also exist narrow vector mesons analogous to the ψ and Υ, decaying into lepton pairs with large branching ratios. For

a reasonable mass resolution the peak would be above the Drell-Yan continuum and the cross-section be observable for reasonably large masses.

There is considerable evidence from cosmic ray experiments indicating the onset of new phenomena in hadron interactions. The appearance of unusual events above 100 TeV incident particles in the laboratory and the observation of anomalous development of air showers above the same energies, suggests some kind of threshold in hadronic interactions[7].

Another challenging possibility is a search for fractionally charged quarks. Overwhelming evidence favours the existence of fractionally charged constituents inside the hadrons. Absence of direct production suggests the existence of a confinement mechanism (bag). It is not known, but it appears plausible that at very high energies the 'bag' could sometimes be broken, thus liberating the elementary constituents.

All these expectations represent an impressive and coherent justification of the considerable interest of this new energy range. On the other hand it is clear that our detector will carry out a first systematic exploration in a field which is almost completely unknown and which must be tackled on a broad and unbiased base keeping sensitivity towards entirely new facts and surprises.

In the following, a short overall review is given of some of the physics potentials of the present proposal. We shall try to classify them according to present knowledge and in the way they have guided us in the design of the apparatus.

2.2. SEARCH FOR THE INTERMEDIATE VECTOR BOSONS. The most direct way to test the current theory of weak interactions is to search for the W-mesons whose coupling to fermions is responsible for the weak force[8]. Their masses must be large, since weak interactions so far can be described in terms of local four fermion interactions[9]. From the observation of neutral currents[10] it is concluded that there must exist a neutral component, a W^o.

Even if we had no idea of what masses to expect, the opening up of the new kinematic range offered by the $p-\bar{p}$ collider would make the search for W an important objective. Current theoretical ideas

establish a close connection between W-mesons and the photon and give to all of them a comparable intrinsic coupling strength. This leads to the mass estimate:

$$m_W \simeq (e^2/G_F)^{\frac{1}{2}} \simeq 100 \text{ GeV}/c^2$$

where e is the elementary charge and G_F the Fermi constant.

More specific theories allow detailed predictions. As an example the Weinberg-Salam model[11] gives masses as a function of an additional parameter $\sin^2\theta_W$, which is known from neutrino experiments:

$$m_{W^\pm} \simeq 60 \text{ GeV}/c^2 \qquad m_{W^0} \simeq 80 \text{ GeV}/c^2$$

which are outside the reach of the presently planned generation of e^+e^- Storage Rings (PEP and PETRA).

More general models of the same class predict a larger number of W mesons[12], in the same mass range as the W-S model. It is therefore evident that the presence or absence of W mesons in this mass range is of considerable importance.

The W cross-section in $p\bar{p}$ collisions is derived using basic and simple assumptions. There is now very strong support for the notion of point-like constituents in the hadron, obtained from lepton-hadron scattering and very high energy neutrino experiments. The experimental detection of weak interaction processes in hadronic collisions almost certainly involves quark-antiquark annihilation very much like e^+e^- collisions.

In order to estimate the cross-sections in $p\bar{p}$ collisions, the structure functions of partons must be known. Neutrino and charged lepton scattering experiments[9] provide the necessary structure functions and have set limits (> 20 GeV) on any non-locality in the parton form factor. The main difference with respect to e^+e^- annihilation is that now the kinematics is largely smeared out by the internal motion of the q's and $\bar{q}$'s.

Calculations on the production cross-sections have been reported

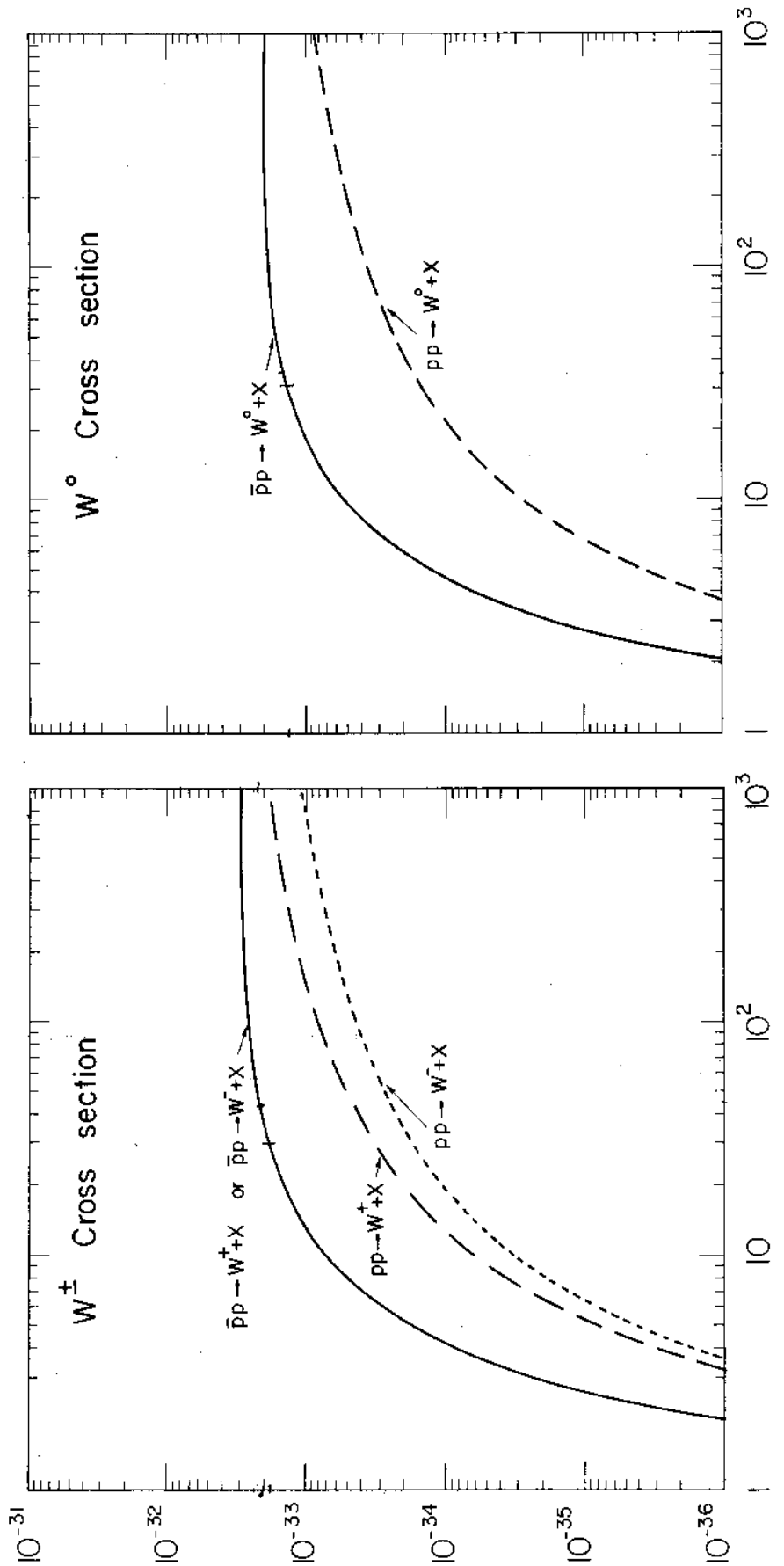

Figure 2.1a. $W^{\pm}$ production cross-section in $p\bar{p}$ collisions from quark-parton model as a function of the mass M. $\sqrt{s}$ is the centre of mass energy.

Figure 2.1b. The same as Figure 2.1a, except for W^{o} production.

by several authors[13]. They usually invoke parton-antiparton annihilation, scaling and CVC to relate the Drell-Yan process to the W-production. Some corrections may be required because of scaling deviations due for instance to asymptotic freedom. These effects have been considered[14] and found relatively unimportant at least for $M_W \leq 100$ GeV.

Cross-sections are summarized in Fig. 2.1a and 2.1b. Expectations give a total cross-section of about 5×10^{-33} cm^2 for $M_{W^\pm} \lesssim 100$ GeV. We would like to stress that the estimates for $p\bar{p}$ are more reliable than those for pp since the former involve mostly valence quarks which have been accurately investigated in deep inelastic lepton scattering experiments.

The search of these bosons requires an unambiguous experimental signature. Leptonic decay branching ratios could be related by CVC to the value of R measured in e^+e^- annihilation at an energy equal to the mass of the W^o. We can either extrapolate R or use the Weinberg-Salam model. It is plausible that the result should be approximately the same in any non exotic model since it depends mainly on the number of possible quark and leptonic final states. (Quarks are counted three times because of colour and with appropriate allowance being made for the Cabibbo angle). For the branching ratios we take the following values[15]:

$$B(W^\pm \to e^\pm + \nu) = 0.12 \qquad B(W^o \to e^+ + e^-) = 0.05$$

Partial widths in the leptonic channels estimated by standard graphs and the value of the Fermi constant[15] are:

$$\Gamma(W^\pm \to e^\pm + \nu) = 140 \text{ MeV}$$
$$\Gamma(W^0 \to e^+ + e^-) = 60 \text{ MeV} \qquad (\sin^2 \theta_W = 0.3)$$

Combining partial widths and branching ratios we get total widths, which are relatively large and at least in the case of W^o accessible to experimental observation:

$$\Gamma(W^\pm \to \text{all}) = 1.2 \text{ GeV}/c^2 \qquad \Gamma(W^o \to \text{all}) = 1.2 \text{ GeV}/c^2$$

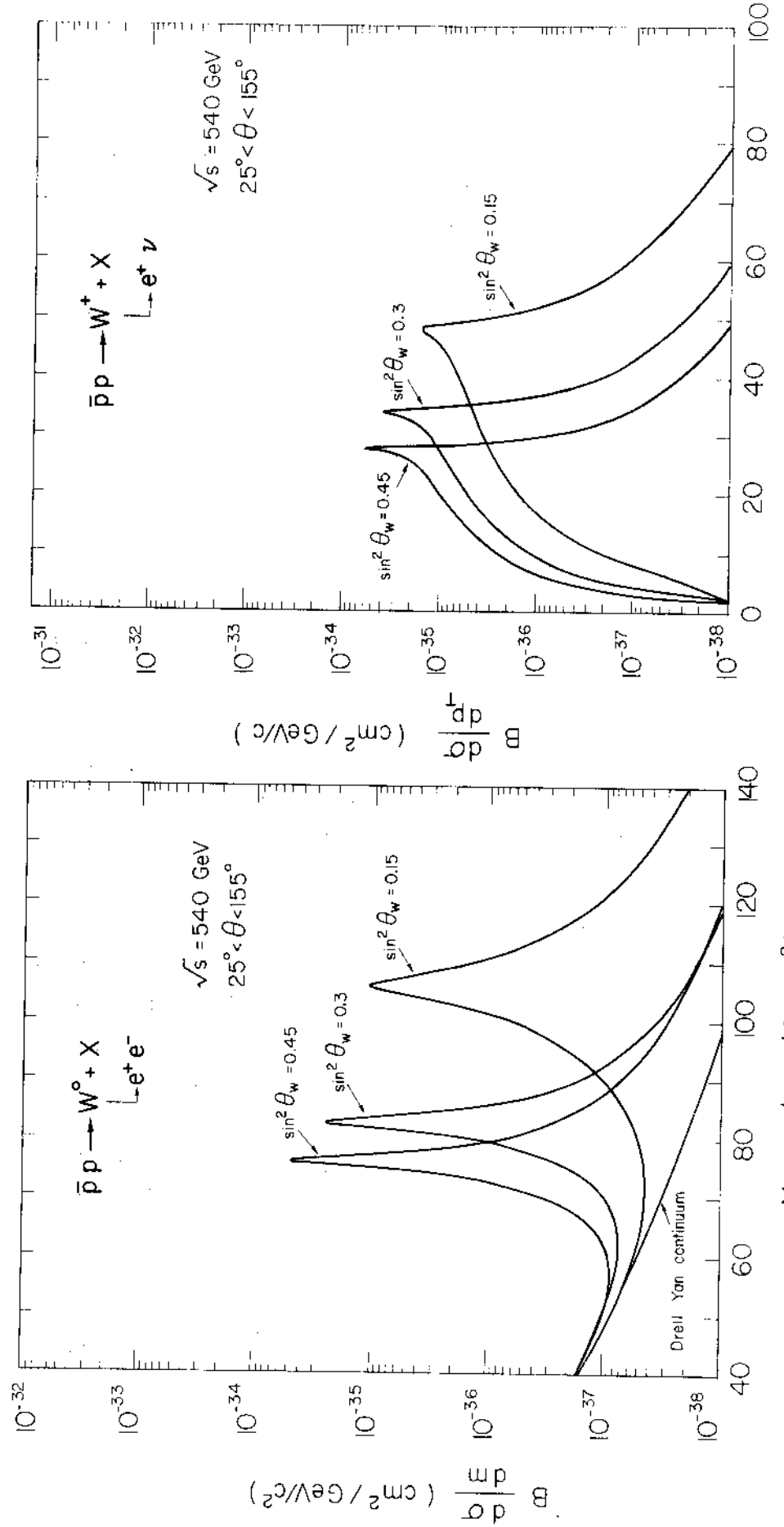

Figure 2.2. Dilepton invariant mass from $W^0 \rightarrow e^+e^-$ decay integrated over the angular acceptance $25° < \theta < 155°$ for $p\bar{p}$ collisions at $\sqrt{s}$ = 540 GeV and for different values of the Weinberg angle θ_W. Drell-Yan continuum is also shown for comparison.

Figure 2.3. Single charged lepton distribution integrated over the angular range $25° < \theta < 155°$ from $W^+ \rightarrow e^+ + \nu$ decay and $p\bar{p}$ collisions at $\sqrt{s}$ = 540 GeV according to the quark parton model for various values of the Weinberg angle θ_W.

The leptonic decay channels of both the neutral and charged bosons represent the most obvious way of detection. In the case of the W^o a pair of charged leptons are emitted. A narrow resonant peak (reminiscent of the ψ/J signature) is easy to detect (Fig. 2.2). In the case of the charged boson, a substantial fraction of the emitted leptons are confined close to the maximum of the transverse momentum (Fig. 2.3). Furthermore a large fraction of the transverse momentum will be missing because of the emitted neutrino. Our detector is capable of recording such a missing momentum.

Fig. 2.4 shows the calculated product[16] $\sigma.B$ for the process:

$$\bar{p} + p \rightarrow W^{\pm} + X$$
$$\qquad\qquad\quad \hookrightarrow e^{\pm} + \nu$$

as a function of the $W^{\pm}$ mass. The large C.M. energy available allows us to investigate the existence of such particles up to masses of about 200 GeV/c^2. The rapidity distribution of the emitted leptons[17] is shown in Fig. 2.5. We remark that only 50% of W^o emit both leptons in the angular range $30^o < \theta < 150^o$ ($|y| \leq 1.3$) and 96% of the leptons are contained in the angular acceptance of our apparatus, $5^o < \theta < 175^o$ ($|y| < 3$).

An important signature of the weak decay of the intermediate boson can be found in the lepton angular distribution. The lepton distributions from the charged W show a strong forward-backward asymmetry (fig. 2.6a). This asymmetry is specific to $\bar{p}p$ collisions. The asymmetry for the W^o is expected to be small (fig. 2.6 b). On the contrary, in pp collisions, the lepton distributions are symmetric in $\cos\theta$.

Recently hadronic jets have been observed in e^+e^- annihilation experiments. According to CVC the W should then also decay into two hadronic jets. Observing the transverse momentum of the jet is most likely not a sufficient criterion to separate out the W signal from the (probably) more abundant background of hadronic origin[18]. However if the mass of the W is determined by observing both jets, the situation is far more promising[19] and depending on the actual backgrounds and

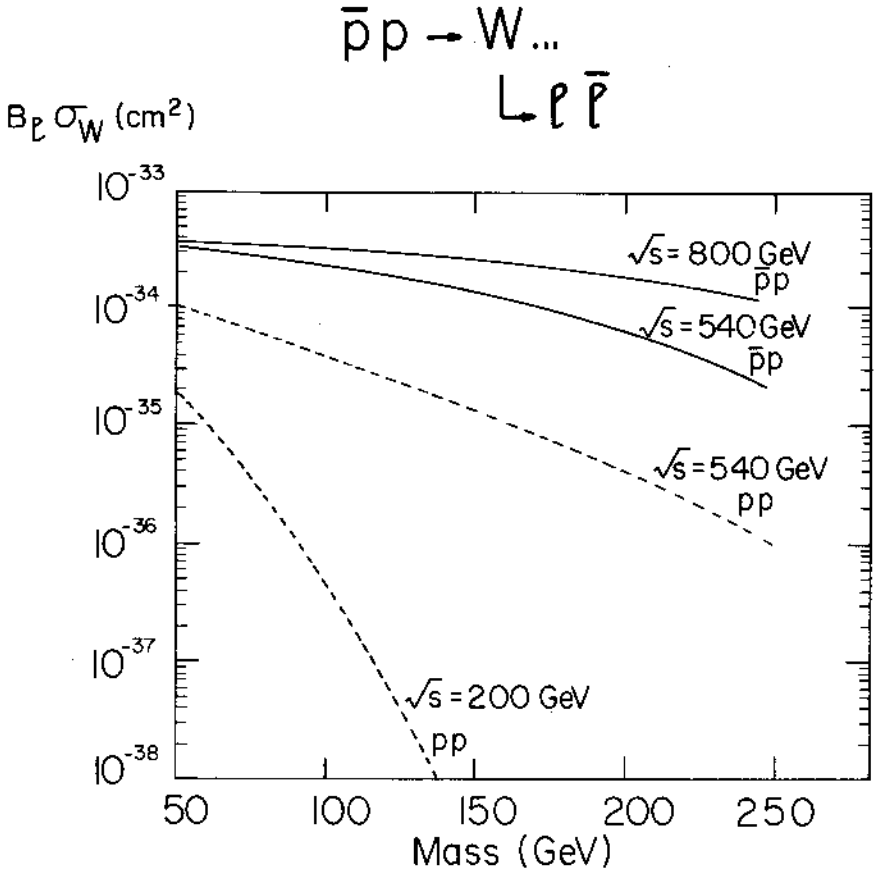

Figure 2.4. Total cross-section σ_W times leptonic branching ratio B_ℓ for the process of $W^\pm$ production by $p\bar{p}$ collisions and decay, given as a function of the mass and for different centre of mass energies. Proton-proton initiated curves are shown for comparison[16].

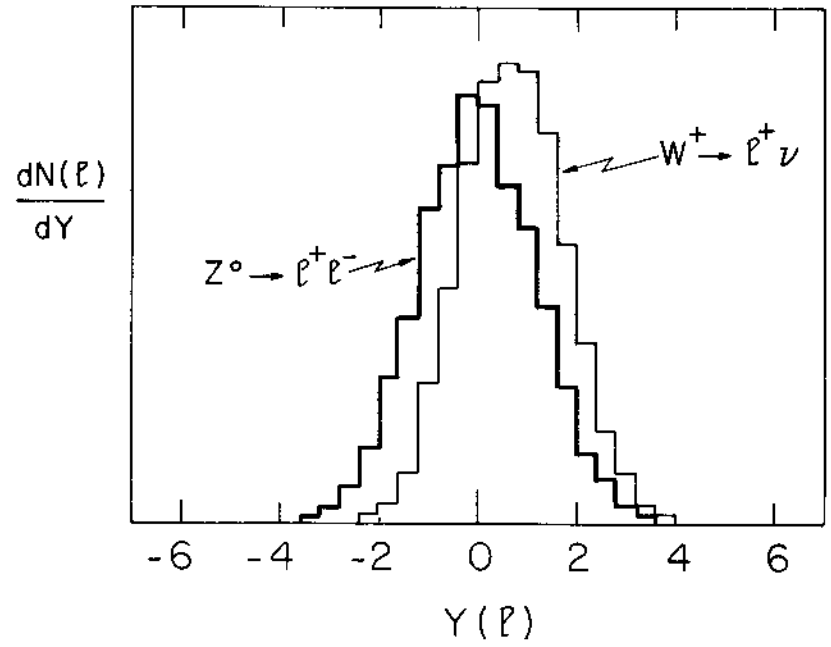

Figure 2.5. Rapidity distribution of the charged lepton emitted in $p\bar{p}$ collisions by the decays $W^o \to e^+e^-$ and $W^+ \to e^+\nu$

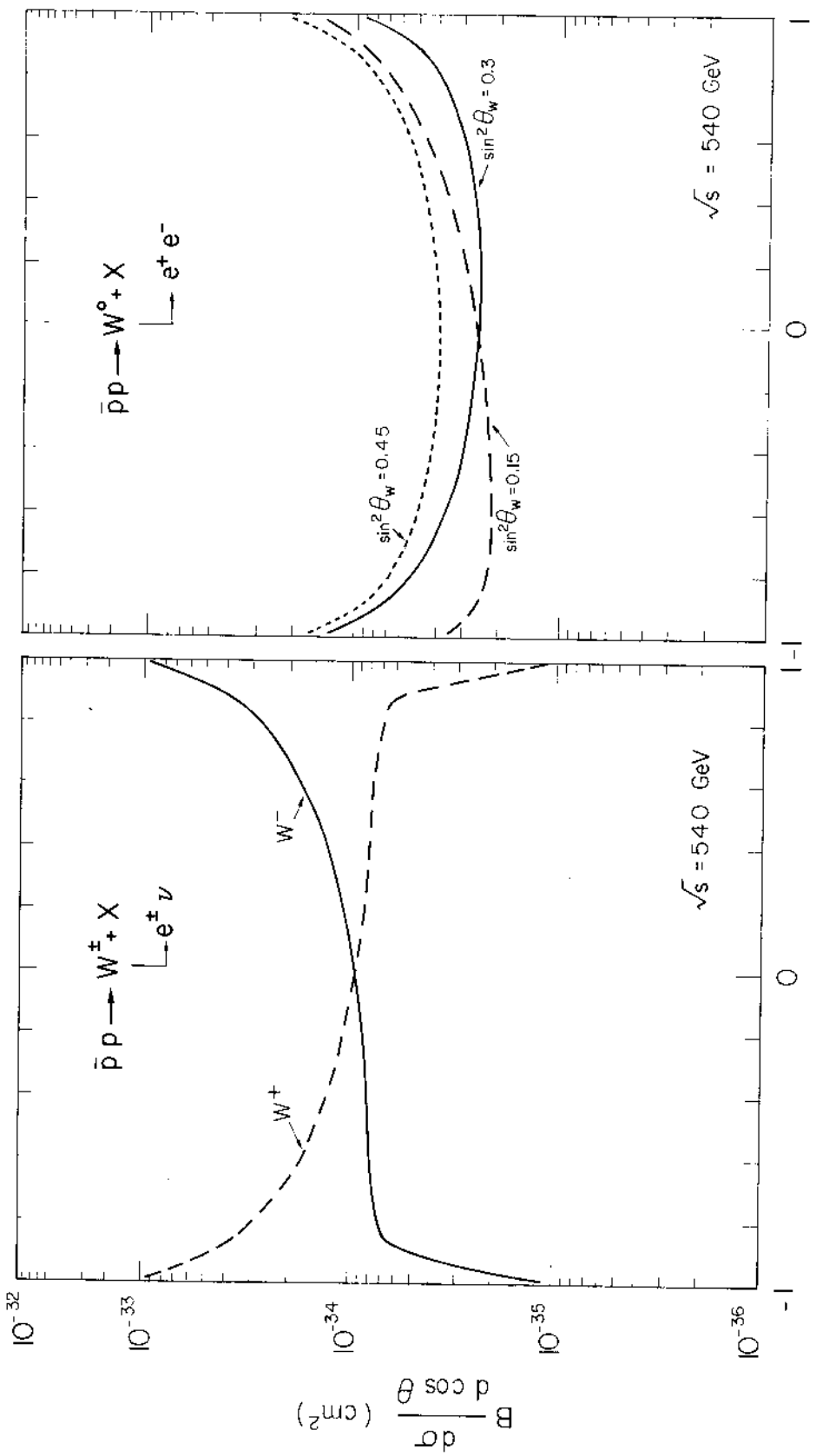

Figure 2.6a. Charge asymmetry for leptonic $W^{\pm}$ decays from $p\bar{p}$ collisions and $\sqrt{s} = 540$[16]).

Figure 2.6b. Charge asymmetry for $W^0 \rightarrow e^+e^-$ from $p\bar{p}$ and collisions various values of the Weinberg angle θ_W[16])

Note the rapidity variation of the distribution with $\sin^2\theta_W$.

mass resolution it might be possible to isolate the signal (Fig. 2.7). The interest in detecting the hadronic decays is motivated by the facts that:

(i) they constitute approximately 75% of the decays

(ii) they represent a direct way to measure the mass of the charged W's.

An additional criterion which can be used in order to separate jets from W decays from ordinary strong interactions is the presence of leptons or/and strange particles since 3/8 of the W decays are expected to be of the type $W^{\pm} \rightarrow (c\bar{s})$.

However our primary objective in the search for $W^{\pm}$ and W^{o} rests on leptonic decays. Background due to non resonant Drell-Yan and other sources will be discussed later in the proposal. For the moment we anticipate the conclusion that they appear negligible.

Number of events for an integrated luminosity of 10^{36} cm^{-2} are given in Table 2.1.

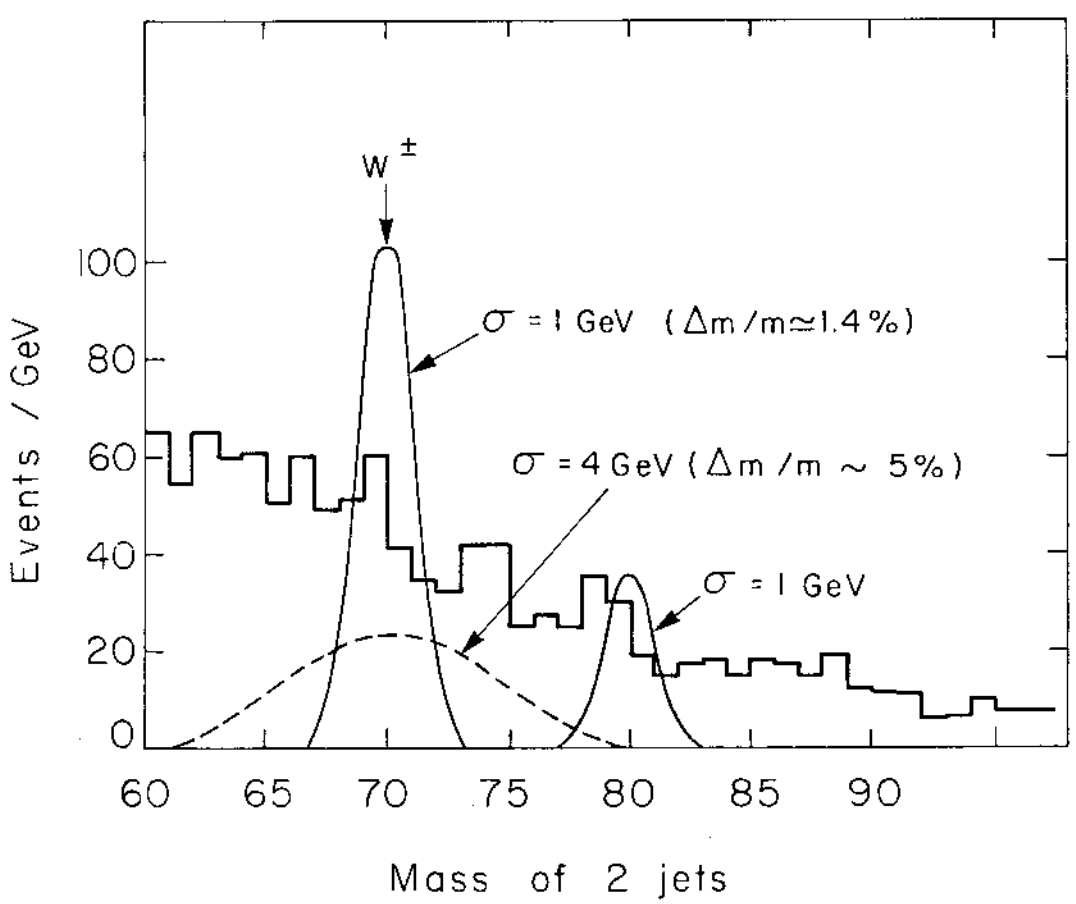

Figure 2.7. $W^{\pm} \rightarrow$ jets and $W^{o} \rightarrow$ jets signals and strong interaction background calculated in the vector gluon model[19]. Data are shown for an integrated luminosity of 10^{35} cm^{-2}.

TABLE 2.1. $W^{\pm}$ and W^{o} Decay Channels, partial cross sections and expected events for $\int Ldt = 10^{36}\ cm^{-2}$.

Channel	Branching ratio	Cross-section (cm^2)	Number of events for $\int Ldt=10^{36} cm^{-2}$
$W^+ \to \mu^+\nu_\mu$	1/8	$2.9\ 10^{-34}$	290
$W^+ \to e^+\nu_e$	1/8	$2.9\ 10^{-34}$	290
$W^+ \to u\bar{d}$	3/8	$8.7\ 10^{-34}$	870
$W^+ \to c\bar{s}$	3/8	$8.7\ 10^{-34}$	870
$W^- \to \mu^-\bar{\nu}_\mu$	1/8	$2.9\ 10^{-34}$	290
$W^- \to e^-\bar{\nu}_e$	1/8	$2.9\ 10^{-34}$	290
$W^- \to \bar{u}d$	3/8	$8.7\ 10^{-34}$	870
$W^- \to c\bar{s}$	3/8	$8.7\ 10^{-34}$	870
$W^o \to e^+e^-$	5%	$8.\ 10^{-35}$	80
$W^o \to \nu_e\nu_e$	5%	$8.\ 10^{-35}$	80
$W^o \to \mu^+\mu^-$	5%	$8.\ 10^{-35}$	80
$W^o \to \nu_\mu\bar{\nu}_\mu$	5%	$8.\ 10^{-35}$	80
$W^o \to q\bar{q}$	80%	$13\ 10^{-34}$	1300

2.3. HIGGS BOSON PRODUCTION. A crucial feature of gauge theories is that the masses of the gauge bosons and renormalizability are obtained using the Higgs mechanism. Every gauge theory has at least one physical neutral scalar Higgs boson. Therefore looking for such particles should be an integral part of any programme to study weak interactions at high energies. In the simplest W-S model there is only one of such neutral Higgs bosons, H. The Higgs boson could be less massive than the $W^{\pm}$ and W^{o}. Other possibilities exist for instance if Higgs particles are much heavier than the intermediate vector bosons. Their self interactions could be large and a whole new set of effects could emerge at centre of mass energies $\geq$ 200 - 300 GeV.

In the standard W-S model, a spin zero Higgs boson couples to other particles with strength proportional to their masses. As soon as one can produce truly heavy particles, either quarks or intermediate bosons, the process of production of a Higgs via bremsstrahlung becomes non negligible.

Assuming that there are no quarks as massive as W's,the H mass is required[20] to be less than about 7 GeV. The production cross-section for H production in p-p collisions has been recently calculated by Georgi, Glashow Machacek and Nanopoulos[21]. They have considered quark antiquark annihilation and gluon-gluon annihilation. The coupling between gluons and H is related to the total number of heavy quark flavours (even those so heavy that the corresponding new hadrons are inaccessible). In their numerical estimates (Figure 2.8) they have used only three flavours. The number of heavy quarks and therefore the H production could indeed be much larger.

Another process which is experimentally of interest in our case is the associated production of a $W^{\pm}$ or W^{o} and a H[22]. Since the W bosons have large masses, the cross-section for associated W, H production is appreciable. The advantage of this process is that the additional presence of the $W^{\pm}$ or W^{o} constituents a very important experimental signature.

The cross-section has been calculated[22] with standard antiparton-parton distribution functions and the cross-section for the elementary

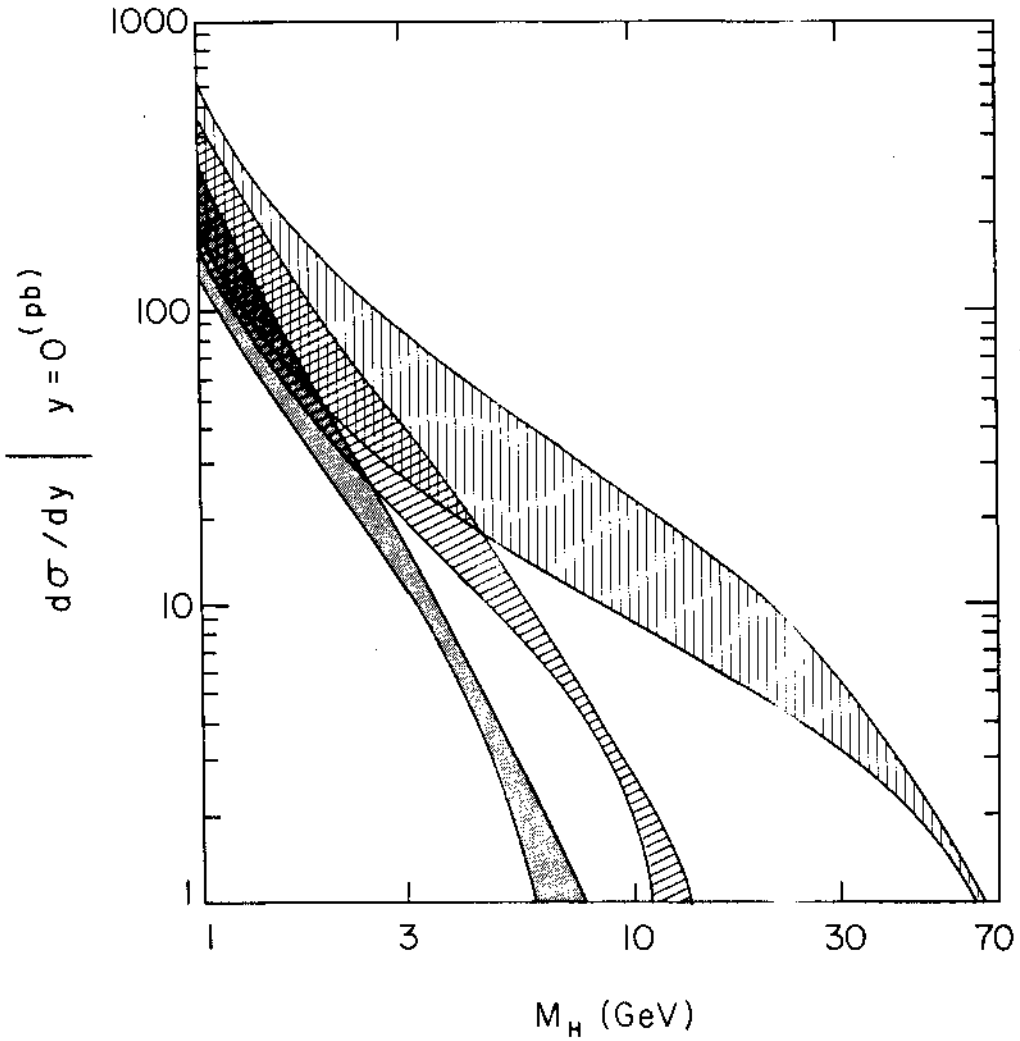

Figure 2.8. $d\sigma_H/dy|_{y=0}$ as a function of H mass. Each shaded band represents a different centre of mass energy ($\sqrt{s}$ = 27.4, 60, 400 GeV). From reference 21.

process $q + \bar{q} \rightarrow W + H$ given by M.K. Gaillard and J. Ellis[15].

Results are shown in Figure 2.9. It is evident that we can reach sensitivity to large masses (provided the $W^{\pm}$ mass is large).

The decay of the H boson depends critically on its mass. For masses between $\sim$ 4 GeV and 10 GeV, the $\tau\bar{\tau}$ and $\bar{c}c$ decay modes are accessible and dominant. The experimental signature is then the presence of at least one additional lepton in the debris of the W-producing event. If the mass is greater than $\sim$ 10 GeV, H decays mostly into hadrons containing the Υ constituents. Until the next hadronic or leptonic threshold is

encountered (corresponding to yet another flavour of lepton or quark), these decay modes will predominate. There may be the possibility that the new upsilon-related hadrons are stable. Another alternative is that the Υ belongs to yet another flavoured set of quarks which enjoys weak couplings to other flavours[21]. In this case the new hadrons will decay by weak cascades producing multi-leptons or multi-strange particle final state.

The effectiveness of the associated production method for observing the Higgs relies onto the fact that the H-$W^{\pm}$ cross-section may be as much as few percent of the ordinary $W^{\pm}$ production and therefore the additional leptonic signatures are highly significant.

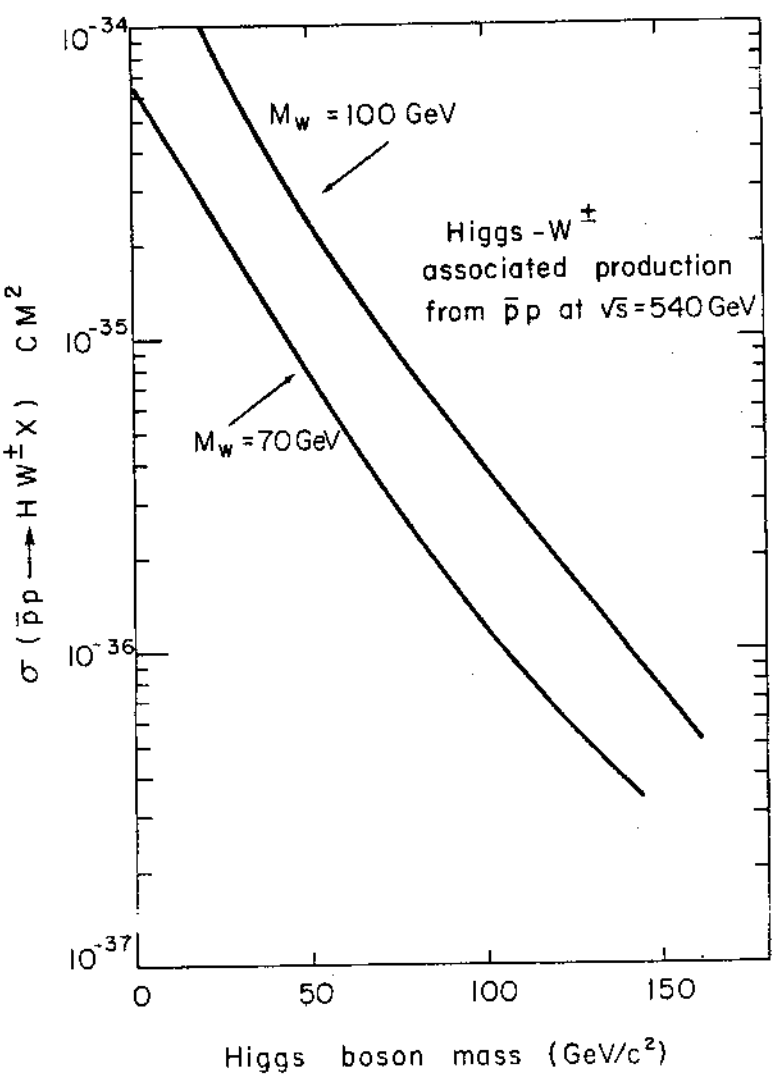

Figure 2.9. Associated Higgs-W production according to the quark-parton model and Weinberg Salam couplings[22].

2.4. DYNAMICS OF HADRON CONSTITUENTS

2.4.1. QUARK SCATTERING. The centre of mass energy of 540 GeV brings closer the regime of 'asymptotic freedom' for hadronic constituents (quarks). Already over the range $10 \lesssim \sqrt{s} \lesssim 60$ GeV there are strong indications for quasi-free behaviour of quarks. The general features of high p_T particle production in hadron-hadron collisions are consistent with a constituent interaction picture[23]. A growing body of evidence suggests that the basic mechanism for this process is a single large angle elastic scattering of quarks followed by quark fragmentation into a jet of hadrons[24]. If this viewpoint is correct the kinematics of jet production are directly related both to the elementary cross-section for quark-quark interactions and to the parent hadron structure functions.

In order to estimate the cross-section for jet production in pp and $p\bar{p}$ interactions for our energy range we have followed calculations of Peierls Trueman and Wang[25]. For elementary quark-quark scattering we consider two possibilities:

(i) coloured vector gluon exchange and (ii) the empirical Field-Feynman form $d\sigma/dt \sim 1/(-\hat{s}\,\hat{t}^3)$[26]. The latter form was chosen to fit the experimental invariant cross-section for single meson production at $2 < p_T < 8$ GeV/c:

$$E\,\frac{d\sigma}{dp^3} = \frac{1}{p_T^8}\,F(x_T, \theta_{CM}), \qquad x_T = 2p_T/\sqrt{s}$$

Additional assumptions used by Peierls et al. are (i) zero transverse momentum for the colliding quarks, (ii) PPT structure functions for the valence quarks[27] and (iii) $(1-x)^7/x$ dependence for sea quarks. Since field theoretical models based on vector gluon exchange predict a p_T^{-4} falloff it may be that the presently observed p_T^{-8} falloff will be replaced by a p_T^{-4} dependence at higher energies - hence both possibilities are considered by Peierls et al.[25].

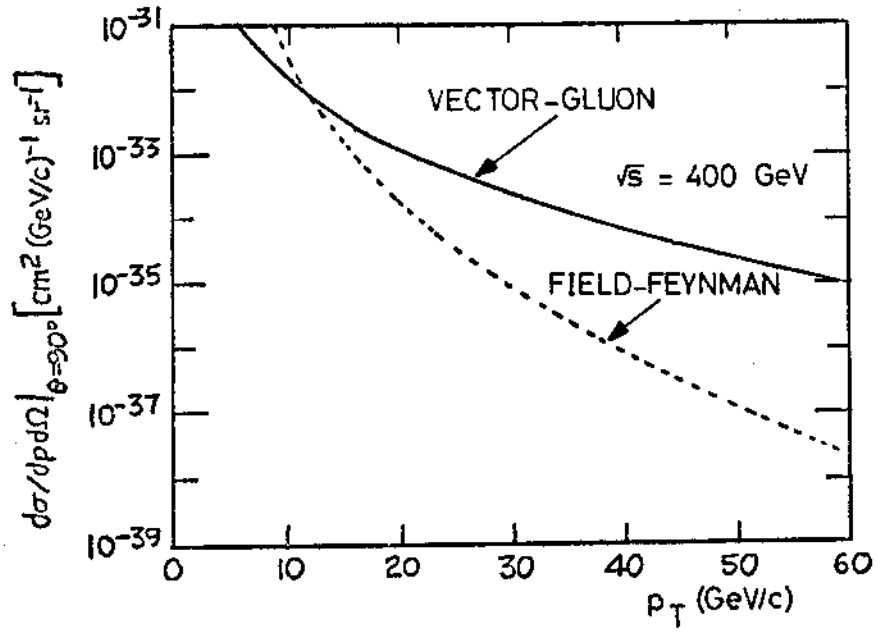

Figure 2.10. Cross-section $\frac{d\sigma}{dpd\Omega}$ for hadronic jets at 90° as a function of p_T for various models. Predictions are for pp interaction at $\sqrt{s}$ of 400 GeV[25].

Figure 2.10 shows the predicted cross-section $d\sigma/dpd\Omega$ versus p_T for jets produced at θ_{CM} of 90° in pp collisions at $\sqrt{s}$ of 400 GeV. Figure 2.11 shows the dependence of this cross-section on $\sqrt{s}$ in the vector gluon model. Figure 2.12 shows that pp and $p\bar{p}$ cross-sections are essentially the same for the p_T range accessible at the planned luminosity, ($L = 10^{30} cm^{-2} sec^{-1}$) in the vector gluon model[25]. The angular distribution of a jet recoiling against a 90° jet is shown in Figure 2.13 for pp interactions at $\sqrt{s}$ of 400 GeV.

Experimental studies of leptonic and hadronic processes have shown the following properties for the process q → hadronic jet:[28]

(1) Limited hadron transverse momentum, ∿ 300 MeV/c relative to the jet axis.

(2) Universal form - that is quarks appear to fragment in the same way

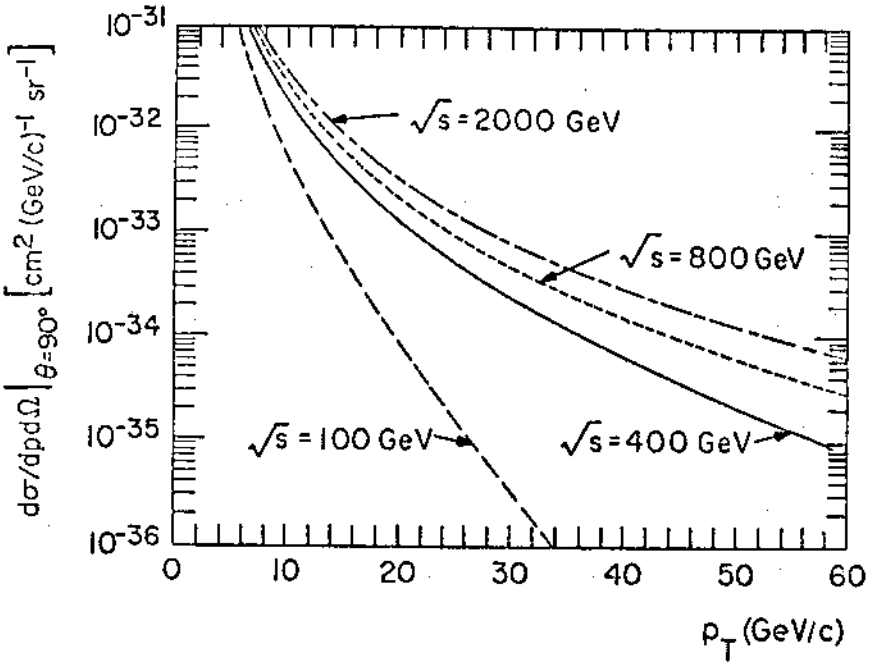

Figure 2.11. p_T dependence of $\frac{d\sigma}{dpd\Omega}$ for hadronic jets at 90^o in pp interactions at $100 < \sqrt{s} < 2000$ GeV in vector gluon model[25].

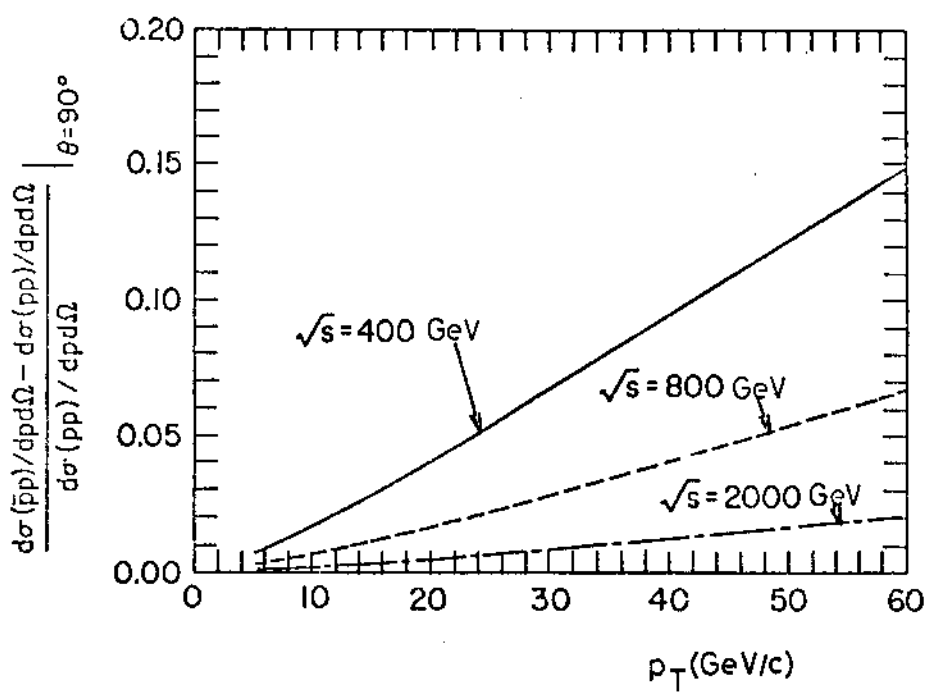

Figure 2.12. Comparison of pp and $p\bar{p}$ cross-sections for hadronic jets at 90^o in the vector gluon model[25].

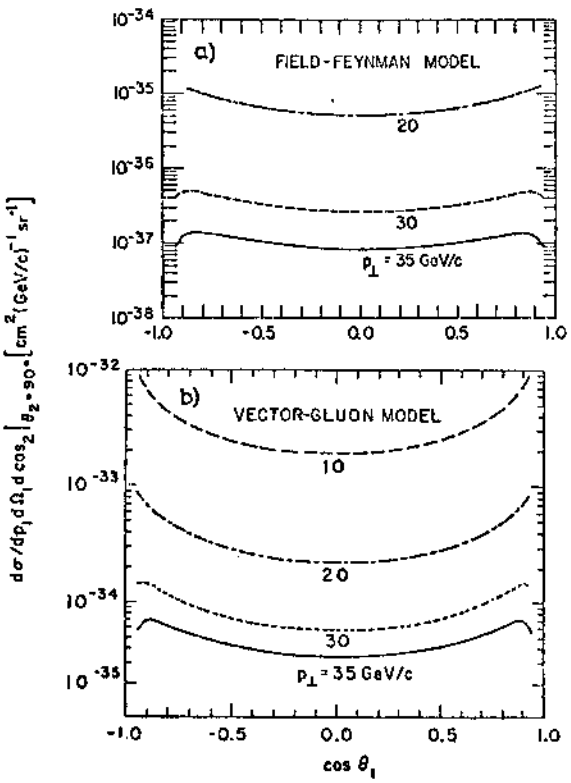

Figure 2.13. Double jet cross-section $d\sigma/dp_1 d\Omega_1 d\cos\theta_2|_{\theta_2=90^\circ}$ as a function of cos θ_1 the angle of the second jet for various values of p_T for (a) Field-Feynman model and (b) vector gluon model. $\sqrt{s}$ = 400 GeV

irrespective of whether they are produced in e^+e^-, νN, e^-N or NN collisions.

(3) The inclusive single hadron distribution within the jet scales.

The theoretical picture is the following: as the quark leaves the others the forces responsible for confinement build up an ever larger field[29]. The many quarks and antiquarks produced then gather into colour singlets $q\bar{q}$ and qqq.

Field and Feynman[30] have developed a specific model of quark decay which leads to direct experimental verifications. Detailed study of quark fragmentation is an important element in our physics programme.

Apart from the intrinsic interest of this process, its understanding is also important in relation to hadronic decays of W. Thus an effective signature for charmed or strange quarks would facilitate the study od $W \to c\bar{s}$. Brodsky has recently reviewed techniques for identifying the parent of a hadronic jet[31]. The retention of charge and other additive quantum numbers by the leading particle ($z \to 1$) in a jet decay may be useful as a jet discriminant.

Jacob and Landshoff have discussed the difficulty of experimentally defining a jet at ISR energies because of the large angular aperture, $\sim 40^{o}$ for a 5 GeV/c jet[32]. Since the angular aperture of a jet goes approximately as $\sin\theta_{CM}$ $\ln p_T/p_T$ the collimation will improve in the higher p_T range afforded by our experiment. Computer simulation of events has shown that at our energies jets should be clearly identifiable 'by the naked eye' (Figure 2.14). For a given p_T range, the increasing

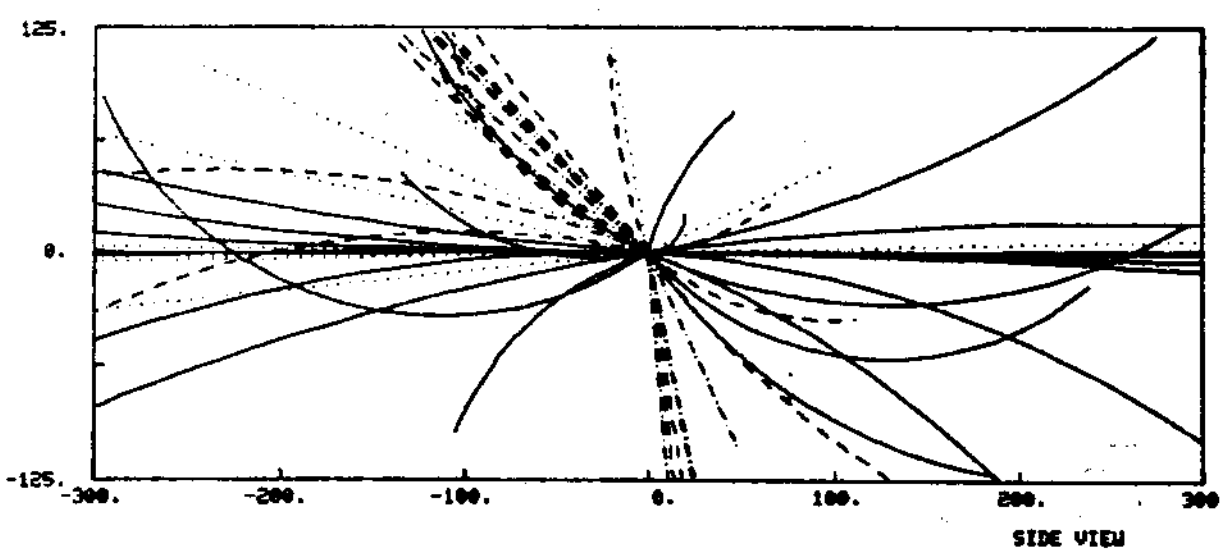

Figure 2.14. Computer simulated quark-quark scattering event. The transverse momentum is p_T = 20 GeV/c. Magnetic field and aspect ratios correspond to our actual set-up- The particles belonging to the jets are dot-dashed. Dotted lines are π^0's.

collimation of the jet away from $\theta_{CM} = 90^{o}$ also enhances jet recognition at the trigger level. Figure 2.15 shows the p_T dependence of jet production at $\theta_{CM} = 90^{o}$, 20^{o} and 6^{o} calculated by Peierls et al. for p_T^{-4} jet production[25]. The 20^{o} cross-section is of the same order of magnitude as the 90^{o} cross-section up to $p_T \sim 40$ GeV/c. Thus high p_T studies are desirable at moderate angles which also afford higher CM energies in the quark-quark CM frame.

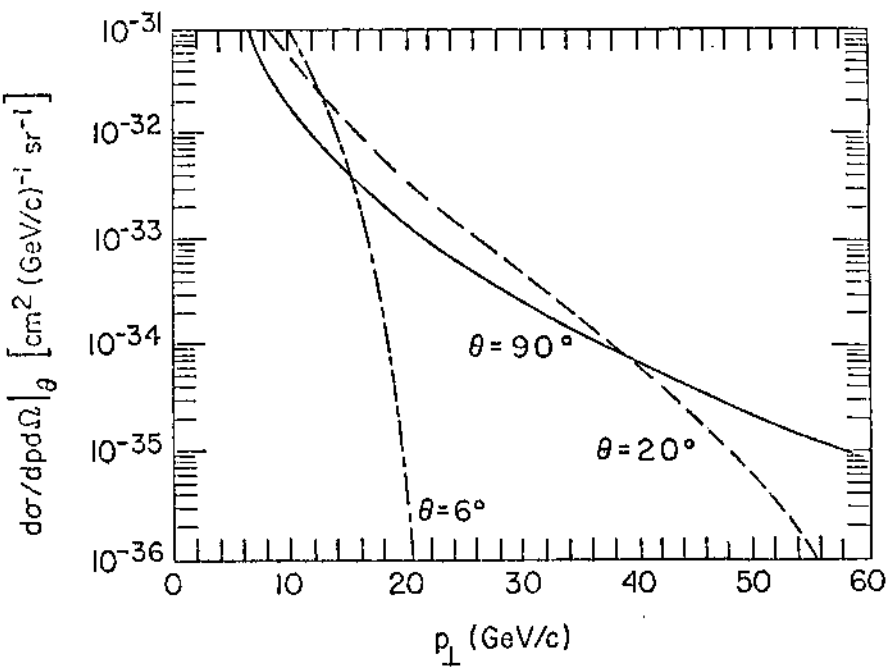

Figure 2.15. Predicted cross-section versus p_T for hadronic jets at various angles in pp collisions at $\sqrt{s}$ of 400 GeV from the vector gluon model[25].

Since the cross-section for large p_T jets is relatively small, a trigger selection is necessary. The best unbiased trigger is the requirement of a large transverse energy with full azimuthal

symmetry. With such a trigger, events with two or more jets can be detected without bias.

Most studies to date of high p_T phenomena have been made by triggering on a single high p_T particle. In the quark-quark scattering model the single high p_T particle comes from a quark carrying typically $\sim$ 15% more momentum than the single particle[26]. The ratio $\sigma(pp \to jet + X)/\sigma(pp \to \pi^0 + X)$ is shown in Figure 2.16 as a function of x_T for the vector gluon and Field-Feynman models; it depends only[25] on x_T and θ_{CM}. A recent Fermilab study at 200 GeV/c is in agreement with the Field-Feynman ratio for $3 < p_T < 5$ GeV/c [33].

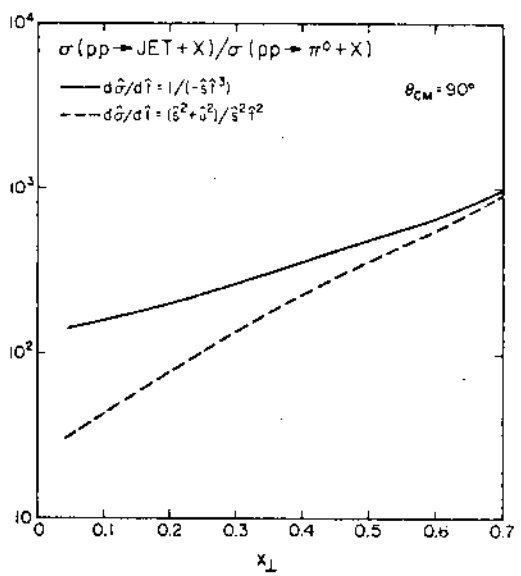

Figure 2.16. Predicted ratio $\sigma(pp \to jet + X)/\sigma(pp \to \pi^0+X)$ versus $x_T = 2p_T/\sqrt{s}$ with $\theta_{CM} = 90^\circ$ from the quark-quark scattering model of Field-Feynman (solid curve) and from a vector gluon exchange model (dashed curve).

In contrast it seems clear that high p_T studies at the $p\bar{p}$ collider should be strongly focussed on jet production for the following reasons:

(1) jet production kinematics are likely to be more directly related to the underlying quark dynamics than single particle production;

(2) the jet fragmentation mechanism also relates directly to quark dynamics;

(3) since the cross-section for jet production is much higher than for single particle production at the same p_T, jet triggers will permit studies out to larger p_T than will single particle triggers;

(4) hadronic decays of W will have to be jet studies.

Finally we would like to recall that cosmic ray experiments seem to indicate[7] that in the energy range of the present experiment large p_T events occur with probabilities which are much greater than those observed at ISR and FNAL.

2.4.2. GLUON INTERACTIONS. It is known from momentum sum rule that about one half of the momentum of the proton is carried by constituents which do not interact with lepton and photon probes. These are probably gluons which are expected to be totally neutral. The importance of gluons in hadron-hadron collisions has been pointed out by Van Hove and Pokorski[34]. They suggest that inelastic production in the central region is mainly due to gluon interactions. They review the evidence for clusters and show that data are consitent with production of neutral clusters emitted independently with flat rapidity distribution and small p_T. In general we can say that QCD implies existence of gluon jets at some level[31]. Any collision that produces direct (real or virtual) hard photons will also produce gluon jets. A gluon jet may be identified from its global neutral character, its quantum numbers and, relatively to quarks, the suppression of leading fragments[31].

Brodsky[31] has pointed out that the most important signature of a gluon jet may be its hadron density dn/dy in the central rapidity region.

Whether gluons jets exist or not, it is anticipated that gluons will become of considerable experimental significance in the energy range

of the proposed experiment[35].

2.4.3. QUARK-QUARK ANNIHILATION. The $q\bar{q}$ annihilation in the Drell-Yan process leads via a virtual photon to lepton pair production.

A recent high luminosity study of the reaction $p + N \rightarrow \mu^+ + \mu^- + X$ at FNAL shows that this process accounts for the production of the lepton pair continuum in the mass range $5 \leq M_{e^+e^-} \leq 10$ GeV/c^2.[36] The scaling behaviour of the Drell-Yan cross-section has the form:

$$d\sigma/dM\,dx = F(x, M^2/s)/M^3$$

As emphasized in reference 1 this scaling law precludes an extension of the $M_{e^+e^-}$ - mass range beyond 10 GeV/c for the present experiment. Nevertheless the study of the scaling properties of the Drell-Yan process as a function of s, p_T and x in the accessible mass range will be an important activity. Drell-Yan pairs with $x \gtrsim 0.1$ will be accompanied by a forward diquark system in the same hemisphere[2]; diquark studies will require specialised forward detectors. Another application of $p\bar{p}$ collisions for Drell-Yan studies may be at the ISR where a comparison of lepton pair production in pp and $p\bar{p}$ interactions could provide a sensitive test of the quark model. Figure 2.17 for example shows the Drell-Yan scaling function $M^4 d\sigma/dM^2$ predicted by C. Quigg for two different forms of the nucleon structure functions in $p\bar{p}$ collisions[37].

The background from Drell-Yan leptons in W-boson searches is expected to be negligible[22].

At high energies we can expect contributions from gluon exchange[38]. This last process is expected to have a significantly larger hadron multiplicity than that associated with Drell-Yan events and unlike the Drell-Yan mechanism, will have the same production cross-section for pp and $p\bar{p}$ reactions.

It seems likely that heavy vector mesons such as J/ψ or Υ are produced by the strong fusion of a quark-antiquark pair.

A variety of models have been proposed for production of J/ψ in hadron-hadron interactions. Most of these involve a generalised Drell-

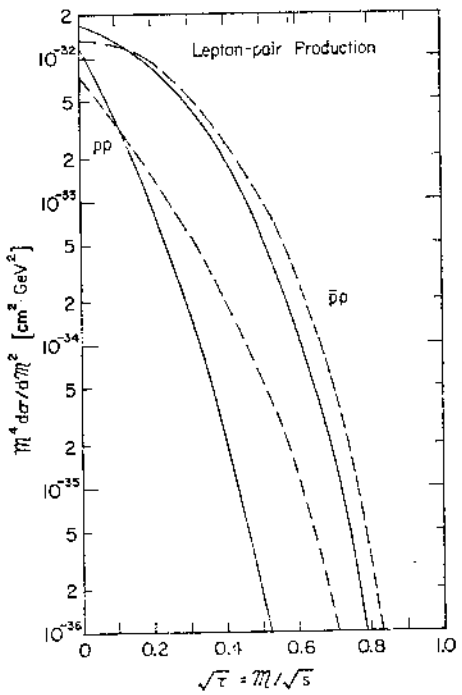

Figure 2.17. Scaling function $M^4\ d\sigma/dM^2$ for Drell-Yan pairs expected for Field-Feynman (solid line) and PPT (broken line) nucleon structure functions.

Yan mechanism in which hadron constituents (quarks, gluons or other) amalgamate to produce J/ψ. In the model of Halzen and Matsuda for example the constituents are light quarks (u, d) and antiquarks which form J/ψ via a single gluon intermediate state[39]. Donnachie and Landshoff on the other hand assume that the predominant mechanism is fusion of charmed quarks from the sea[40]. In their model fusion involving u, d quarks is suppressed due to its 'Zweig-violating' character, except close to production threshold where the higher momentum valence quarks take over, ($M_V^2 = x_1 x_2 s$ where x is the momentum fraction carried by the colliding quarks). The recent observation of $\sigma(p)/\sigma(\bar{p}) = 0.15 \pm 0.08$ for J/ψ production at 39.5 GeV/c ($M_V^2/s = 0.12$) supports the Donnachie and Landshoff model[41].

It is obvious that production of J/ψ and ϒ in $p\bar{p}$ collisions are of considerable significance in the understanding of these mechanisms.

2.5. PRODUCTION OF MASSIVE AND NARROW VECTOR MESONS- If massive new quarks exist there should also be narrow vector mesons analogous to the J/ψ and Υ. A question of primary interest is the production of heavy vector mesons with hidden quantum numbers beyond charm. We can attempt to infer the production cross-sections for such states from the measured cross-sections for J/ψ prduction[42]. Gaisser, Halzen and Paschos[43] have proposed the scaling rule for the production of such a meson of mass M:

$$\sigma = \frac{\Gamma}{M^3} F(s/M^2)$$

where Γ is the total width into hadrons and $F(s/M^2)$ is a universal dimensionless function.

The meson should decay into lepton pairs e^+e^- with a branching ratio $B_{e^+e^-}$. Thus it could be observed as a narrow peak in the lepton pair invariant mass with a cross-section:

$$B_{e^+e^-}\ \sigma = \frac{\Gamma_{e^+e^-}}{M^3} F(s/M^2)$$

which is independent of Γ. Assuming that $\Gamma_{e^+e^-} \simeq \Gamma_{e^+e^-}(J/\psi)$, we can estimate production from J/ψ data. It is interesting to remark that this procedure gives approximately the cross-section for $\Upsilon \to e^+e^-$ observed at the ISR[44].

Scaling according to M^2 rather than M^3 is also conceivable[45] and it is not ruled out by the experimental data. Figure 2.18 shows the resulting $\bar{p}$ excitation curves for the masses $9.5 < M < 100$ GeV/c^2.

Although these cross-sections appear substantially smaller than the expectations for $W^o \to e^+e^-$, the uncertainties on scaling and widths are amply sufficient to justify the following question: suppose one finds a narrow peak in e^+e^- say at 60 GeV/c^2. How do we know that we have found the W^o, rather than a bound $q\bar{q}$ state? The answer evidently rests on the observation of the asymmetry in the leptonic charge, which as

already pointed out is a specific feature of $p\bar{p}$ collisions.

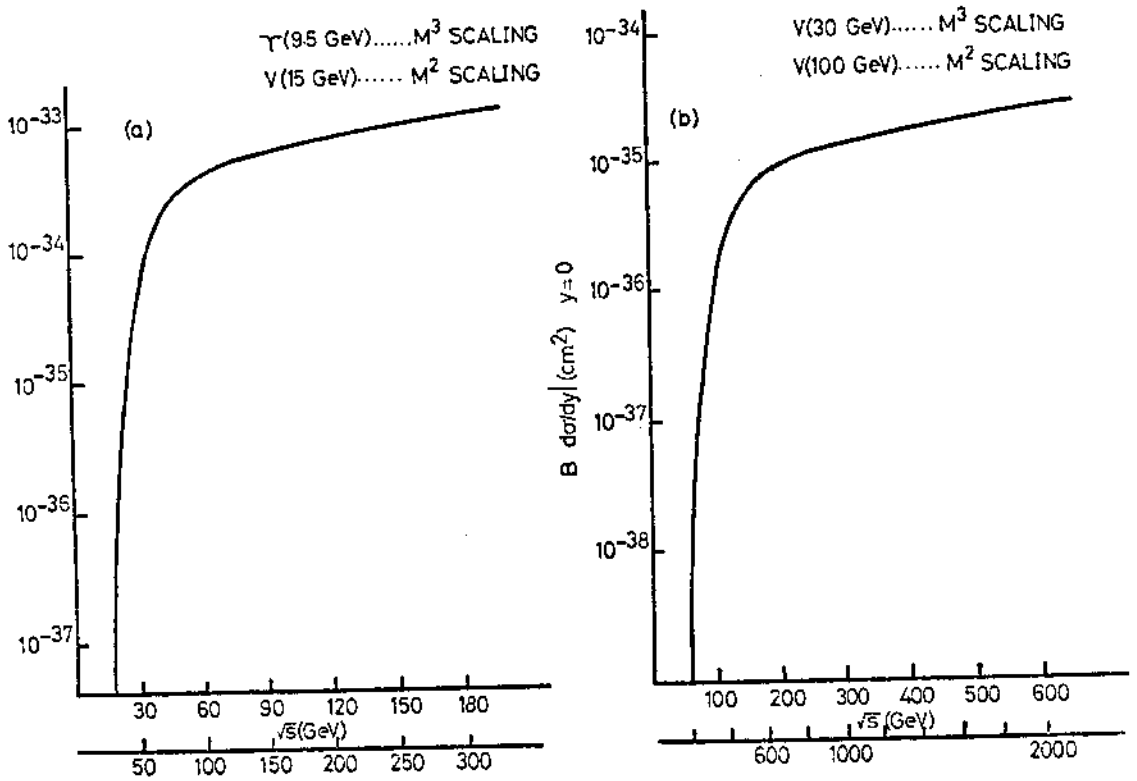

Figure 2.18. $B(V \to \mu^+\mu^-) \times d\sigma/dy|_{y=0}$ for vector meson production. The upper (lower) scale in s corresponds to $M^3(M^2)$ scaling.
a) Excitation curve for Υ(9.5 GeV) and V(15 GeV), and
b) Excitation curve for V(30 GeV) and V(100 GeV).

2.6. CONVENTIONAL HADRONIC PHYSICS

The general feature of ISR results on large cross-section phenomena can be globally referred to as 'log s physics'. We expect to find very significant changes between the ISR ($\sqrt{s}$ = 56 GeV) and the present experiment ($\sqrt{s}$ = 540 GeV), even for phenomena which have a scale for changes set by log s or the available rapidity range ΔY.

The extrapolation procedure is not entirely obvious and larger differences are expected for instance if $(\log s)^2$ terms need to be present, as suggested for instance by the most recent ISR measurements

on particle multiplicities[46].

Total cross-sections (Figure 2.19) could increase significantly from ISR energies, as inferred from a dispersion relation analysis of the ratio of the real to imaginary part of the forward amplitude at the ISR[47].

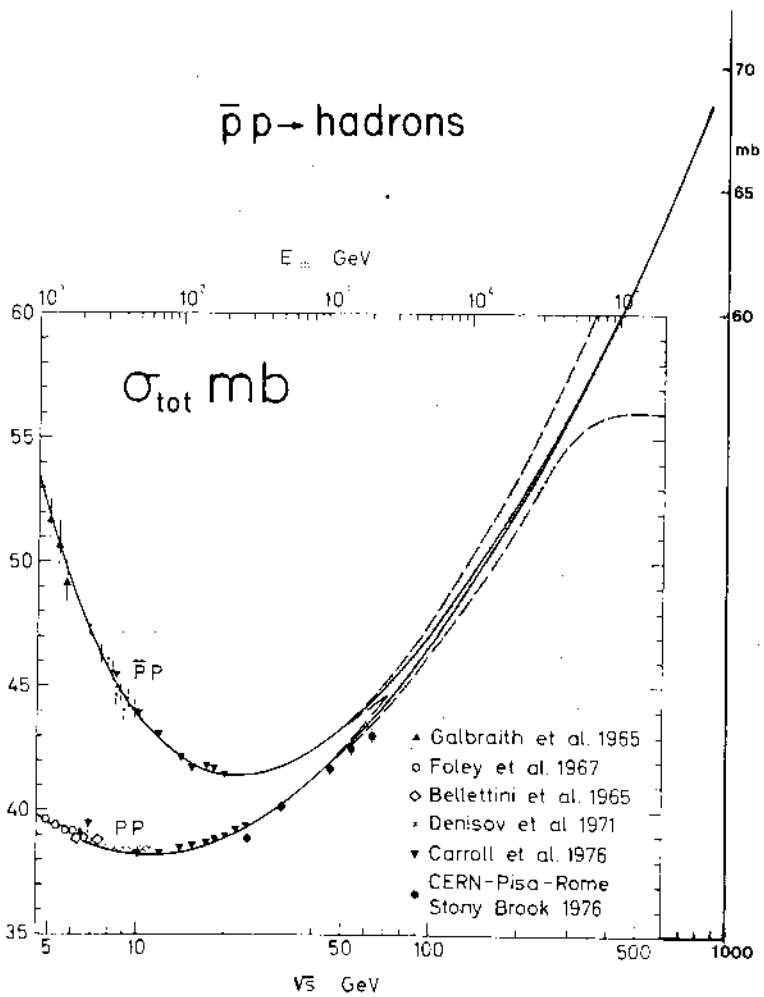

Figure 2.19. Measurements of total proton-proton and proton-antiproton cross-sections as a function of the centre of mass energy. The dashed area is the prediction of dispersion relations and of measurements of the real part of scattering amplitude[47].

The single particle inclusive reactions are expected to exhibit important changes from ISR to the proposed energies. Firstly, if two units of rapidity are obtained from each of the fragmentation regions,

the length of the central region is increased from $\Delta y = 4$ at ISR to $\Delta y = 9$. This expansion is of substantial benefit. Furthermore recent results indicate a slow but significant rise in the inclusive invariant cross-section around 90^{o} [46,48] (Figure 2.20).

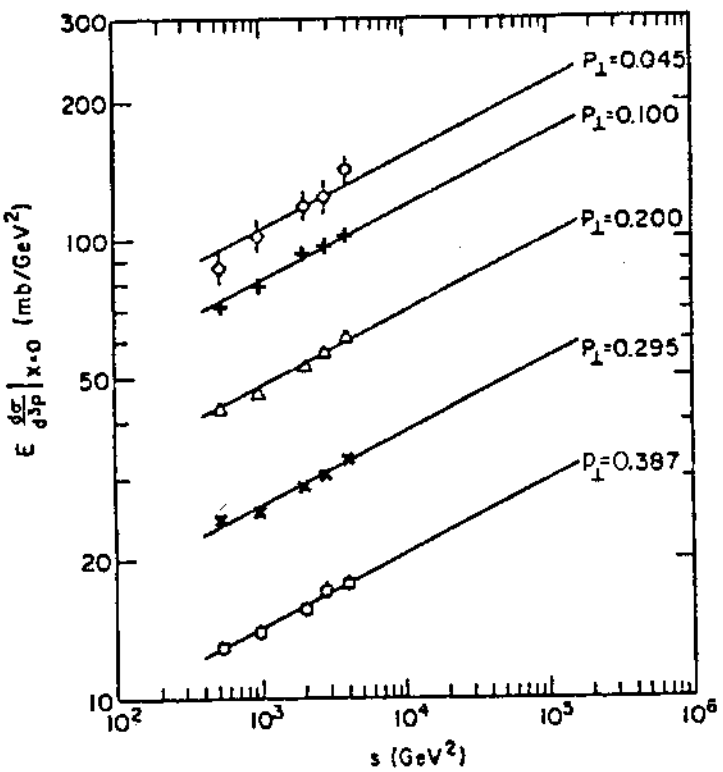

Figure 2.20. Energy dependence of $pp \rightarrow \pi^- X$ cross-section at x=0. The naive Pomeron Model predicts that this cross-section should remain independent of energy.

Extrapolations to $p\bar{p}$ collider energies would indicate a rise of the rapidity plateau by almost a factor two from ISR.

The higher energy would also facilitate the study of particle correlations, since the size of the central region is now about twice that at the ISR. Particles can be separated by more than one correlation length (2 units of rapidity) while remaining in the central region. This should allow separation between dynamical long range correlations, short range correlations and momentum-energy conservation effects.

The smooth changes expected if confirmed would be an important success of our present ideas about strong interactions. However there is evidence from cosmic rays that more important changes may manifest themselves. Figure 2.21 shows measurements of the mean charged multiplicity <N> as a function of energy, including the last ISR results[46]. The best fit, demands a $(\ln s)^2$ term, a consequence of the logarithmic rise of the plateau. The striking point of this figure is that, the extrapolated multiplicity for $p_{LAB} > 10^5$ GeV is well below, the indication of <N> deduced from cosmic ray experiments[49].

Finally we mention briefly the double-Pomeron exchange. By definition the double-Pomeron process A + B → A + X + B is characterized by i) quasi-elastic scattering of the incident particles A, B and ii) large rapidity gaps ($\Delta_{1,2} \geq 2$ units) between the central cluster x and the outgoing particles A, B. A first search for this process at the ISR gave a cross-section ∿ 10 - 20 μb for $30 < \sqrt{s} < 62$ GeV[50], consistent with theoretical expectations[51]. Subsequent studies by the CCHK[52] and CHOV[53] collaborations have confirmed this result[54]. The cross-section is expected to grow as ℓns and 30 μb at collider energies is a reasonable expectation[35]. Interest in this process is twofold:

i) to elucidate the nature of the Pomeron, i.e. to understand the dynamics of elastic and quasi-elastic processes, and

ii) to use this process to provide a Pomeron-Pomeron 'facility' for the study of I=0, C= G=+1 bosons in the J^{PC} series 0^{++}, 2^{++} and so on (quantum numbers of the cluster X). At the collider, ($2y_M$ = 13 units), rapidity gaps as large as $\Delta_{1,2}$ = 3 units would be compatible with masses M_X up to 20 GeV/c^2, ($M_X^2 \sim \mu_\pi^2 \exp(\Delta_X)$ where μ_π is the pion transverse mass). For masses $M_X \geq 3$ GeV/c^2 one expects $d\sigma/dM_X^2 \sim 1/M_X^2$.

The Pomeron may be no more than a phenomenological artifact. At the more fundamental level of QCD it seems increasingly plausible that the bosonic cluster x is the colourless product of a gluon-gluon interaction[35,55,56]. The question of how colour neutrality of the colour octets at the upper and low vertices is achieved in this reaction is moot. Whatever the final state interaction it is thought

that the fundamental production process for a bosonic cluster well separated in rapidity from other particles is a hard gluon-gluon collision. The close analogy with $\gamma\gamma$ scattering in e^+e^- collisions has been remarked on [35,56], and has been used to estimate a cross-section of $\simeq$ 15 μb for this process[35].

So we have the exciting prospect of a colliding gluon-gluon 'facility' at the $p\bar{p}$ collider. In this case many interesting and important possibilities are opened both for testing QCD and for boson physics. Since gluons unlike the Pomeron are flavour neutral the final states X should couple with equal strength to pions, kaons, charmed particle pairs etc.

2.7. NEW HADRONIC PHENOMENA. Cosmic ray experiments at energies exceeding the reach of our present accelerators have provided hints of some surprising new phenomena which should affect a major part of the total cross-section of the presently proposed colliding beams. The information is, of course, very scarce owing to the extremely fast fall of the primary flux (see Table 2.2), and it is based either on isolated events or on extensive air showers.

This trend is confirmed by the observation of isolated events above 100 TeV: Centauro events[57], T-star (500 charged secondaries)[58], and Andromeda[59]. The first observed Centauro event is a 230 TeV interaction 50 m above the emulsion chambers which produces 90 charged

TABLE 2.2. Primary cosmic ray flux at the top of atmosphere

Primary energy E	Flux N (> E)
1 GeV = 10^9 eV	40,000 $(m^2\ sec)^{-1}$
1 TeV = 10^3 GeV	1 $(m^2\ sec)^{-1}$
10^3 TeV = 10^6 GeV	1 $(m^2\ day)^{-1}$
10^5 TeV = 10^8 GeV	1 $(m^2\ year)^{-1}$

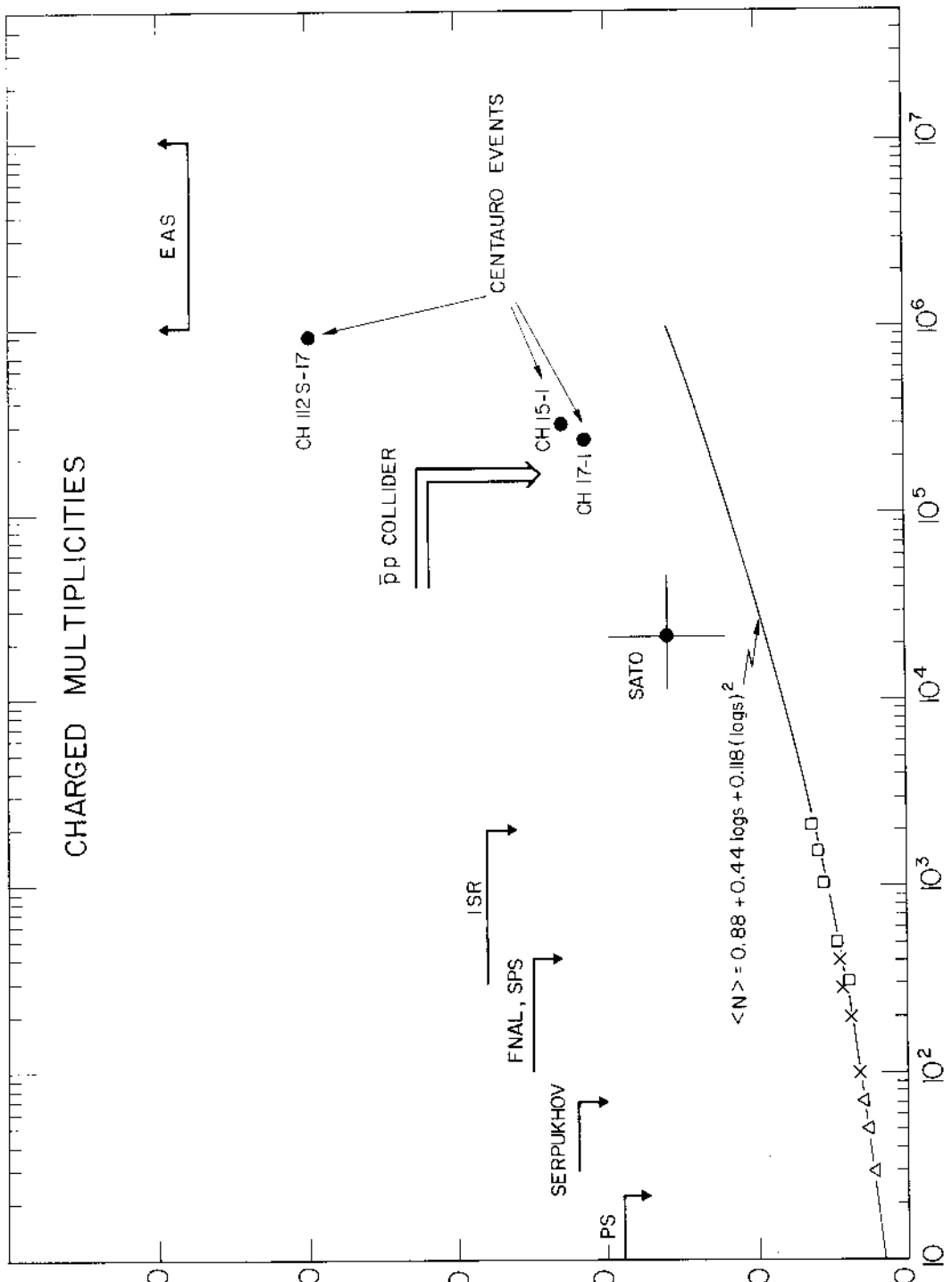

Figure 2.21. Charged multiplicities from accelerators, ISR and cosmic ray experiments. The line is the fit up to $(\log s)^2$ terms of the accelerator and ISR data. Note that cosmic ray results (mostly single events) indicate that there are about twice as many particles than what expected by this extrapolation.

particles with an invariant mass of 210 GeV and an average transverse momentum of 1.7 GeV with respect to the core axis. No neutral π's are observed! The apparent absence of π^0's at production sets the probability that this event is a fluctuation of a regular nuclear interaction at 10^{-6}. The high average transverse momentum rules out the possibility of a break up of a nucleus.

Besides these unusual events, observations indicate anomalies of the development of air showers above the same energy and suggest that 100 TeV is some kind of a threshold in hadronic interactions[7]. This threshold might have been directly observed in the Tien-Shan experiment[60]. A calorimeter measures the absorption length of hadrons or air shower cores in lead as a function of their energy. The result is shown in Figure 2.22. The penetration of cascades increases dramatically between 50 and 100 TeV, indicating the onset of new phenomena in hadron interactions.

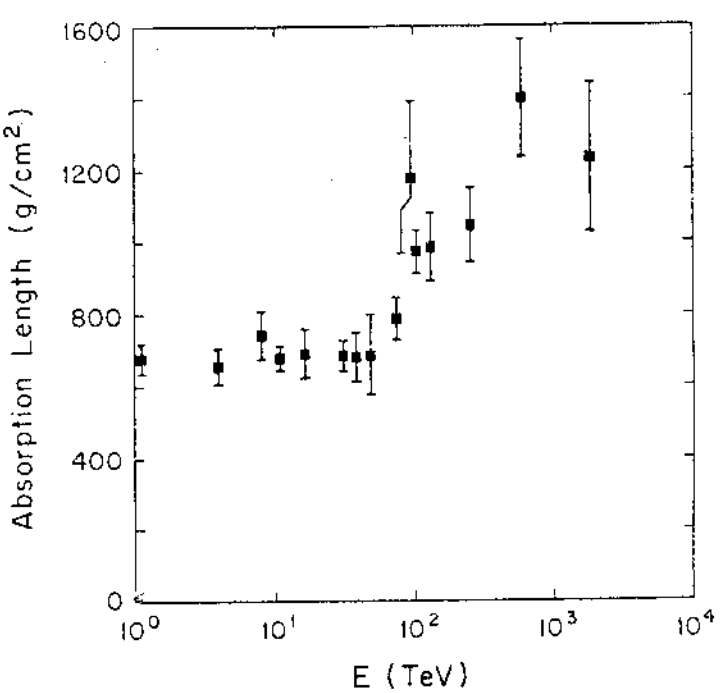

Figure 2.22 The Tien Shan anomaly in the penetration of cosmic ray showers as a function of the total energy measured in a calorimeter[60].

3. GENERAL DESCRIPTION OF THE SET-UP

3.1. GUIDELINES. The physics motivations of the preceeding chapters and the exploratory nature of the experimental programme have provided general guidelines for a more detailed design of the detector:

(i) In order to collect the largest amount of unbiased information at each event the detector must cover the largest possible fraction of the solid angle. In practice we have succeeded to insure detection of particles down to about one degree from the beam axis.

(ii) The simultaneous detection of large transverse momentum electrons, muons and neutrinos, the last ones by missing energy, is of importance when searching for a broad class of new physical phenomena.

(iii) We need energy measurements both by magnetic curvature and calorimetry. A global energy flow measurement remains of significance even for configurations where the local particle density is too large for the visual detectors to give meaningful curvature measurements. Likewise an electromagnetic shower detector complements the energy resolution of magnetic analysis for high energy electrons, like for instance from decays of the type $W^o \to e^+e^-$. It is also less sensitive to internal radiative corrections[61] and to bremsstrahlung in the vacuum chamber walls.

(iv) The detector must operate with minimum disruption of the SPS programme and in an environment which is relatively hostile because of high radiation levels, backgrounds and so on. Only unsophisticated and reliable equipment must be chosen. The problem of debugging and maintaining efficiently a complex equipment in the SPS tunnel should not be underestimated.

(v) The nature of our proposal is basically evolutionary and several separate elements (building blocks) are designed in such a way as to be operated almost independently and may eventually be installed in successive phases matched to the available luminosity and to the advances of civil engineering.

(vi) Data acquisition and trigger should be arranged in order to collect the maximum of information at each event and per unit of time.

Although the inner core of our detector could be installed in the SPS tunnel without major modifications for a first exploratory experiment, we have reached the conclusion that the minimum overall disruption to SPS programme is achieved by breaking-in of the new area before the beginning of the experimental activity. Furthermore a series of successive installation phases will inevitably delay some of the most challenging explorations to the advantage of ISABELLE which is expected to operate few years after the present proposal. However our design is sufficiently flexible as to permit substantial modifications in case a different strategy should be chosen.

3.2. INITIAL CHOICES. Before describing in detail the proposed set-up we discuss briefly the main underlying reasons for these choices. We start with the choice of the magnetic field. Schemes involving more than one field configuration have been discarded since they necessarily give bad fields over rather extensive transition regions.

The orientation of the field is not entirely trivial. Three major orientations have been considered:

i) A toroidal field ,always normal to the direction of emission and proportional to 1/r. The main advantage of this configuration is that the field has the maximum effect, and that the bending power is concentrated at small angles where the particle rigidity is maximal. We have discarded this scheme, since it has not been possible to arrive at a realistic design with more than about 60% transparency outside the coils. Also the general problem of the forces acting on the coils is quite serious.

ii) A solenoidal field[62]. This is the universally preferred solution of e^+e^- detectors. The bending power ($B.\ell$) is angle-independent as long as the solenoid is made long enough. A very long solenoid is required if one wants to measure particles emitted over several units of rapidity. The weak point of this arrangement is that after few units of rapidity the momentum resolution for charged particles becomes less accurate. Moreover the magnetic field does not extract from the beam pipe forward particles which carry a substantial fraction of the energy. Note that this problem does not exist in e^+e^- processes which are mediated by one-photon exchange

iii) A transversal field (dipole)[63]. The bending power increases rapidly at smaller angles of emission at least as long as the pole pieces are rectangular and sufficiently long. The main drawback of the system is a dead cone around 90°, where particles travel parallel to the field. In terms of solid angle, this does not represent a large fraction, and it occurs where the particle density is generally lowest. Compensating magnets help to increase the analysing power for small-angle particles.

The choice between (ii) and (iii) is very delicate and a conclusion has been reached on the basis of considerations most of which are not entirely fundamental. We prefer the dipole solution since the losses around the beam pipe appear more serious than the dead cone around 90°, where chambers can still detect tracks and calorimeters can give approximate energy determination. Other arguments in favour of the dipole is that it offers a good accessibility of the chambers and that there is no coil in front of the electromagnetic detector and dE/dx scintillation counters. Finally a solenoid would almost inevitably be a superconducting coil, whilst the dipole can be realised with a thin aluminium coil at room temperature.

The extreme complexity of some of the cosmic-ray events in this energy domain demonstrates the need for highly redundant, 'visual' multidimensional chambers. The relative high magnetic rigidity of charged tracks places strict requirements on the spatial accuracy. Finally, the remote possibility that free quarks may be produced within jets, and more ambitious particle separations by relativistic increase of dE/dx, are strong recommendations to retain the energy loss information for individual tracks. For these reasons we have developed and extensively tested[64] what we like to call an 'image chamber'. Rather than an entirely new device, an image chamber is a different, more complete way of extracting the information potentially present in a drift chamber. From the electronic point of view, the device is essentially a drift chamber with a large number of collecting wires. However the complete and (presumably) undistorted image of the ionisation electrons produced in the gas is now scanned and recorded.

Each of the chamber wires represents a 'scan line' of the image. Signals are stored like a 'video signal', that is the complete time dependence of the signal is retained, rather than just the timing of the centroid or the leading edge as customary for a Charpak-type drift chamber. In a few words, the principle of operation is clearly inspired by the television camera. Like in a television, 'scan lines' are stored either as charge in an analog shift-register or converted digitally and accumulated in a multi-bit shift-register. After parallel storage, scan lines could be read out sequentially. In principle, the resultant 'video signal' could be used to modulate directly the intensity of a CRT display which gives the image of the event which occurred in the chamber volume. The topology of the image is precisely the one seen by an idealized camera located at infinity and with its optical axis parallel to the recording wires. The critical track configuration is the one in which a multiplying wire is subject for extended periods of time (several microseconds) to electrons concentrated over a small area. Saturation effects have been carefully investigated and found not important at least up to the maximum drift time which is in our case about 4 μs.

Although such a read-out insures a true (two dimensional) isotropy, the best accuracy is obtained by a measurement of the drift time. Therefore planes have been arranged in such a way as to insure that tracks coming from the diamond do not exceed 45^{o} angle respect to the electric field direction.

The photon and electron detector surrounds the track sensitive chambers over the largest possible fraction of the solid angle. It is designed in order to achieve:

(i) detection of photons and a measurement of their energy by total absorption;

(ii) a measurement of the energy of high energy electrons(primarily from W^{o} and $W^{\pm}$ decays)with the best possible accuracy;

(iii) electron identification in the presence of hadronic background which is expected to be several orders of magnitude more abundant.

The detector is a fine grain calorimeter made of many plates of

short radiation length and which measures samplings of the total energy deposited by the electromagnetic cascade. Homogeneous shower detectors like Lead Glass or Sodium Iodide blocks have been discarded because they seem less well adapted to the present application. Their major disadvantages are: (i) the difficulties in reconciling longitudinal segmentation in order to probe the shower development at different depths with a compact geometry; (ii) their sensitivity to radiation damage which could be substantial inside the SPS tunnel during normal operation; (iii) the requirements on the phototubes, which must be located immediately behind the crystal and finally (iv) the prohibitive cost of a 70 m^2 detector. On the other hand it is generally accepted that the energy resolution of an homogeneous detector can be realised also with a sampling calorimeter provided sufficient large number of plates is used[65].

Several major detectors for colliding beams now under construction throughout the world have chosen liquid Argon to measure electromagnetic energy depositions. Our initial design considerations have also been orientated towards a cryogenic liquid Argon detector because of its potentially greater uniformity between cells and the accurate calibration procedure[66]. Engineering studies have shown that such a detector is feasible only at the cost of considerable complexity and substantial solid angle losses due to cryostats and supporting structures.

Recently a new type of shower counter has been described[67]. The device is conventional in the sense that it uses lead scintillator sandwich for detecting the shower energy. However a novel light collection technique is employed in which the scintillation light produced in inexpensive plastic scintillation slabs crosses an air gap into a thin plastic sheet doped with a wave-length shifting organic compound. This technique has been shown to be capable of an energy resolution which is at low energies the same as with liquid Argon. However at higher energies, the ultimate resolution might be slightly worse since it could be masked by calibration in the PM's. The main advantage of this technique is that it permits to construct counters which are less expensive and more convenient to build and operate

than liquid Argon shower detectors, since the lead plates do not have to be self-supporting and, most important, they require no cryogenics. It is easy to split the counter in several sections in order to achieve a satisfactory separation between hadrons and electrons; several shifter sheets may be brought out separately, each one looking at different sections of the shower counter. Finally space can be made between the layers of the stack and track chambers inserted whenever required to provide improved position resolution and separation between multiple hits. This can be done with little or no sacrifice in energy resolution.

The hadron calorimeter is necessary for several important reasons, some of which mentioned already:

(i) the energy flow measurement for configurations where the particle densities are too large for magnetic analysis of individual tracks;

(ii) the results of the Tien-Shan experiment indicating the onset of a more penetrating hadronic component for centre of mass energies $\gtrsim$ 500 GeV;

(iii) the possibility of separating electrons from accidental overlaps of a charged particle and a photon on the basis of the longitudinal energy deposition;

(iv) to realise an effective measurement of missing transverse energy to identify large transverse momentum neutrinos (for instance from $W^{\pm}$ decays);

(v) to trigger on specific energy depositions, jets and so on.

It is known that the best hadronic calorimeters are uranium compensated devices. After several initial investigations we have discarded this solution because of its cost and complexity. We prefer instead simply to instrument the iron yoke of the magnet with plastic scintillators and a technique rather similar to the one already discussed for the electromagnetic detectors.

Two ways of identifying muons have been considered, both based on the absence of interactions. The first one observes the apparently rectilinear tracks after traversing a considerable amount of material

(EMI). A non-interacting track is defined as a track which is compatible with spatial deviations due to Coulomb scattering alone. For particles at high energies, the mean free path for interactions identifiable in this way becomes considerably larger than the collision mean free path. Although wasteful in terms of absorber, this scheme is simple and of proven effectiveness. The second method is based on a hadron calorimeter in which the track is sampled periodically. A muon is defined as a track which loses energy compatibly with electromagnetic processes only (ionisation). Since almost all hadronic interactions lead to anomalous energy depositions in the calorimeter, this method gives a detectable collision length close to the true length, and it is particularly effective at high energies (which is our case).

The angular range below 5^{o} (and above 175^{o}) respect to the beam line is either badly or not covered at all by the chambers of the central detector. In this angular range one does not expect decay particles for instance from W decay but rather the 'spectator' jets produced in association with the central event. It is however worth while to retain some sensitivity over that region in order to get a more complete understanding of these features of the events. For these reasons we have decided to install very simple forward detectors downstreams of the main spectrometer.

Finally in order to know the luminosity we would like to follow the generalised Van der Meer method[68]. Two very small telescopes subtending angles around 1 mradian are required (luminosity telescopes). These devices can also be used in coincidence with the main spectrometer in order to study Pomeron-Pomeron collisions.

3.3. THE SET-UP. We now give a brief overall description of the set-up. The detailed discussions of the technical aspects of each of the components are given in the following chapters.

We shall refer to Figure 3.1. The complete detector is about 10 m long and 5 m wide. The magnet is a dipole of nominal field value of 0.7 Tesla and it has an internal magnetic volume of 80 m^3 (7.0 x 3.4 x 3.4 m^3). The coils [5] (numbers refer to Figures 3.1 and 3.2) are made of Aluminium in order to minimize the number of collision

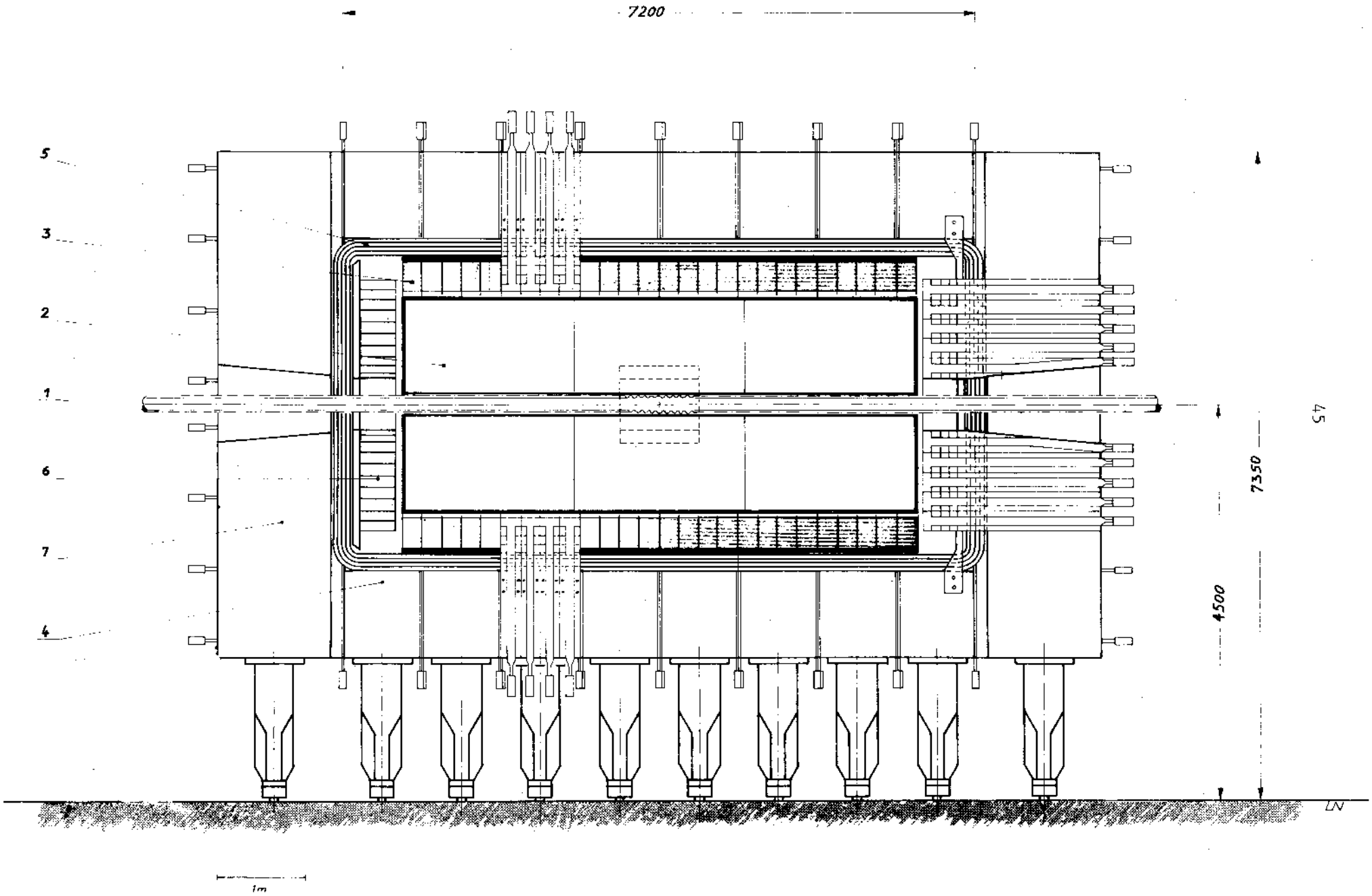

Figure 3.1. Side view of the detector. Legend: |1| vacuum chamber; |2| vertex chambers; |3| electromagnetic (e.m.) detectors; |4| hadron calorimeters and return yoke; |5|Al coil; |6| forward e.m. detectors; |7| end caps.

lengths. They are 13 cm thick and weigh about 25 Tons. We have chosen a rather conservative current density of $5A/mm^2$ giving a total dissipated power of 5.8 MW. The total thickness of the instrumented iron yoke is 96 cm and it is subdivided into 16 C-shaped elements [4] each one about 90 cm wide and of about 52 Tons. Each element can be in principle removed independently with its own instrumentation (hadron calorimetry).

The chambers of the central detector [2] are of drift type with image read-out. The third coordinate is obtained by current division. The sensitive volume around the vacuum pipe [1] is roughly a cylinder about 6 m long and 1.22 m radius. It can be separated in 6 blocks which can be easily removed and replaced with another standard element in case of failure. All wires travel along the horizontal plane. The wire spacing is 3 mm and the maximum wire length is 2.5 m. Since we plan to used 40 μ wires, this span can be covered without supporting wires. The drift distance is 20 cm and it is matched to the time lag between bunches, i.e. the collection of electrons must be completed before the next crossing takes place. We hope to achieve a spatial resolution of 250 μ on each wire, and a longitudinal localization to about ± 1% of its length. The large number of points measured on each track makes it possible to determine the ionisation of tracks down to ± 6%.

The chambers are surrounded by an electromagnetic calorimeter [3] of lead-scintillator type, about 30 radiation length deep. The calorimeter is segmented in 52 half-moon gondolas which have an internal radius of 1.3 m, a width of 22.5 cm, corresponding to four gondolas for each magnet unit [4]. They weigh about 1.8 Tons each. A scintillation counter is mounted in front of each gondola for dE/dx and time of flight measurements. The thickness of the lead-scintillator stack is about 36 cm. Each gondola can be separately removed. Similar units [6] cover the end caps. They are segmented in ten angular ranges of a width modulated to achieve iso-rapidity gaps over the radii between 30 cm and 1.2 m. The total number of phototubes required by a fourfold segmentation in depth of the gondolas and localization by pulse division in both coordinates is $\sim$ 832. Additional 320 tubes are

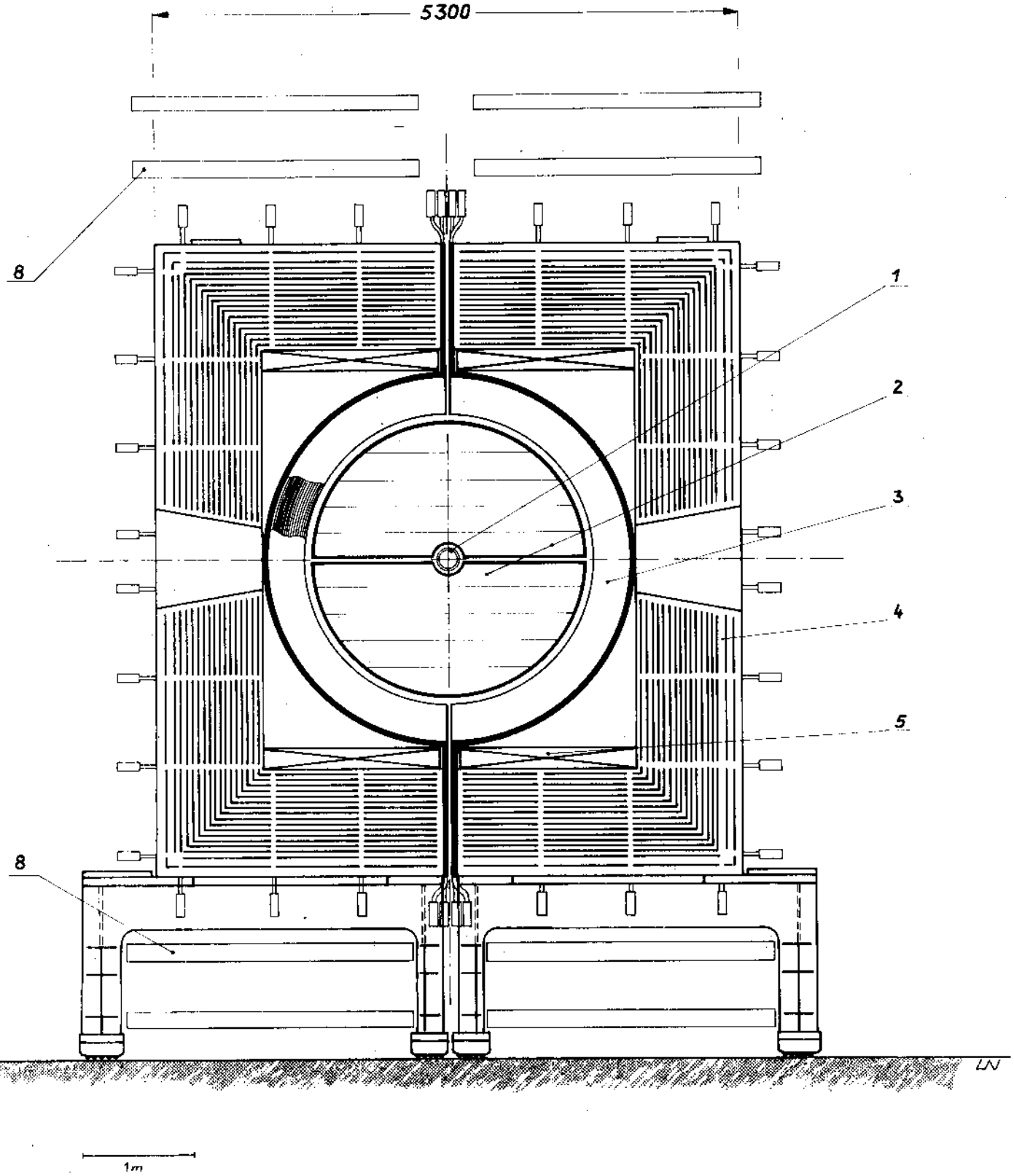

Figure 3.2. Cut view of the detector. For legend see Figure 3.1. Note that the muon detectors [8] are shown for clarity only on top and bottom of the magnet and not on the sides (nor in Figure 3.1).

needed for the end-caps. The hadron calorimeters are actually built inside the magnet C's [4] and end-caps [7]. There are in each of the C's ten subdivisions in ϕ. In total there are 8 subdivisions in θ, one for each one of the C's. The standard scintillator plate size is 88 x 80 x 0.7 cm^3. About 2000 m^2 of scintillator are needed. The total number of phototubes for the C's is 640. The two end caps (270 Tons) are instrumented with about 360 tubes and 1000 m^2 of scintillator.

The detector can be easily opened by rolling the two halves of the magnet apart (Figure 3.3). In this way the chambers are made immediately accessible. PM's can be replaced easily with a quick disconnect technique. The rest of the detector is very rugged and should need only very rarely direct maintenance. Table 3.1 lists some relevant parameters.

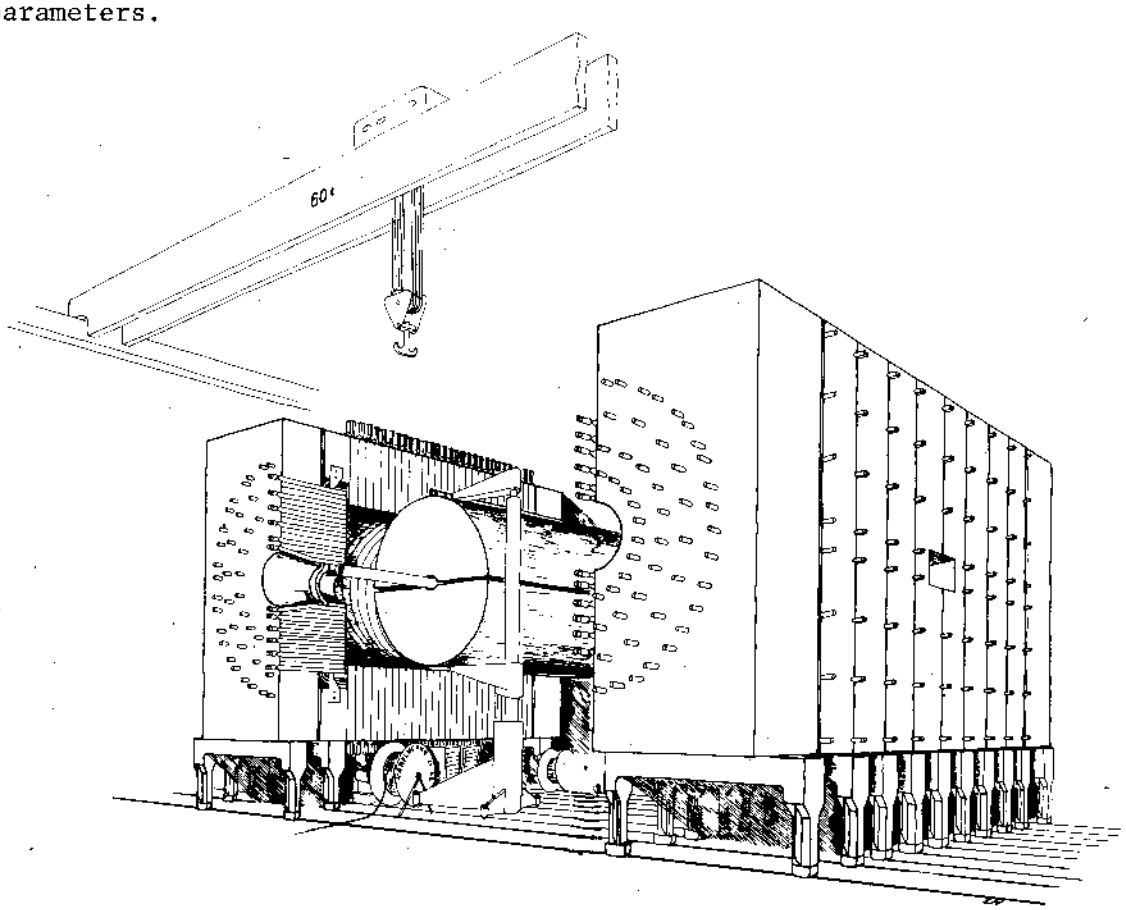

Figure 3.3. Artist's view of detector showing access to the central chambers.

TABLE 3.1. Parameter list

A) MAGNET

Field	Type	dipole
	Nominal value	0.7 Tesla
	Inside magnetic volume	80 m^3
	Dimensions	7.0 x 3.4 x 3.4 m
Coils	Number	2, flat
	Material	Aluminium
	Thickness of conductor	13 cm
	Total mass of conductor	25 Tons
	Current density	5A/mm^2
	Dissipated power	5.8 MW
Iron	Thickness	80 cm
	Effective thickness of return yoke (instrumented)	96 cm
	Weight	830 Tons
	External dimensions (length x width x height)	7.2 x 5.3 x 5.7 m
	Subdivision in C-shape elements	
	- total number	16
	- width	90 cm
	- weight	52 Tons

B) CENTRAL DETECTOR CHAMBERS

Type		drift, image read-out + current division
Sensitive volume (cylinder around beam pipe)		
	- length	6 m
	- R_{min}/R_{max}	0.10 to 1.22 m
Number of separate elements (half cylinder of L $\sim$ 2 m)		6
Wires	- wire spacing	3 mm
	- wire length	0.8 to 2.5 m
	- drift length	20 cm
	- total number of sense wires	10,700

B) CENTRAL DETECTOR CHAMBERS

Performance/accuracy	
- time measurement (for sagitta)	250 μ
- pulse division (localization)	1% of wire length
- ionisation measurement	± 6%
- 2 track resolution	2.5 mm

C) EM CALORIMETER

General description	
- type	Lead scintillator sandwich
- thickness	30 r.ℓ.
- lead plate thickness	2 mm
- stack thickness	36 cm
Scintillator plates	
- material	PLEXIPOP
- thickness	2 mm
- attenuation length λ_o	20 cm
Light collection pipes	
- material	acrylic, BBQ doped
- thickness	4 mm
- attenuation length λ_o	$\geq$ 3.5 m
Large angle units	
- shape	half moon ('gondola')
- internal radius	1.3 m
- width	22.5 cm (4 per iron C)
- weight/unit	$\sim$ 1.8 Ton
- number of units	52
- number of PM's	832
End cap units	
- shape	half moon
- internal radius	0.3 to 1.7 m
- weight/end cap	$\sim$ 12 Tons
- number of units/end cap	10
- number of PM's	320
Performance/accuracy	
- resolution	$10\%/\sqrt{E}$
- track localization (pulse division)	$\sim .05\ \lambda_0/\sqrt{E}$
Front scintillator counters	
- number of PM's (2 x (52 + 20))	144

D) HADRON CALORIMETER

General description	
- type	Iron scintillator sandwich
- iron plate thickness	5 cm
Central part (magnet iron C-shape units)	
- number of subdivision in θ	8
- number of subdivisions in ϕ	20
- standard scint.plate dimensions	88 x 80 x 0.7 cm^3
- total scintillator needed	2000 m^2
- number of PM's	640
2 end caps (4 independent half-moons)	
- outside radius	3.0 m
- inside radius (forward hole)	0.35 m
- thickness - iron	1.25 m
- total (instrumented)	1.50 m
- weight/end cap	270 Tons
- total scintillator needed	$\sim$ 1000 m^2

E) MUON DETECTOR

General description	
- type	drift tubes
- location	around dipole and end caps
- total surface covered	350 m^2
- number of layers	2
- number of planes of drift tubes per layer	4 (2)
- distance between layers	.6 - 1 m
- dimension of one drift tube	(.05) X (.05) X (3 - 5)m^3
- spatial resolution	.5 - .7 mm
- time resolution	$\simeq$ 20 ns

4. MAGNET

4.1. DESIGN. The physics considerations outlined in the preceding chapters govern the design of the dipole within limitations dictated by economics and common sense. More specifically:

i) The analyzing power, $k = B\ell^2$ where ℓ is the useful transverse dimension of the track detector inside the magnet (and $K = BL^2$ for the longitudinal dimension L) should be as big as possible. A minimum value of 1 $T.m^2$ is desirable, if it can be reached for reasonable dimensions of the magnet and an acceptable value of the electric power.

ii) For the purpose of calorimetry, the thickness a of the metal of the coil should be a rather small fraction of an interaction length, leaving the main part of the calorimeter in the yoke. The iron thickness f of the return yoke should be about 80 cm, which, added to the other materials (electromagnetic shower detector, coil, scintillators), would represent more than 6 absorption lengths, λ_a (the iron should be made of plates separated by gaps, so that the geometrical thickness is about 1.2 f).

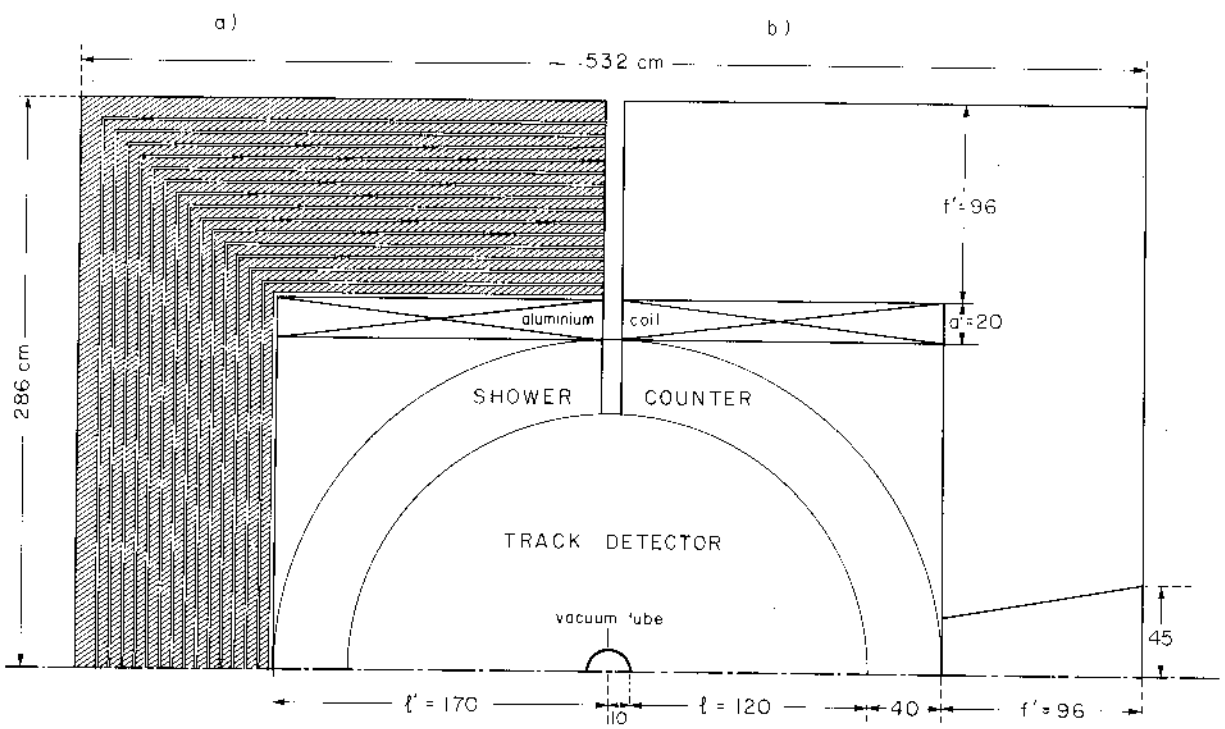

Figure 4.1. Transverse cuts of the magnet a) through a standard section, showing the disposition of the iron plates, b) through the median plane, showing the horizontal window along the field direction.

The thickness of the coil is minimized by using Aluminium rather than Copper, since 13 cm of Aluminium represent only 0.34 λ_a instead of 0.56 λ_a for the 8.2 cm electrical equivalent of copper, and by distributing the coil evenly around the inside field volume.

This leads to the ''warm-coffin'' design illustrated in Figure 4.1, which has also the advantage of providing a very uniform field. The coil is made of two vertical rectangular halves; the small gap between these two halves (and the horizontal parts of the iron yoke) is needed for the light collectors from the e.m. shower counters and allows the yoke to be physically separated into two parts, thus providing access to the inner detectors.

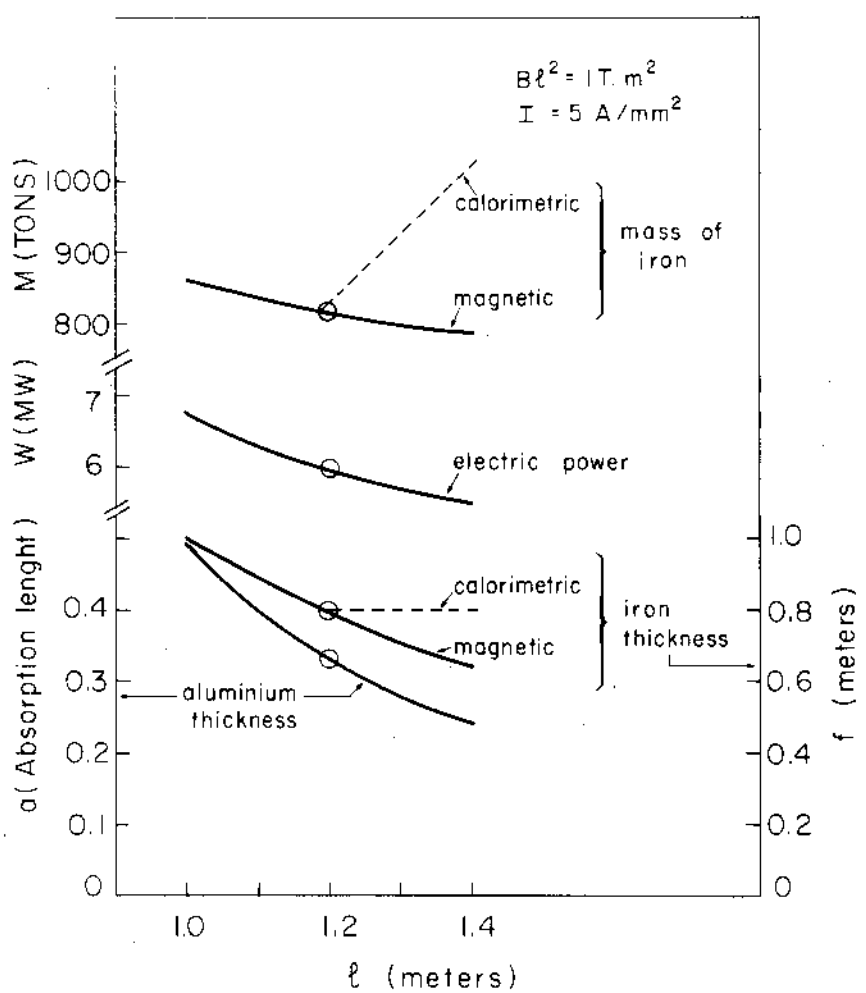

Figure 4.2. Variation of the magnet characteristics, at fixed analyzing power $B\ell^2$ and current density I, with the useful transverse dimension ℓ.

4.2. CHARACTERISTICS. The aspect ratio L/ℓ being fixed to 2.5 (see chapter 3), the physical parameters which remain free are the inside transverse dimension, $\ell' = \ell + 0.5$ m (the 0.5 m is needed for the vacuum tube and the shower detector) and the field B. They should be chosen in such a way as to provide a good analyzing power $k = B\ell^2$ with optimized values of the electric power W, the total mass M of iron required (either for magnetic or for calorimetric purposes), and the thickness a of Aluminium in the coil.

Fig. 4.2. shows the variation of these characteristics as a function of the useful transverse dimension ℓ, when the analyzing power is fixed at 1 T.m^2 and the current density in Aluminium is set equal to the acceptable value I = 5 A/mm^2. Due to the better use of the inside magnetic volume, the three variables W, M (magnetic) and a, slowly decrease when ℓ increases. However, at $\ell > 1.2$ m, the minimum thickness of iron required for the magnetic flux return becomes less than the 80 cm required for calorimetry and at constant thickness the total mass of iron would skyrocket when ℓ increases. We therefore should choose this value $\ell = 1.2$ m, if the other characteristics have acceptable values.

At $\ell = 1.2$ m, the electric power is around 6 MW, which seems reasonable for an installation which will presumably be used for about 12% of the time; it also allows the use of the power supply of the 2 metre HBC.

The necessary thickness of Aluminium is about 13 cm, equivalent to .34 interaction length (or 6 cm of iron), which allows to consider the coil as the first plate of the hadronic calorimeter. Finally the value of the magnetic field B = .7 T is adequate for good operation of the inside drift chambers (see chapter 5).

Thus the choice $\ell = 1.2$ m ($\ell' = 1.7$ m) leads to a satisfactory solution of the various constraints. The final list of parameters is given in Table 4.1, where the current density I and hence the total current i and the power W have been adjusted so as to yield an average field value of 0.7 Tesla inside the measurement volume ($z^2 + y^2 < 1.3^2$ m^2).

For this purpose the field has been calculated by the computer program Fatima[69] with input data representing the quality of a standard

TABLE 4.1. Parameters of the magnet

Nominal field value	B_o	0.70 T
Transverse analyzing power	$k = B_o \ell^2$	1 T m^2
Longitudinal analyzing power	$K = B_o l^2$	~ 6.0 T m^2
Inside magnetic volume, dimensions:		
(i) Transverse	$2\ell'$	3.4 m
(ii) Longitudinal	2L'	7 m
Total current in each half coil	i	1.03 10^6 A
Coil material		Aluminium
Thickness of conductor	a	13.0 cm
Total space for coil	a'	20 cm
Current density in aluminium	I	4.81 A/mm^2
Total mass of conductor		~ 25 Tons
Total dissipated power		5.88 MW
Total thickness of iron (magnetic)	f	80 cm
Width of return yoke (instrumented)	f'	96 cm
Weight of iron (magnetic)	M	~ 830 Tons (*)
Overall external dimensions:		
(i) Length		7.40 m
(ii) Height		5.72 m
Dimensions of windows at 90° (on external iron surface)		.9 x .9 m^2
Dimension of forward openings in the coil		ϕ = .70 m

(*) End caps not included

low-price iron ($\mu \simeq 150$ at B = 1.8 Tesla), and the exact configuration of the iron plates (14 plates of 5 cm separated by 1 cm gap and followed by a last plate of 10 cm), as well as the vertical slit already mentioned and, in the median plane, two windows of 0.9 m vertically (about $\pm 10^{o}$ in azimut) to provide escape for particles emitted at $\theta \sim 90^{o}$ along the magnetic field.

The field lines displayed in Fig. 4.3. illustrate the good uniformity of the field. In the median transverse plane, where the field is slightly perturbed by the horizontal window, its calculated values depart at maximum by 5% from the average field inside the periphery of the track detector, and by less than 1% in 80% of that area. These numbers are even better for a section without window.

4.3. STRUCTURE OF THE MAGNET. The total length of the iron yoke being 7.2 m and the total weight of iron about 830 tons, a possible structure consists in dividing each half of the magnet into 8 vertical C-shaped sections, 90 cm wide, each weighing about 55 t.

A schematic design of such a C-section is displayed in Figure 4.4. It is made of 15 iron plates (14 plates 5 cm thick, followed by an external one 10 cm thick) separated by 1 cm gaps. The plates are bound together by transverse rods, disposed in longitudinal rows about every 80 cm along the periphery of the C. This reinforcement structure, which insures rigidity of the unit, subdivides the C in 10 cells, ~ 90 cm long, ~ 80 cm wide and 94 cm thick in which the scintillators can be inserted from both lateral sides. A space of 2 cm is left free between the internal horizontal faces of the C and the coil, both to provide room for supporting the coil and to insert a first layer of scintillators. The vertical extreme faces of the C, facing the opposite C, are covered with 4 22.5 cm wide iron plates, which are the supports for the internal shower counters (see chapter VI). Each C is mounted on guided rollers of the type used in the NA4 experiment (see Fig. 3.1).

The modular C-structure of the whole magnet is shown in Fig. 4.5. (see also Fig. 3.1). It has the following advantages:

- each C can be completely mounted, including its detection equipment, before being brought near the intersection for final assembly of the magnet.

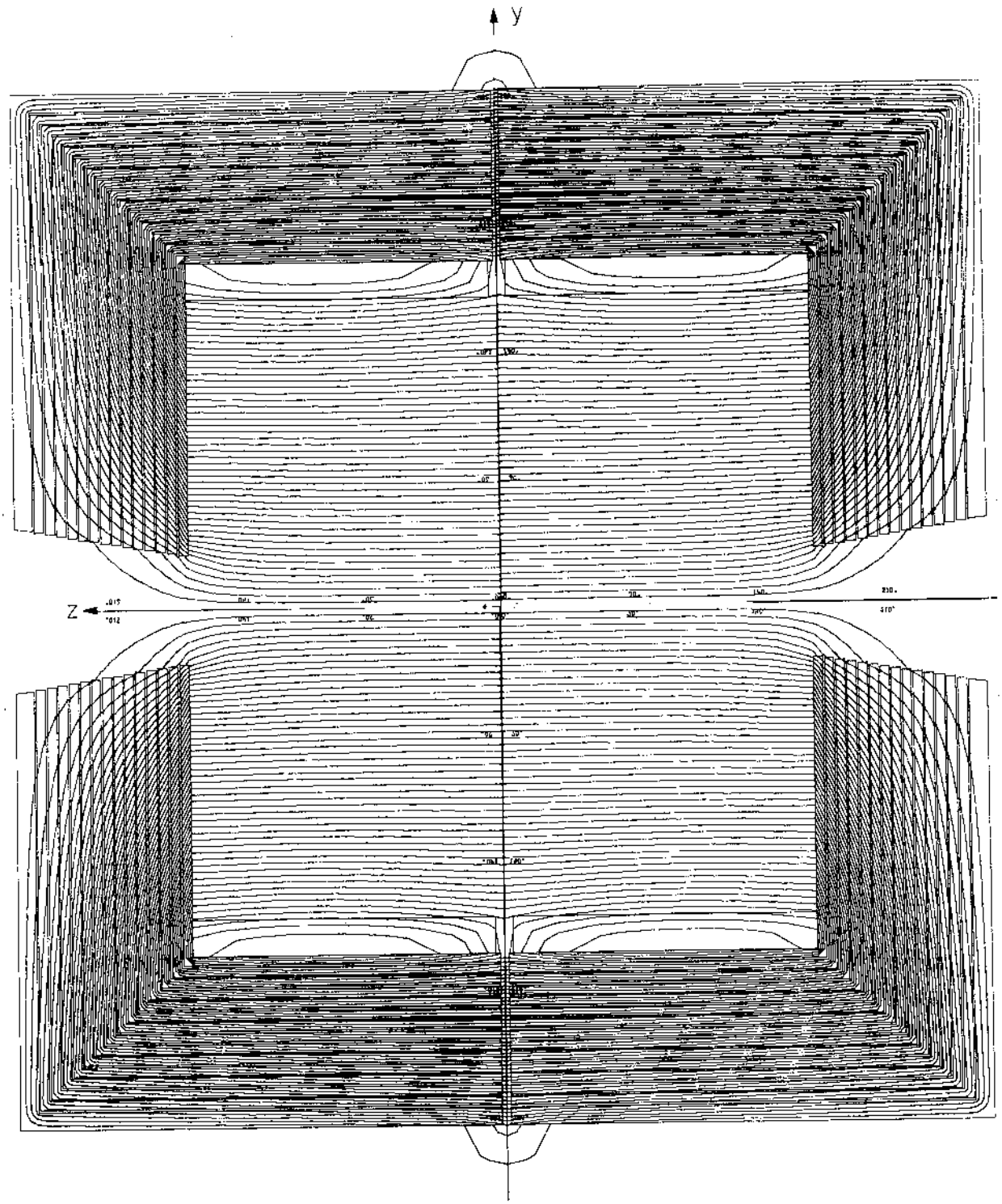

Figure 4.3. Field lines in the median transverse plane of the magnet. Note the good uniformity of the field in the area covered by the track detector (a circle of radius $\sim$ .8 the half width of the dipole) and the lack of appreciable fringing field, except near the vertical slit.

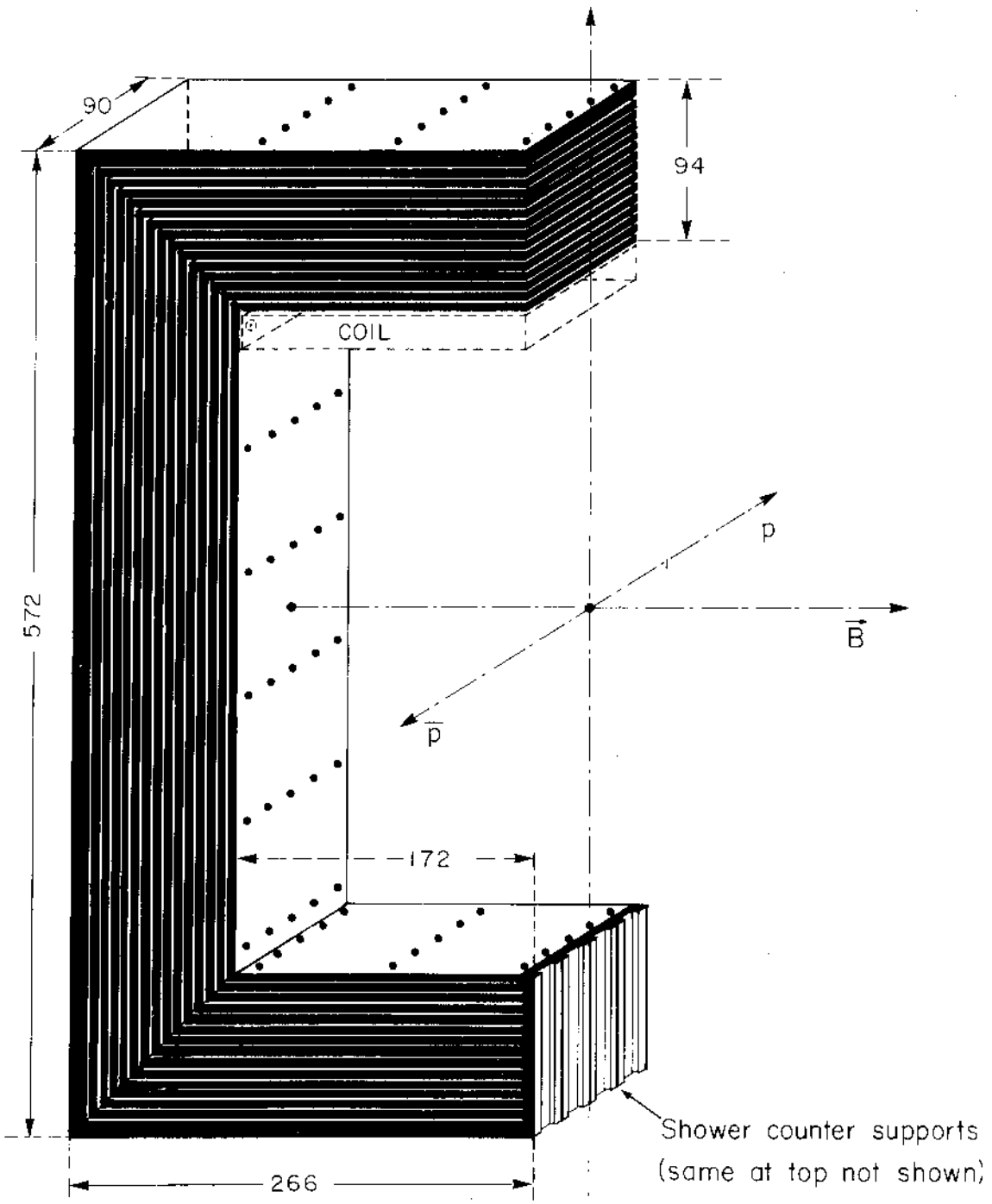

Figure 4.4. Perspective view of a C-section. The black dots represent the ends of the reinforcement bars.

- each C can eventually be removed independently (see Fig. 3.1) from the other ones to allow repair or replacement of the scintillators, which are accessible from the vertical sides of the C.
- each of the two halves of the magnet (8 C's bound together) is movable horizontally as a single unit, to allow the magnet to be opened and to provide access to the internal detectors.

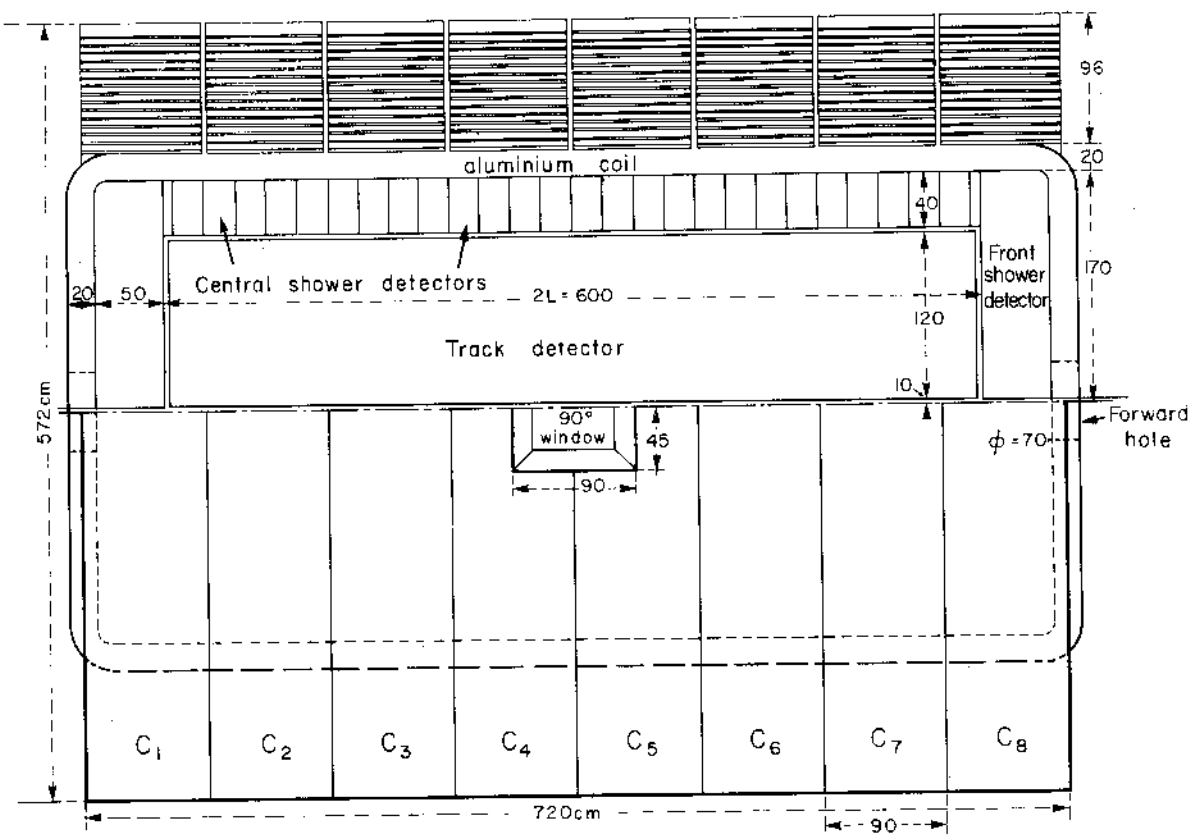

Figure 4.5. The upper half is a vertical cut along the beam axis, the lower half a side view of the whole magnet, showing its segmentation in 8 C-shaped sections.

4.4. COMPENSATION

DIPOLAR EFFECTS. The dipole field is to be compensated locally by means of two dipole magnets on either side of the experimental magnet such that the total integrated field along the beam axis is zero. The compensating magnets could be beam transfer magnets in the beginning with $\sim$ 1.5 T field and $\sim$ 1.6 m length each. The amplitude of the

vertical orbit bump at 270 GeV reaches the following values,in the centre and at the edges of the experimental magnet:

TABLE 4.2. Amplitude of the vertical orbit bump.

Distance (m) (centre exp.magnet-centre compensation)	Amplitude (mm) (centre)	(edge)
4.5	12.2	2.7
5	13.6	4.1
6	16.3	6.8
7	19.	9.5
8	21.8	12.2
9	24.5	15
10	27.2	17.7
11	29.9	20.4
12	32.6	23.1
13	35.4	25.8

The effects of this bump should be local assuming perfect dipolar fields. The magnets will only be switched on after acceleration since probably the time constant of the big magnet will be too long to be able to follow the machine magnets during acceleration. Also the higher order effects are attenuated at higher beam momentum. Switching on the set of magnets (dipole and compensators) necessitates a time which is long with respect to their largesttime constant e.g. probably several minutes with time constants of the order of 10 seconds (SFM fundamental mode: 13 seconds).

QUADRUPOLE EFFECTS. Quadrupole components create time shifts, amplitude beating and changes of the horizontal momentum compaction[70]. Because of the holes in the forward direction and because of the horizontal window at 90^{o} the proposed dipole has quadrupole components. From two dimensional field computations the integrated gradient

$\Delta(G\ell) = \int_{\ell_1}^{\ell_2} G(\ell)\, d\ell$ is estimated to be at most 2 x 0.3 T and $\sim$ 0.015T in the centre.

Taking these figures and the properties of the proposed low beta insertion (71) we obtain for the amplitude beating:

$$\left(\frac{\Delta\beta}{\beta}\right)_{H,V} = \frac{1}{2 \sin 2\pi Q_{H,V}} \frac{0.3}{p_{beam}} \beta_{H,V}^{pevt} \Delta(G\ell)$$

yielding, with $Q_H \tilde{\sim} Q_V \tilde{\sim} 26.6$ [71]:

$$\left(\frac{\Delta\beta}{\beta}\right)_V < 4\%$$

$$\left(\frac{\Delta\beta}{\beta}\right)_H < 2.5\%$$

For the tune shift we obtain:

$$\Delta Q = \frac{1}{4\pi} \beta_{H,V}^{pevt} \Delta GL \frac{0.3}{p}$$

$$\Delta Q_V < 4 \times 10^{-4}$$

$$\Delta Q_H < 2 \times 10^{-4}$$

Finally the variation of the horizontal momentum compaction is zero because the momentum compaction is zero in the low beta insertion.

At the ISR an amplitude beating of several percent and a tune shift of the order of $\Delta Q \lesssim 10^{-3}$ is considered to be admissible.

5. CENTRAL DETECTOR

5.1. INTRODUCTION. With the $p\bar{p}$ collider we are entering a new energy regime and we must be prepared to measure events which are made complex by the high particle multiplicities. Hence we need a device which is capable of measuring such topologies. Such a device, the drift chamber with image readout[72], has recently been developed for this purpose and has the following properties:

1) Good pattern recognition capabilities of large charge multiplicities which is provided by the high density for information recorded and the good two track resolution.
2) Good momentum and directional measurement of individual tracks.
3) The feasibility of mass measurement of some particles through the measurement of dE/dx. Fractionally charged particles can be detected from their energy loss which is proportional to the square of the particle charge.
4) Relatively few wires for the large volume covered.

While providing all these advantages, the technique we propose is only a simple extrapolation of a completely known technology.

5.2. BASIC CONFIGURATION

5.2.1. GENERAL PARAMETERS. The central detector is a self supported cylinder 6 m long and 2.6 m in diameter. This cylinder is split along the horizontal diameter and into three 2 m sections along the beam pipe making 6 half moon sections as shown in Figure 5.1. The middle sections will be referred to as a the central chambers and the other sections as the forward chambers. The magnetic field and the drift wires are horizontal and the beam pipe traverses along the axis.

The cylinder of these chambers is prestressed and made of a vetronite shell separated with honeycomb. This design combines a maximum of rigidity with a minimum of radiation length of material. The horizontal members are of similar material and provide additional support to prevent rotational distortions about the beam axis. The half moon sections are separated by a thin mylar window such that they can be treated as completely independent chambers each with an individual

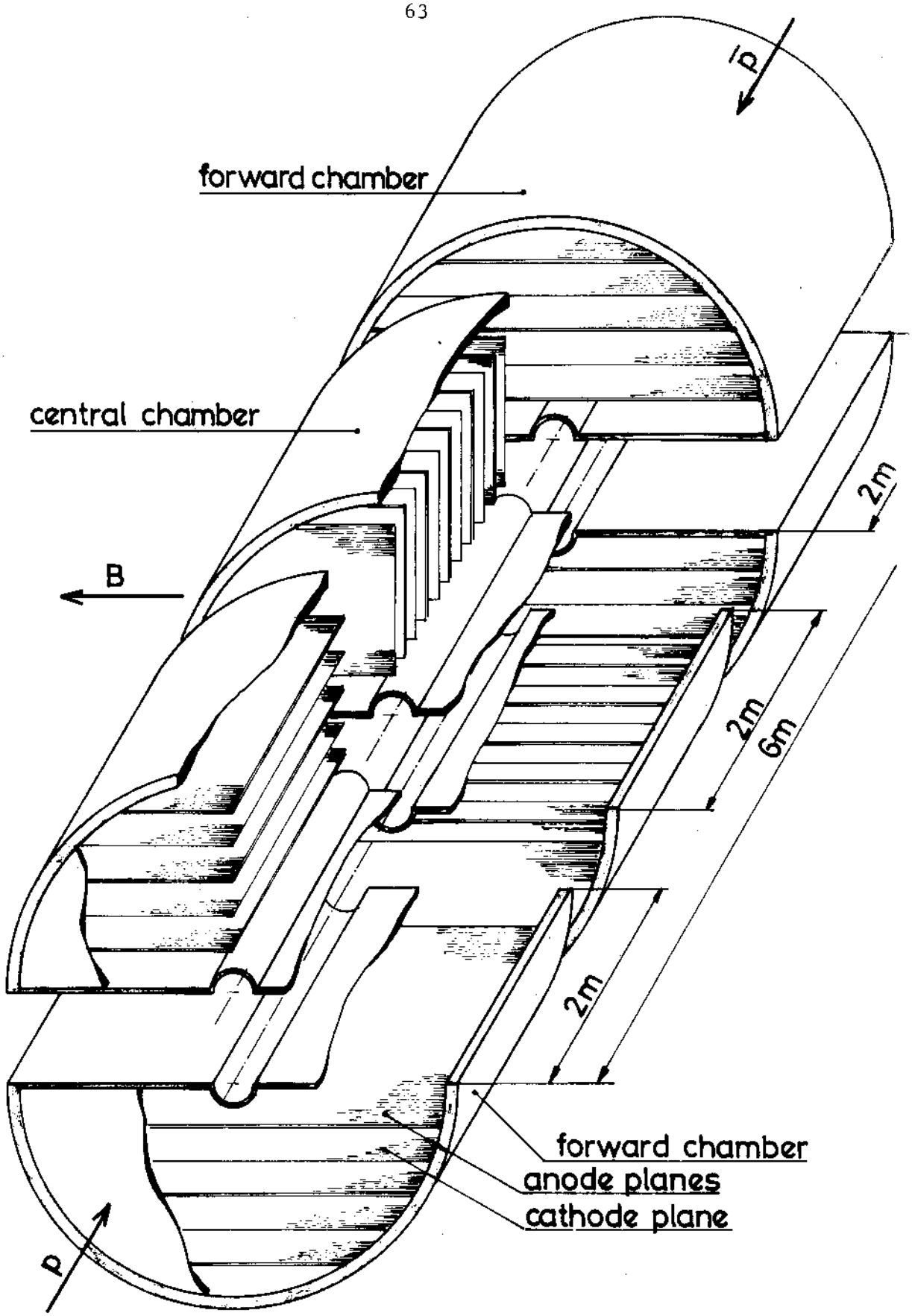

Figure 5.1. Cut-away diagram of central detector showing the orientations of the wire planes in the central and forward chambers.

gas supply. This modularity has many advantages both in construction and maintenance.

The basic cell we propose to use consists of a bidimensional proportional chamber onto which electrons created in the gas are drifting. An electric field is applied in the drift space by a cathode parallel to the plane of sense wires and suitable field electrodes at the volume boundary. The three coordinates of a space point on a track crossing the chamber will be given by:

a) the time of arrival of electrons
b) the position of the sense wire on which it arrives
c) the pulse sharing between the two ends of the sense wire.

Solution c) was prefered to a cathode readout because it provides space points directly which will decrease the number of ambiguities for pattern recognition.

The drift distance has been fixed at 20 cm for the following reasons:

1) the maximum drift time of 4 μs is well matched to the bunch crossing frequency
2) space charge problems vary as the cube[76] of the distance and become manageable for 20 cm (see section 5.4.2).

Table 5.1 lists the main parameters of the chambers.

5.2.2. WIRE ORIENTATION. The wires of the chamber are arranged in the so called quadrupole configuration[75]; two planes of wires 3 mm apart alternating grounded anode sense wires of 40 μ.diameter and cathode field wires of 100 μm diameter. This configuration has two advantages:

1) drift electrons cannot cross this plane and hence there is no left right ambiguity. However the sampling frequency is reduced to once every 6 mm
2) it allows the wires to be unsupported over their maximum length of 2.5 m. Extrapolation from tests we have done show that their movement can be limited to less than 300 μm provided we load the 40 μm sense wires to 160 g.

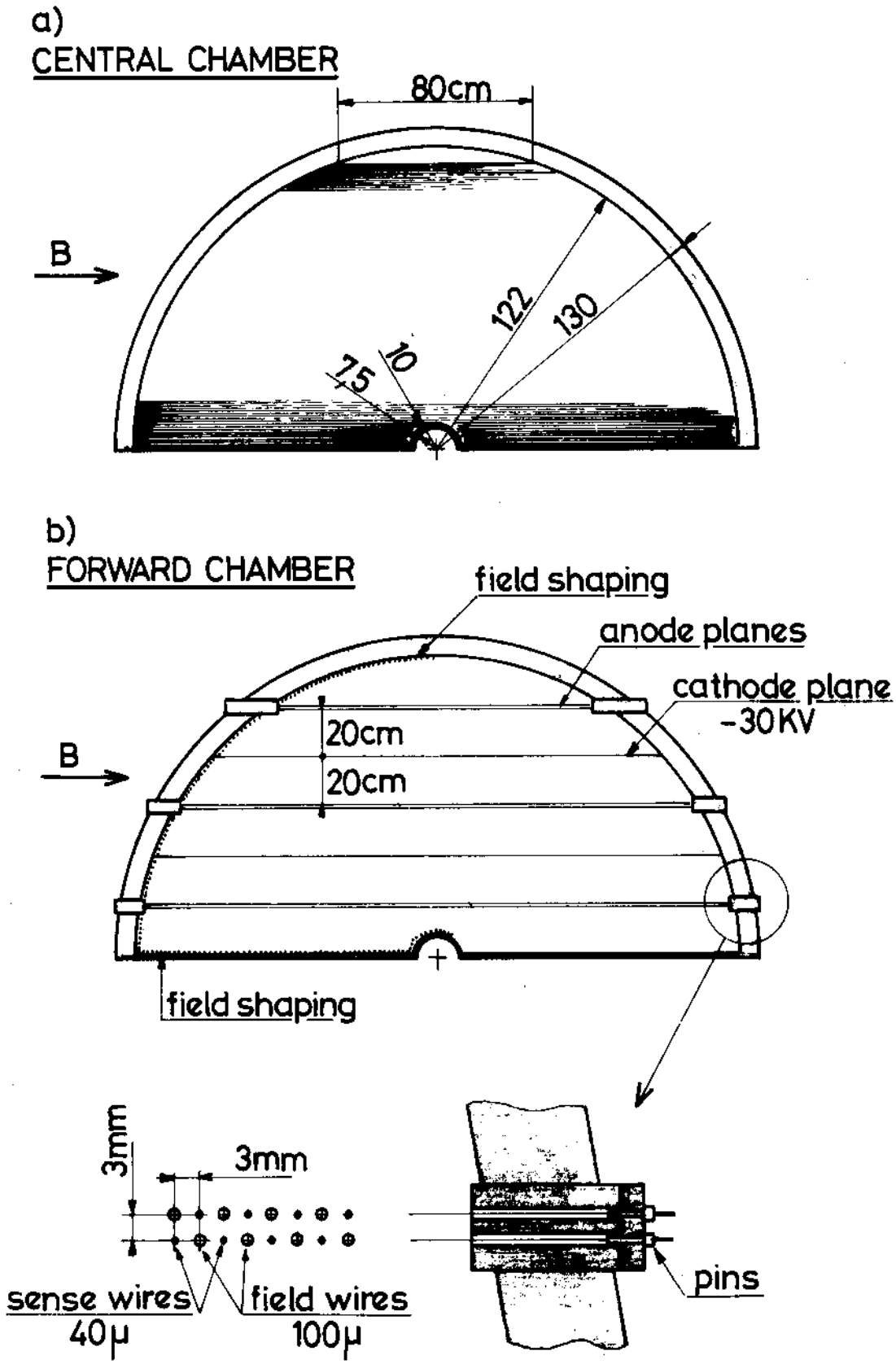

Figure 5.2a) Vertical section of a central chamber.

b) Vertical section of forward chamber.

Although our chambers are fully sensitive to all tracks, whatever their direction is, we choose to orient the sense wires along the magnetic field direction in order to make full use of the drift time for momentum measurement.

a) CENTRAL CHAMBERS. The planes of wires are in the vertical direction and the electrons drift in the horizontal direction. Figure 5.2a) shows a vertical section through a plane of sense and field wires. The magnetic field is horizontal and the electric field and beam pipe are into the paper. The wires extend from 0.10 m to 1.15 m vertically and are 2.44 m long at the bottom and 0.80 m long at the top. Below 0.1 m there are planes of similar wires each side of the beam pipe. There is a measurement hole below 10^{o} to the magnetic field (horizontal) direction. This corresponds to ± 0.30 m at the inner edge of the return yoke. The measurement of particles in this direction is discussed below. There are 5 pairs of sense and field wire planes at 0.40 m intervals with cathode wire planes at ± 0.20 to these planes. Hence a volume extending ± 1.0 m along the beam pipe is covered by these chambers.

b) FORWARD CHAMBERS. In the forward chambers the planes of wires lie in the horizontal direction and the electrons drift in the vertical direction. Figure 5.2b) shows a vertical section perpendicular to the beam pipe through the forward chambers. The magnetic field is horizontal and the electric field in the vertical direction. The wires extend from ± 1.10 m to ± 2.9 m along the beam pipe either side of the central region respectively. The cathode and sense wire planes are again separated by 0.20 m. As shown in Figure 5.2b) there are 3 sense wire planes at 0.20, 0.60 and 1.0 above the beam axis which have 2.40, 2.12 and 1.40 m long wires respectively. Electric field shaping near the edge is provided by applying the appropriate voltages to a series of electrodes etched onto the vetronite wall of the detector. At the beam pipe, field shaping is provided by similar electrodes.

5.3. ELECTRONIC CIRCUITS. The electronic readout should record all the useful information without producing such a large number of bits as

to be too expensive to process. The actual required information is of two types: the timing of the leading and trailing edges of the pulse to an accuracy of about 4 ns, and the determination of the total charge if the pulse has minimum length or for longer pulses a sampling of the integrated charge every 50 ns corresponding to 2.5 mm drift lengths.

Two different systems have been considered. The first is based on the storage of information in analogue form by a charge coupled device (CCD)[73].

A conservative approach is to convert the pulse amplitude into digital information sufficiently rapidly to accumulate samplings at a 20 MHz rate. A device has been described[74] which combines the integration and an amplitude to time conversion. The input signal is converted to a current pulse which is then switched at 50 ns intervals between 2 identical circuits. During one such interval the charge is integrated on a storage capacitor and during the next it is discharged at a constant rate and the discharge time is digitized with a 160 MHz clock. The 2 circuits are out of phase, so that when one is digitizing, the other integrates the next sampling. It can be seen that this scheme has the capability of recording multiple track hits on any wire provided that there are separated by more than 2.5 mm.

5.4. PERFORMANCE OF CHAMBERS

5.4.1. RESULTS OF TESTS. Two chambers each having a drift gap of 0.20 m have been tested successfully at the PS[72]. One of these was mounted inside a magnet in order to determine the drift angle with respect to the electric field as a function of the electric and magnetic fields. The results as shown in Table 5.2 imply a drift angle of 22^{o} for a magnetic field of 0.7 T and an electric field of 1.5 kV/cm.

In addition to the results of these tests, a large amount of information is available from similar multi-sense wire drift chambers currently used in the R606 experiment at the ISR[75]. From the performance of the chambers at the PS as well as from the experience gained at the ISR, we expect for the chambers of the central detector the following properties:

TABLE 5.2. Measured drift angle as a function of the electronic field E and magnetic field B.

B \ E	1kV/cm	1.5 kV/cm
0.5 T	26°	< 20°
1 T	45°	32°

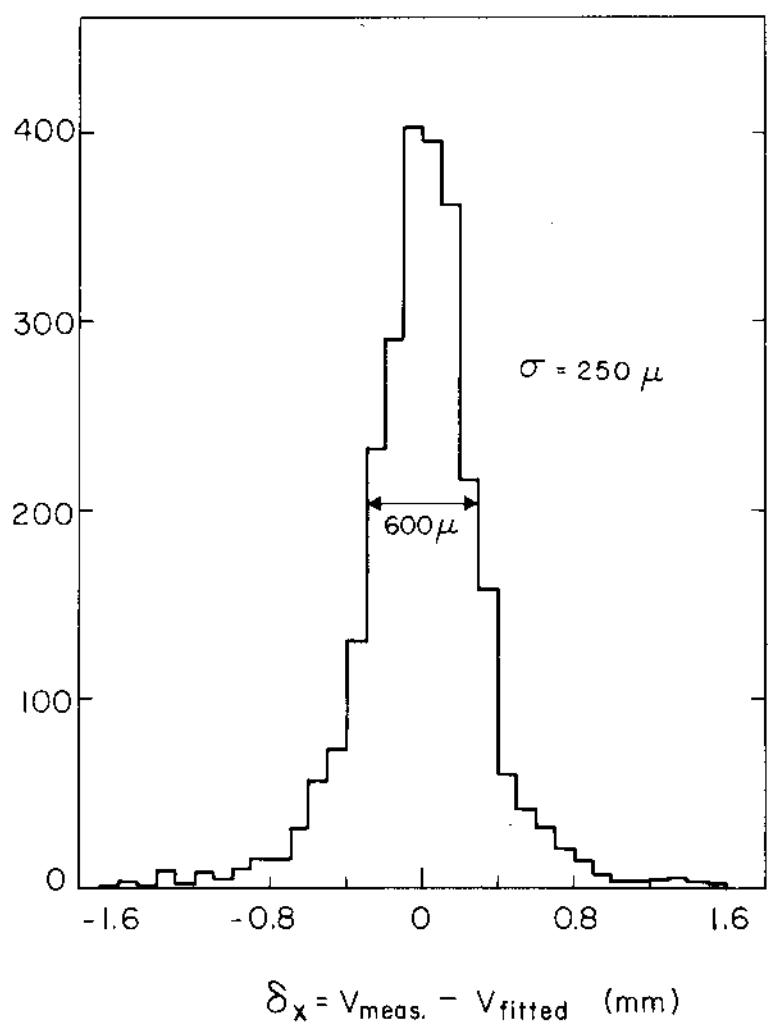

Figure 5.3 Distribution of residuals for a sample sense wire (see Reference 75).

1) high reliability with an efficiency of 99.8%
2) a spatial resolution in the drift direction of 2.50 μm, see Figure 5.3.
3) no angular dependence of the drift velocity between 0^{o} and 90^{o}. Figure 5.4 shows the drift velocity up to 45^{o}. For tracks parallel to the drift field (90^{o}) the same drift velocities are observed.
4) a drift angle of the expected magnitude as shown in Table 5.2
5) the capability of recording many tracks with a two track resolution of 2.5 mm corresponding to 50ns drift time
6) figure 5.5 shows that a dE/dx resolution of 14% was obtained by retaining the 4 lowest pulse heights out of 10 x 2 cm samples. This implies for our increased track length in the central detector that a dE/dx resolution of 6% can be obtained.

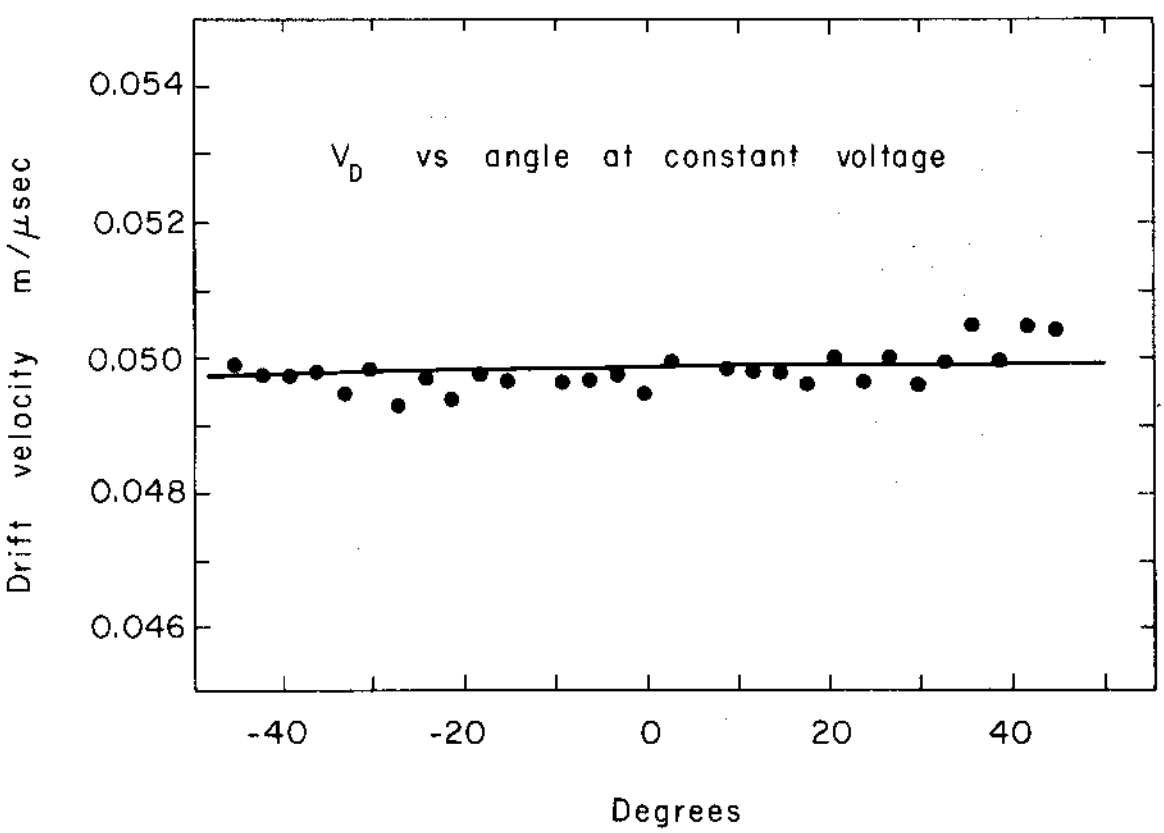

Figure 5.4. Electron drift velocity versus the angle the track makes with the electron drift direction.

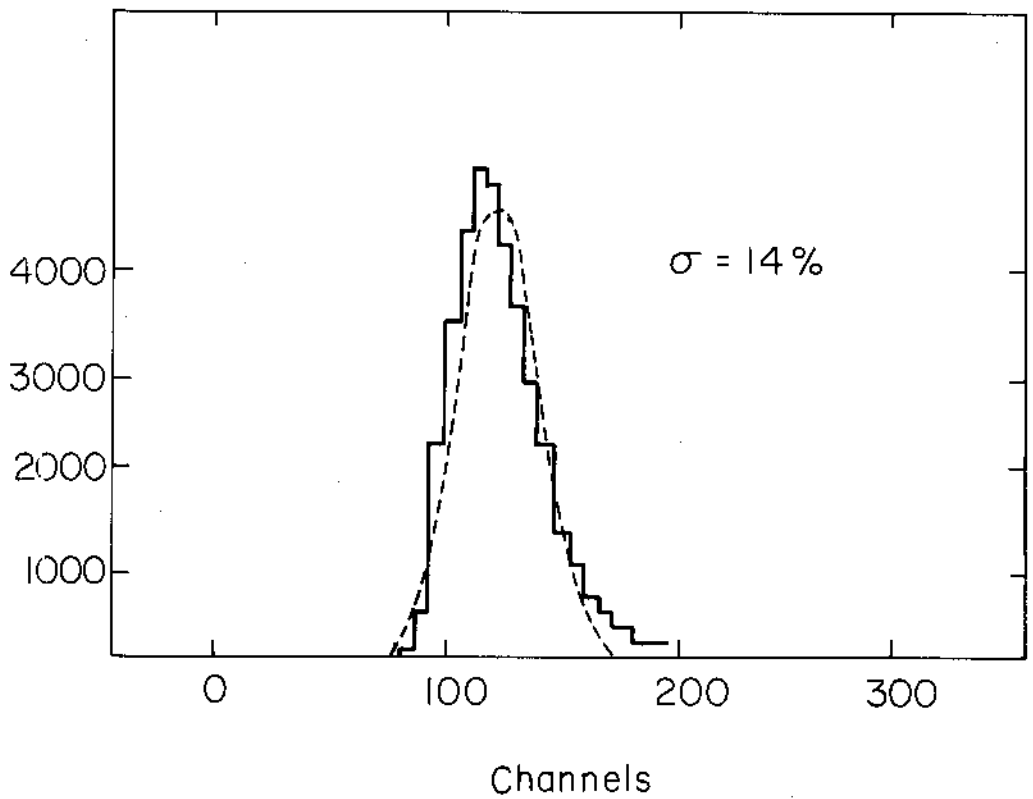

Figure 5.5. Pulse height spectra of the lowest pulses. The fitted gaussian gives a dE/dx resolution of 14%.

The relativistic increase of the ionisation is roughly 50% in the p/m range 3 - 150. A resolution of ± 6% would allow therefore a separation of pions, kaons,protons and electrons with the following confidence levels:

C.L.	> 95%	π - p	5 - 30 GeV/c
	> 85%	π - K	3 - 30 GeV/c
	> 70%	K - p	5 - 70 GeV/c
	> 95%	π - e	0.3 - 15 GeV/c

A detailed description and the results of the tests can be found elsewhere[72].

5.4.2. SPACE CHARGE EFFECT. Positive ions create an additional electric field perpendicular to a wire plane which increases linearly with the distance from this plane. This has no effect on the drift velocity which is in the saturated region but slightly modifies the angle of drift (α) ($\alpha \sim 22^{o}$). For our configuration we have computed a maximum distortion of 170 μ perpendicular to the wire plane for a flux of 2.5×10^{5} particles/m^2/second, which corresponds to the expected track density at full luminosity at 10 cm from the beam. Details of this calculation are presented in reference[76]. We have measured the deflection of electrons due to space charge effects in our test chambers and our results agree well with theoretical calculations. Distortions in successive planes tend to compensate and the effect on sagitta will be reduced. Our continuous calibration will allow such effects to be monitored and make further corrections if necessary.

5.4.3. EXPECTED PERFORMANCE OF CENTRAL DETECTOR. With the wire configuration described above we have calculated [77] $(\Delta p/p)$ and $\Delta\theta$ for reconstructed tracks with a random setting error of 250 μm for each point of the track. Figure 5.6 shows lines of equal $(\Delta p/p)$ as a function of the longitudinal momentum p_L and transverse momentum p_T. The best case is shown for a dip angle of $\lambda = 0^{o}$ where λ is defined as the angle the track makes to the plane perpendicular to the field direction. These errors have been calculated under the assumption that there are no systematic errors in the chamber geometry. If these systematic errors can only be controlled within 100 μm the errors shown in Figure 5.6 should be increased by a factor of two. Perpendicular to the wire direction the track angle is determined in the same calculation to an accuracy of approximately 2×10^{-4}. Along the wire direction an angle error of between 40 and 80 times worse is obtained. This arises because of the increased setting error of 1 to 2 cm along the wire, determined by the current division. With a precise value of the vertex position, obtained from many tracks, this angle error could be reduced by a factor of two. However this latter direction is closely related to the azimuthal direction about the beam which does not require such an accurate measurement.

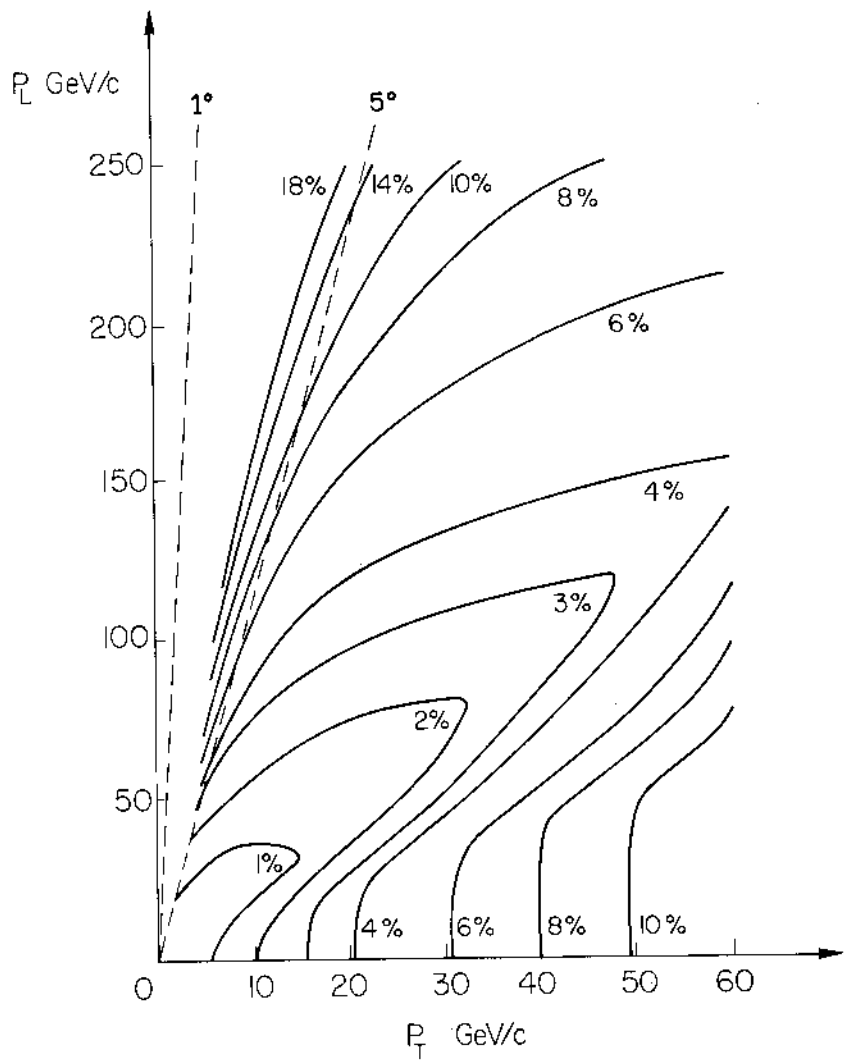

Figure 5.6. Lines of equal ($\Delta p/p$) as a function of longitudinal momentum p_L and transverse momentum p_T. No allowance has been made for systematic errors.

As noted above Fig. 5.6 is for a dip angle $\lambda = 0^{o}$. For other dip angles this error will increase by a factor $(\cos\lambda)^{-1}$. This does not take into account a possible increase of the setting error as λ increases. This question is currently under experimental investigation. Preliminary results suggest less than a 10% increase in the error out to track angles of 45^{o}.

5.5. CALIBRATION AND MONITORING. The chambers we are proposing to build are essentially analogue devices. In order to achieve the effective 60 μ r.m.s. error on the sagitta that we claim in section 5.4.3 we have to control very carefully all systematic errors down to that level. Moreover average pulse heights must bo monitored to 5%.

The mechanical design enables us to measure the position of individual sense wires to the required accuracy. In particular the support of the chambers should not apply any stress to their structure. Similarly electronics will include automatic calibration facilities.

The main effects to control then, are variations of drift velocity and drift angle due to mechanical or magnetic field imperfections, changes in temperature and gas composition, and space charge effects. We will deal with these problems in three ways:

a) we are planning a careful study of chamber behaviour on prototypes. We will chose final parameters which will maximize drift velocity stability and minimize the drift angle.

b) our system is, to a large extent, self calibrating.This comes from the fact that we are drifting in opposite directions on either side of a sense wire plane. A track will usually cross several drift spaces and the measurements will have to be consistent. Linking of track segments provides detailed information on the drift velocity and the drift angle, since variations of these quantities will have opposite effects in adjacent drift spaces. Moreover points close to the sense wire planes (small drift times) are not subject to variation of drift parameters and can be used to fix the position of tracks in space.

c) we plan to draw fiducial marks in our volume. We are investigating several possibilities. The most powerful one seems to be the use of a pulsed UV laser. In principle, it can extract, by multiple photon absorption, electrons on rigorously straight lines. Time zero could be known to few ns. The number of electrons per unit length is controled by the laser intensity. For pulse height calibration, we can use also Fe^{55} sources.

5.6. ADDITIONAL CHAMBERS

5.6.1. WINDOW AT 90°. Perpendicular to the beam pipe in the horizontal direction there is a measurement hole. This occurs because of two reasons:

1) tracks travelling parallel to the chamber wires gives large pulses but only a small number of wires detect these tracks
2) the magnetic field is in this direction and hence provides no bending.

The magnet is designed to have a hole about this axis ± 0.45 m vertically and ± 0.45 m along the beam direction. The vertical aperture is matched to the measurement limit of the central chamber and the horizontal aperture is increased to allow for the 0.30 m long interaction region of the beams. It is proposed to put two sets of drift chamber planes external to the magnet to measure the escaping tracks. These could be used as the first stage of a spectrometer arm which could be added at a later date.

5.6.2. HOLE IN FORWARD DIRECTION. Due to lateral dimensions of the beam pipe (ϕ = .15 m) tracks produced between 2° and 5° to the beam axis only have part of their trajectory in the active part of the central detector leading to reduced accuracy. Below 2° a particle leaves the central detector completely undetected. To improve the measurement accuracy of such tracks we propose to have two sets of drift chambers, 1 metre apart, situated at 5.5 m and 6.5 m from the intersection region. These chambers are described in chapter 9.

TABLE 5.1. CHAMBERS

Type	Drift, image read-out	
Gas	Ar/Ethane	
Drift length	20	cm
Drift field	1.5	kV/cm
Drift velocity	0.05	m/μs
Drift angle	22^{o} at 0.7	T
Collecting electrodes		
(a) Configuration	Quadrupole	
(b) Wire spacing	3	mm
(c) Wire length	Max. 2.5	m
(d) Support wires	None	
(e) Wire diameter, sense	40	μ
(f) Wire diameter field shaping	100	μ
Planes normal to vacuum chamber		
(a) Total number of half planes	10	
(b) Number of wires/plane	350	
Planes parallel to vacuum chamber		
(a) Total number of half planes	12	
(b) Number wires/plane	600	
Total number of sense wires	10,700	
Ionisation measurement	± 6%	
Localisation along wires	Current division	
Accuracy of pulse division	1% of w. length	
Accuracy to time measurement	$\lesssim$ 250 μ	
Two track resolution	2.5 mm	

6. ELECTRON AND PHOTON DETECTOR

6.1. INTRODUCTION. The photon and electron detector encloses the track sensitive chamber over the largest possible fraction of the solid angle. It is designed in order to achieve:

i) detection of photons and measurement of their energy by total absorption.

ii) measurement of the energy of high energy electrons, primarily from W^0 and $W^{\pm}$ decays with the best possible accuracy.

iii) electron identification in the presence of hadronic background which is expected to be several orders of magnitude more abundant.

Homogeneous shower detectors like lead glass or sodium iodide blocks which give very good energy resolution have been discarded because of:

i) their sensitivity to radiation damages

ii) the prohibitive cost of a 70 m^2 detector

iii) the requirements on the phototubes which must be located behind the crystal

iv) the difficulties in the longitudinal segmentation for π/e discrimination.

A lead liquid argon detector, as proposed for several detectors, has potentially a very good uniformity between cells, a precise localisation of the centroid of the shower and can be calibrated with a great accuracy[66,78]. However an appreciable fraction of the solid angle must be sacrified to cryostat walls and various supporting structures which must hold the $\sim$ 140 tons of the detector through cryogenic insulation. Besides that, the operation of such a detector in the SPS tunnel could be rather complex.

A lead-scintillator sandwich counter gives less good but adequate resolution and is simpler. We thus propose to use a lead scintillator electromagnetic detector as a trade-off between flexibility, simplicity of construction and operation, low cost and a slightly worse energy resolution.

The list of parameters of the detector, which will be discussed in details in the following sections, is given in Table 6.1.

6.2. DESCRIPTION OF THE DETECTOR

6.2.1. GENERALITIES. Recently a new type of lead scintillator sandwich shower counter has been described[65] which avoids many of the older problems and makes this technique competitive with a liquid argon lead sandwich. The important novel feature is the method of light collection. UV scintillation light is produced in inexpensive but high quality plastic scintillator slabs. The light crosses an air gap into a thin plastic sheet doped with a wave-length shifting, but not scintillating, organic compound. The test counter of reference[65] is illustrated Figure 6.1. The counter with 2 mm lead plates and 1/2'' plastic scintillator sheets, 13 r.ℓ. deep was tested with electrons in the energy range 0.5 - 2 GeV. The light collection is uniform over the detector. The energy resolution is well fitted by the expression:

$$\Delta E/E = 0.092/\sqrt{E}(\text{GeV})$$

This result is to be compared to the one obtained with liquid argon and 1.5 mm lead plates[79]:

$$\Delta E/E = 0.075/\sqrt{E}(\text{GeV})$$

and to Monte Carlo calculations[80] for 2 mm lead plates which predict:

$$\Delta E/E = 0.090/\sqrt{E}(\text{GeV})$$

Clearly the results are in excellent agreement with each other once a small correction for the different converter thickness is introduced. They are consistent with the fluctuations expected from the shower development.

6.2.2. DESIGN. The central part of the photon detector covers the region from $\theta = 90^{o}$ down to $\theta = 25^{o}$ where θ is the angle of the emitted particle to the beam crossing axis. It is segmented in several narrow and long rings in the plane normal to the beam (Figure 6.2). This configuration gives a very convenient way to trigger on transverse energy.

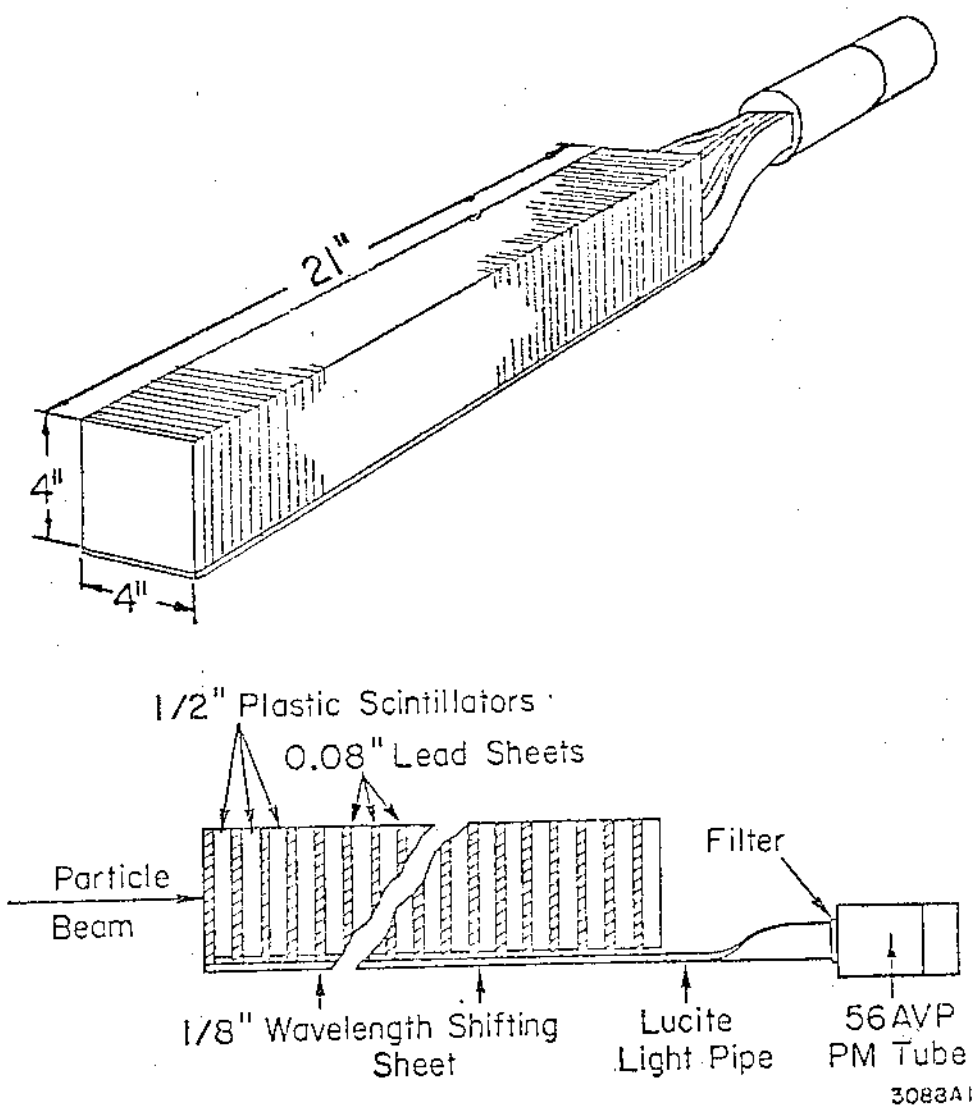

Figure 6.1. Lead scintillator sandwich counter used in Reference [65].

Each of the elements is split in two half moons consisting of a rigid honeycomb supporting structure and of the lead-scintillator stack mounted on its inside wall. The supporting structure extends above and below the half circles in order to ensure a rigid fixation of the elements on the magnet yoke (Figure 3.2). A special transfer frame is used to hold the half moon when not secured on the magnet. These precautions are necessary since the weight of each of these units is about 2 tons. Converter plates will consist of 2 mm lead and 2 mm scintillator sheets of precisely calibrated thickness. Natural lead is entirely satisfactory since it can adapt easily to the curved shape of the counter and it is held firmly in position inside the stack by the scintillator sheets. We have discarded the possibility of the more dense uranium converters[79] because its residual radioactivity will most certainly affect the operation of the chambers.

From $\theta = 25^{o}$ down to $\theta = 5^{o}$ the emitted particles will hit the end cap detectors. These detectors are also segmented in several units, each one covering a small fraction of production angles and about 180^{o} of the azimuthal angles. Supports and light pipes are following closely the design concepts already described for the large angle detectors (Figure 6.3). A strong backplate made of a rigid frame fitted with honeycomb material and solidly anchored to the magnet yoke holds the lead scintillator stacks. The weight of each of the detector units when completely equipped is approximately 12 tons and the supporting structure must be solidly designed. Light pipes come out horizontally between the two coils.

Since the whole photon and electron detector with exception of photomultipliers which are easily accessible on the outside of the magnet is made of inert material, it is expected that removal of units during the experiment in the SPS tunnel would be needed only in exceptional circumstances.

6.2.3.WIDTH OF COUNTERS. The width of each counter unit is primarily determined by the requirement of keeping as low as possible the possibilities of multiple hits. However a too fine segmentation

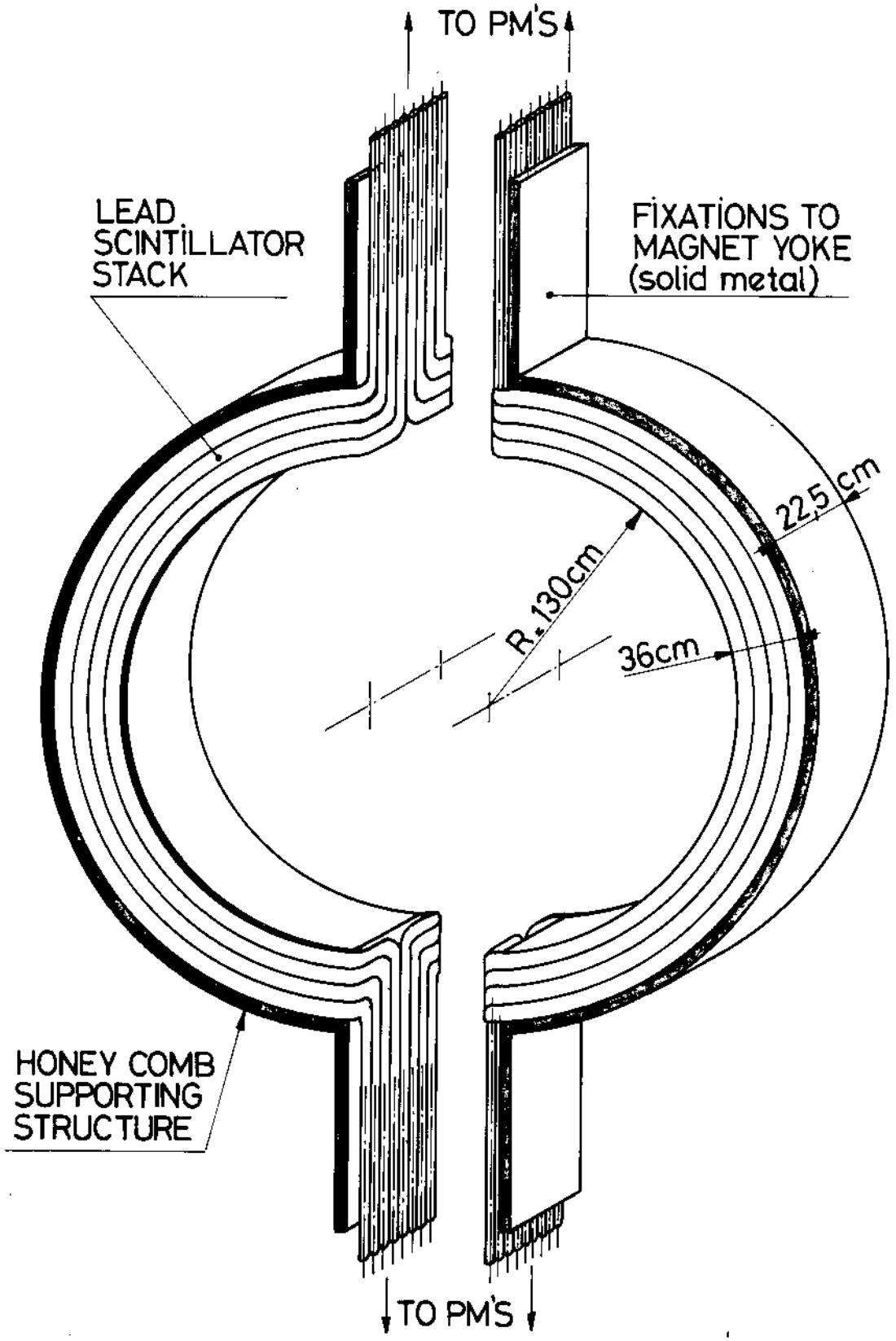

Figure 6.2. Schematic of the large angle unit photon detector.

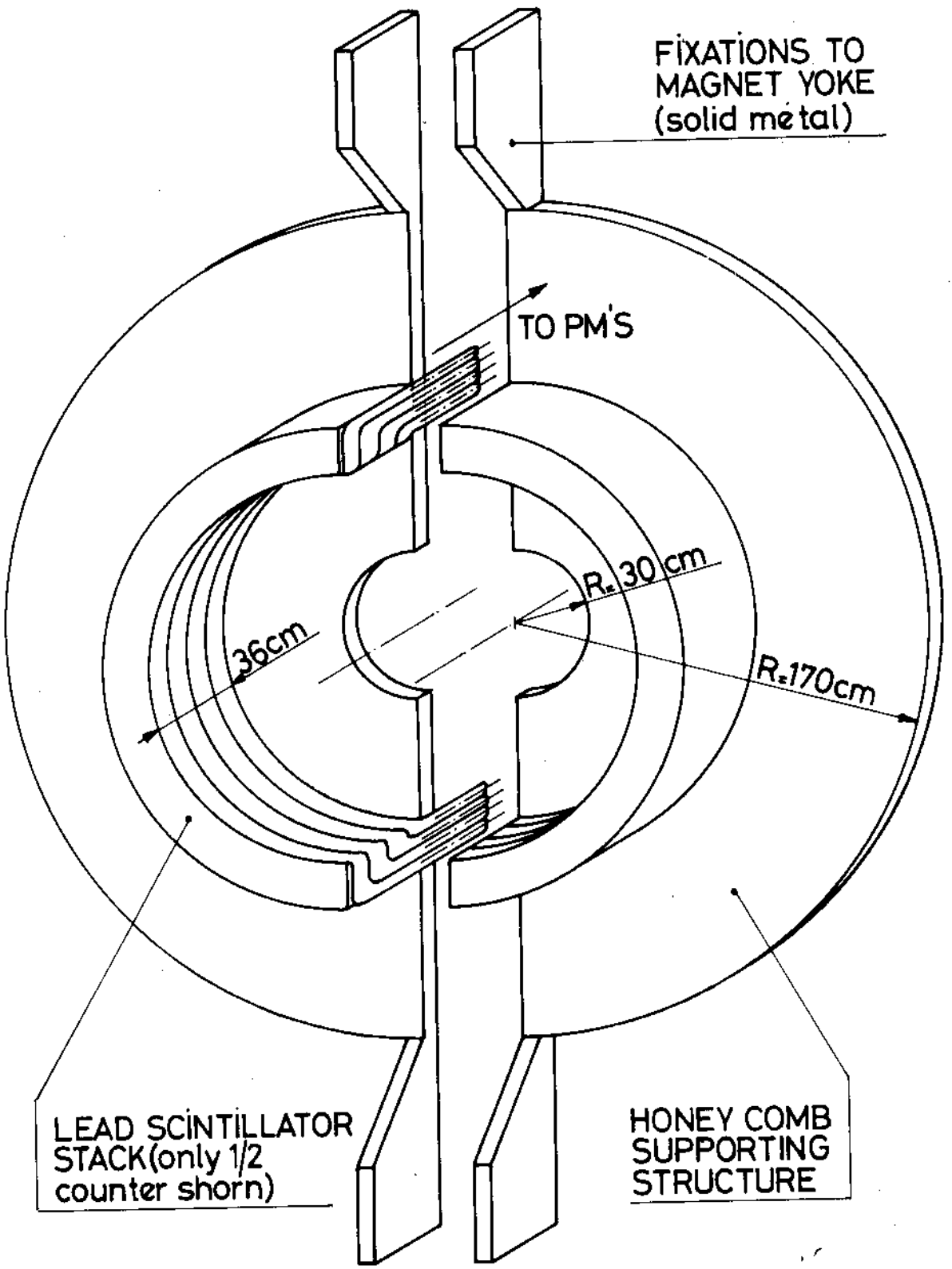

Figure 6.3. Schematic of the end cap photon detector.

increases the number of photomultipliers and the number of inactive gaps ($\sim$ 1 cm)between counters. An optimized layout must therefore take into account the fact that particle density per unit solid angle grows rapidly with decreasing production angle 0. A constant width of counters gives about equal hit probability in each counter.

Assuming $\frac{dN}{dy} = 1.5$ for π^0 production at collider energies,(note that at ISR energies, $\frac{dN}{dy} = 1.0$), we get an average of 4.5 π^0 per event in the central part of the photon detector and 4.5 π^0 per event in the end cap detectors. Note that the average p_T of these π^0 is expected to be $\sim$ 300 MeV/c.

In the present design there are 52 counters in the central part of the detector with a width of 22.5 cm at 1.3 m of the interaction point. This leads to an average of 0.09 π^0 per event in a given counter. This width is also well matched with the C structure of the magnet (4 counters per C).

The end cap detectors will consist of 10 half rings covering the same rapidity interval. Each ring gets an average of 0.11 π^0 per event. At 5^o which is the smallest covered range, the ring counter has a radius of $\sim$ 30 cm at 3.5 m of the interaction point and is 5 cm wide.

6.2.4. DEPTH OF COUNTERS. The thickness of the stack is determined by the requirement of a good containment of the shower. An experimental[81] transition curve for 50 GeV electrons is shown in Figure 6.4. In Figures 6.5a, 6.5b, 6.5c we show the distribution of the energy depositions of a 50 GeV electron after 12.4 and 24.8 radiation lengths. We remark the presence of an asymmetric tail in the distribution due to few showers which penetrate much further than the average. We conclude that in order to ensure an appropriate and symmetric response to high energy electrons the depth of the counter must be at least 25 radiation lengths (along the direction of incidence of particles).

6.2.6. LEAD SCINTILLATOR STACK. The stack is made of 84 thin sheets of ordinary lead (2 mm), which correspond to 30 radiation length in the direction normal to the stack. The scintillator plates are made of commercial acrylic doped with appropriate scintillating agents and wave-length shifter (PLEXIPOP). In order to minimize the thickness

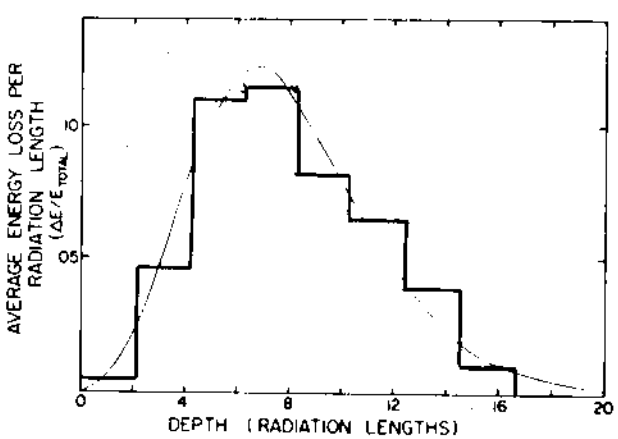

Figure 6.4. Distribution of energy in lead glass vs depth 40-45 GeV electrons. From Reference 81.

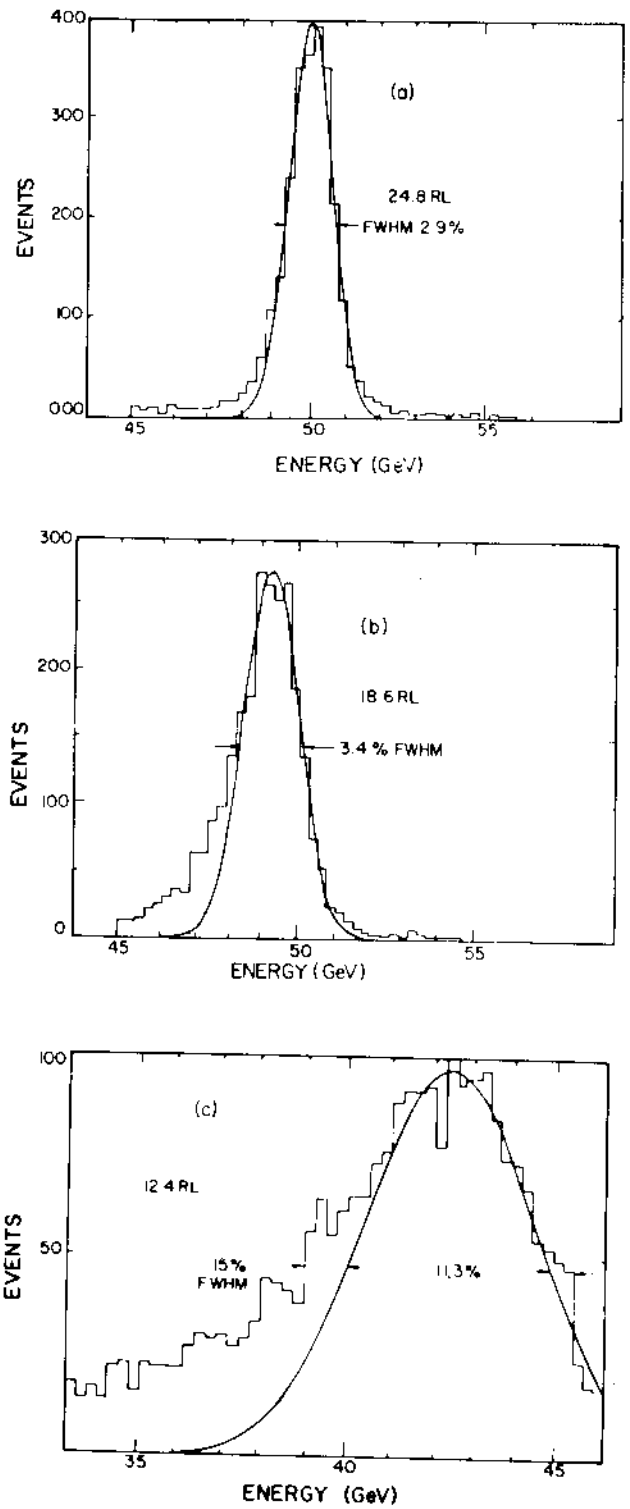

Figures 6.5. Fraction of energy deposited in lead glass after: a) 12.4 r.ℓ, b) 18.6 r.ℓ., c) 24.8 r.ℓ. From Reference 81.

of the overall lead scintillator stack, the PLEXIPOP sheets are 2 mm thick. The maximum thickness of the stack is then 360 mm.

6.2.7. LIGHT COLLECTION. The light collecting pipes are on the side of each counter. They consist, for the large angle units, of $\sim$ 4 m long, 4 mm thick pieces of acrylic, BBQ doped material. The light emerging from the edge of the scintillator crosses a $\sim$ 1 mm air gap and reaches the pipes. These pipes absorb the light at λ = 420 nm from the scintillator and reemits it at $\lambda \sim$ 480 nm. Since the reemitted light is isotropic, approximately 1/3 of this light is within the internal reflection angle and is transported with an attenuation length $\geq$ 3.5 m onto the two (up and down) small area (1'' - 2'' diameter) phototubes. Note that this attenuation length is well matched to the length of the counter.

6.3. EXPECTED PERFORMANCES.

6.3.1. ENERGY RESOLUTION. The counters have been designed in order to ensure the best performance around 50 GeV which is the typical electron energy from W^0 or $W^{\pm}$ decays and to retain a reasonable energy resolution (for photons) down to a fraction of a GeV. However since the geometrical parameters of electromagnetic showers vary very slowly (logarithmically) with energy the optimum performance is ensured over a very broad energy range.

The energy resolution of such a detector is determined by three components:

i) the sampling fluctuations.

From these fluctuations we expect an energy resolution for particles with an incidence normal to the stack:

$$\Delta E/E = 0.09/\sqrt{E(\text{GeV})} \qquad \text{see 6.2.1}$$

The response for particles at different angles of incidence has been extensively studied with a Monte Carlo program[80]. The program reproduces very well the experimentally observed shower fluctuations for a variety of lead plate thicknesses and energies whech are well represented by the empirical formula[82]:

$$\Delta E/E = 0.05 \left(\frac{dE}{dx} \cdot \Delta x \right)^{\frac{1}{2}} \frac{1}{\sqrt{E(GeV)}}$$

where $\frac{dE}{dx}$ is the energy loss (in MeV) in one layer (lead + scintillator sheet).

We have extended these calculations to the case in which the particle (electron or photon) is incident on the stack at an angle $\neq 90^{o}$. Results are shown in Figure 6.6 where it is apparent that the shower fluctuations could be made independent down to $\sim 25^{o}$ as long as the thickness of the converter plates is reduced by a factor $1/\sin\bar{\theta}$, where $\bar{\theta}$ is the average incidence angle for each half moon, in order to compensate the increased thickness due to the angle of incidence.

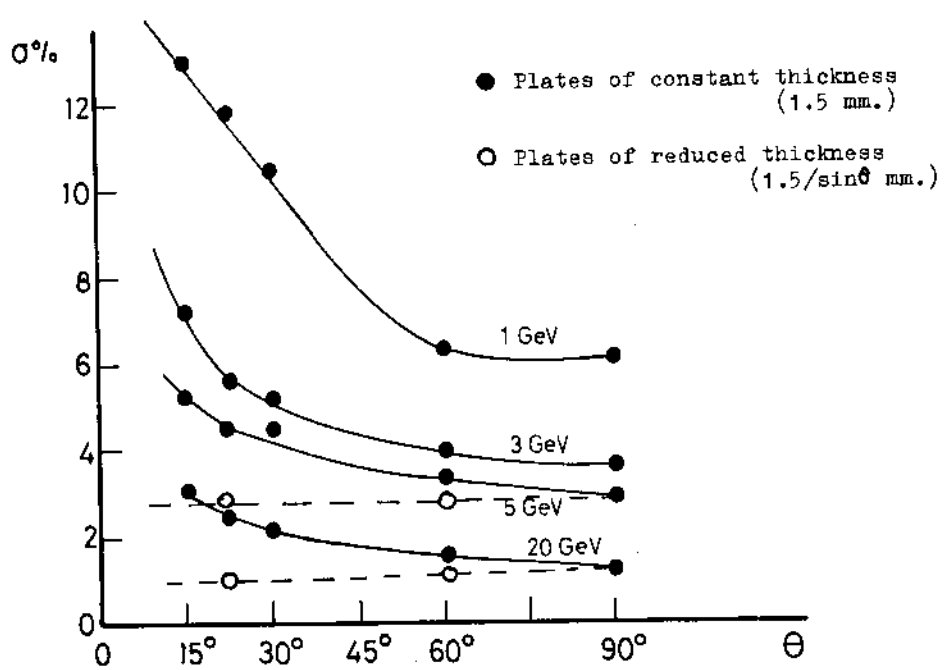

Figure 6.6. Energy resolution for showers generated by electrons with different impact angles. From Ref. 80.

Particles emitted at angles smaller than 25^{o} intercept the end cap detectors which have plates oriented in an almost normal incidence.

The inactive gaps between counters are $\sim$ 1 cm. We expect that this distance does not affect the precision of our measurements. Monte Carlo tests are in progress.

ii) Statistical fluctuations in the number of photoelectrons.

The figures have been derived following closely the work of Barish et al.[67] which gives results on light collection with the same type of counter.

We expect one photoelectron in each collecting bar per 5.7 MeV deposited in the stack. This leads to:

$$\frac{\Delta N(\text{photoelectron})}{N} = \frac{\Delta E}{E} = \frac{0.05}{\sqrt{E(\text{GeV})}}$$

We are aware however that other teams have obtained significantly less light than expected. We plan to study carefully this discrepancy with the test prototypes. However this does not appear to be crucial for high energy particles since we are there limited by systematics.

iii) Systematics for high energy particles.

Extrapolation to the energy interval of interest for the Z^{o} and $W^{\pm}$ search is not entirely trivial. Fluctuations of the shower development and of photoelectrons decrease as $1/\sqrt{E}$ giving for instance at E = 50 GeV a resolution $\sigma = 0.1 \times \frac{1}{\sqrt{50}} = 1.4 \times 10^{-2}$. Such an ultimate resolution can be substantially masked by calibration errors in the PM's and by inhomogeneities of the light collection. Some estimates of these effects can be obtained from data available for a lead glass counter[81] which exhibits up to 50 GeV an energy resolution well represented by a $1/\sqrt{E}$ term plus a constant which becomes significant only at high energies:

$$\Delta E/E = \frac{0.10}{\sqrt{E(\text{GeV})}} + 0.015$$

We estimate that realistic energy resolution at 50 GeV for the sandwich counter is 2 - 3%.

6.3.2. HADRON REJECTION. In addition to the measurement of the energy of an electromagnetic shower and provision of a trigger which indicates occurence of the shower, the counters must provide an effective identification of electron amidst a large flux of hadrons.

In our counter one radiation length corresponds to only 0.03 hadronic absorption lengths: hence an early development of a sizeable cascade is an effective way of recognizing an electromagnetic shower Another method consists of comparing the known momentum p of the incoming electron with the total visible energy E in the lead scintillator stack. For electrons $E/p \simeq 1$ whilst for hadrons $E/p << 1$.

This has been studied in detail in ref.[79] for a 50 GeV incident electron on a lead glass shower counter. The size of the task is indicated by Figure 6.7a. After applying threshold cuts, there is a suggestion of an electron peak in Figure 6.7b near 1.0 on the E/p plot. In order to further separate electrons from those hadrons which deposit all their energy in the array (most likely through π^0 production reactions) the authors use information on the longitudinal distribution of the electromagnetic shower given by four independent sections. The result of these cuts is the E/p distribution shown in Figure 6.7c. From this figure we can derive a formula for the hadron rejection = $5 \times 10^{-3} \times \Delta p/p$ where $\Delta p/p$ is the momentum resolution from the central detector.

Following this work, we thus propose to segment our counter in four independent sections: 0 - 6 r.ℓ., 6 - 12 r.ℓ., 12 - 24 r.ℓ, and 24 - 30 r.ℓ. A more refined optimization will be performed during the tests of prototypes. We expect a hadron rejection of the order of $\sim 7 \times 10^{-4}$ for 50 GeV charged particles at 90° ($a = 7 \times 10^{-3} \times \frac{\Delta p}{p}$ with our sampling). This could be even improved by using the information from the hadron calorimeter.

At the triggering level we expect to have a rejection factor of at least 20 to 50 by comparing the ratio of the energy deposited in the

first half of the calorimeter stack to that deposited in the second half. A rejection factor of this type has been reported[83] in a recent study of a thin lead argon calorimeter exposed to 15 and 50 GeV electrons. In addition we plan to have a layer of scintillator in front of the counters to distinguish electrons from π^0 at the trigger level.

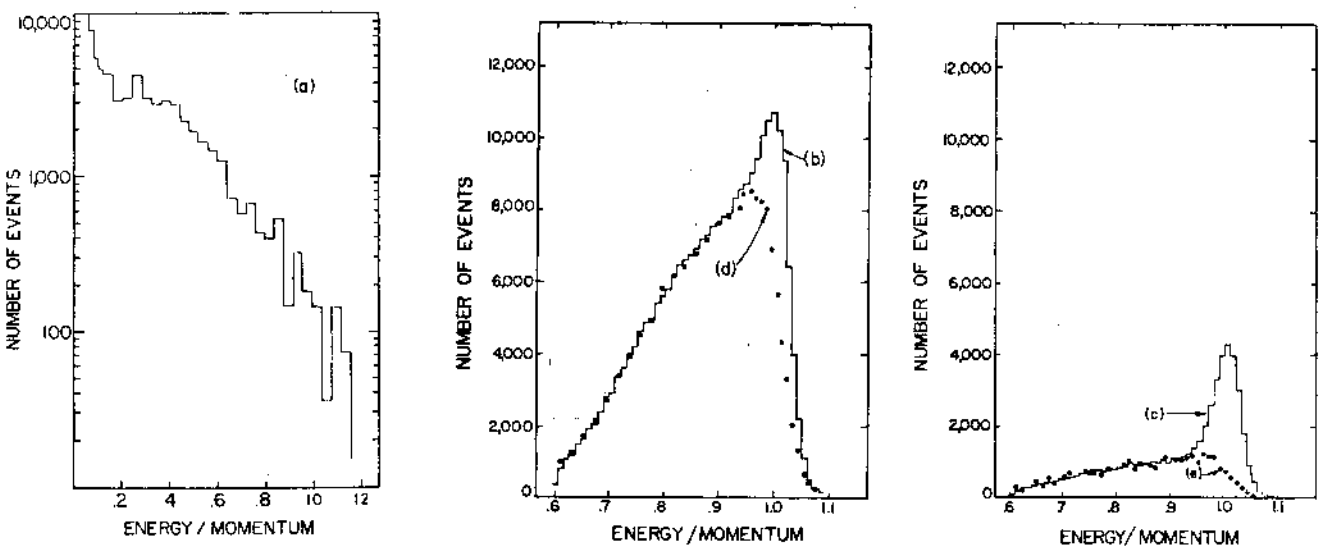

Figure 6.7. Fraction of energy (E/p) deposited in lead glass for a) all incident charged 40-45 GeV particles, b) all particles above a threshold requirement, c) all particles passing shower shape requirement, d) all hadrons passing the cuts of b), e) all hadrons passing the cuts of c). From Reference 81.

6.3.3. LOCALIZATION OF THE SHOWER. The localization of an electromagnetic shower is performed in our counter through pulse height division.

Azimuthally (with an attenuation length of 3.5 m in the wave shifter bar) we expect a localization:

$$\Delta x = 15.9 \text{ cm}/\sqrt{E}(\text{GeV})$$

in our central counters.

TABLE 6.1. Electron and photon detector.

Type	Lead scintillator stack
Depth, normal to incidence	30 r.ℓ.
Lead plate thickness, normal to incidence	2 mm
Scintillator plate	
(1) Material	UV acrylic, PLEXIPOP
(2) Thickness	2 mm
(3) Light attenuation length	$\sim$ 20 cm
(4) Total surface	$\sim$ 5900 m^2
Total number of converter sheets, scintillator plates	84
Thickness stack, max.	360 mm
Large angle units	
(1) Shape	half moon, 1.3 m radius
(2) Width	22.5 cm
(3) Approximate weight	1.8 Tons
(4) Total number required	52
End cap detector	
(1) Shape	half moon
(2) Radius	variable 30 cm to 1.3 m
(3) Number/end cap	10 x 2
(4) Approximate weight of each end cap	10 Tons
(5) Subdivision	iso-rapidity gaps
(6) Width	max. 30 cm min. 5 cm
Light collecting pipes	
(i) Material	acrylic, BBQ doped
(ii) Length, large angle units, max.	4.10 m
(iii) Thickness	4 mm
(iv) Attenuation length	$\geq$ 3.5 m

TABLE 6.1. continued

Resolution	
(i) At low energies	$0.1/\sqrt{E}$(GeV)
(ii) Ultimate, at high energies	0.02 - 0.03
Localization, by pulse division	
(i) Longitudinal	$\pm$ 16 cm/$\sqrt{E}$(GeV)
(ii) Transverse	$\pm$ 1 cm/$\sqrt{E}$(GeV)
Electron-pion discrimination	
(at 50 GeV)	$\leq 7 \times 10^{-4}$
Segmentation along shower	4
Phototubes	
(1) Large angle units	832
(2) End caps	320
Light yield	~350 photoelectr./GeV

In the transverse direction for a scintillator with a purposely short attenuation length of $\sim$ 20 cm, we expect by collecting the light on bothe sides of the central counters:

$$\Delta y = 1 \text{ cm}/\sqrt{E}(\text{GeV})$$

These figures have been derived following closely the work of Barish et al.[67].

This very precise localization of the centroid of all electromagnetic showers occuring in a given counter will allow us, if achieved, to detect extra π^0 whenever an electron hits a counter, through an off-set of the overall centroid with respect to the impact of the charged particle deduced from the track seen in the central chambers.

7. HADRON CALORIMETER

INTRODUCTION

We propose to build a hadron calorimeter which will measure the energy of particles produced with scattering angle, θ ($5^{o} < \theta < 175^{o}$). The physics requirements of the calorimeter have been discussed in section 2. Its main uses are in $W^{\pm}$ detection and in triggering on high p_T jets.

The calorimeter will measure the total hadronic energy contained in charged particles, neutrons and K^{o}s. It will thus complement the momentum measurement of the charged hadrons in the central detector. Although the two devices will have roughly the same energy resolution ($\frac{\Delta E}{E} \sim 15\%$), the hadron calorimeter can be used to trigger (either on-line or off-line in the software) on tranverse energy, E_T.

Ideally, we want a calorimeter which is symmetric about the azimuthal angle, ϕ, and in modular form so that we obtain E_T by summing over all elements:

$$\text{ie } E_T = \sum_i K_i (E_{em})_i \sin\theta_i + \sum_j h_j (E_h)_j \sin\theta_j$$

where $(E_{em})_i$ and $(E_h)_j$ are the energies deposited in modules i, j of the electron and hadron calorimeters.

Some modularity in θ is essential to convert from $E_{deposited}$ to E_T. By triggering on integrated E_T, we obtain an unbiased hadron or jet distribution. Off-line, a better determination of E_T is obtained by combining the measurements of track angle in the Central Detector chambers with the measurement of the total energy in the calorimeters.

Apart from its principal use in triggering, the hadron calorimeter is essential for detecting missing transverse energy.

eg $W \rightarrow \mu\nu$ where the high energy muon is detected.

The apparent momentum imbalance produced by the undetected neutrino is a possible W signature. This is discussed further in section 13.

7.2. CONSTRUCTION OF THE CALORIMETER. The hadron calorimeter will be constructed in two distinct parts.

A. Central Part

For large scattering angles ($30^{o} < \theta < 150^{o}$), the calorimeter is constructed by instrumenting the iron magnetic field return yoke with scintillator plates. As described in section 4, the yoke is constructed of identical 'C' shaped modules (Fig. 7.1). As the modules are the same length along the beam direction (90 cm), each subtends approximately the same interval of rapidity.

As shown in Fig. 7.2, the first layer of scintillator is immediately after the coil. These 'C's are, in fact, iron/scintillator sandwiches (5 cm iron and 0.7 cm of scintillator). The last layer of iron is a continuous slab, 10 cm thick, to make the module rigid and to decrease its magnetic reluctance. The iron thickness is 80 cm giving a total thickness including gaps for the scintillators of 96 cm (Fig. 7.2).

Each 'C' is subdivided into ten calorimeter elements subtending approximately equal azimuthal angles ($\Delta\phi \sim 18^{o}$). This subdivision matches the requirements of the 'C' construction, as discussed in Chapter 4. The resulting size of each calorimeter element is 90 x 80 x 96 cm^{3}.

B. End-caps

For smaller angles ($5^{o} < \theta < 30^{o}$ and $150^{o} < \theta < 175^{o}$), the calorimeter lies outside the magnet (Fig. 7.3). It will be constructed of iron plates, 5 cm thick and interleaved with 0.7 cm scintillator plates. The iron plates could be magnetized to aid muon identification, as discussed in section 8. The total thickness, including the scintillator is 150 cm (ie twenty five plates of 5 cm of iron).

The end-cap calorimeters will be built in a mosaic pattern to localize the showers in θ and ϕ. They will cover the same rapidity range as the Central Part of the calorimeter and will be subdivided into elements subtending solid angles defined by $\Delta\theta = 5^{o}$ and $\Delta\phi = 10^{o}$ (Fig. 7.3). (The opening angle of a jet is approximately $\pm 3^{o}$ [85]).

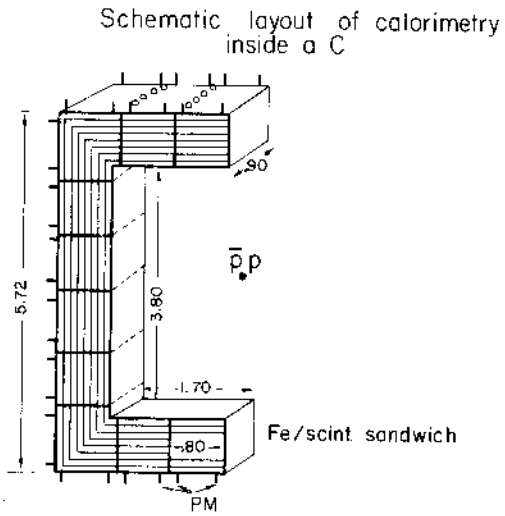

Figure 7.1. Subdivision of 'C' modules into calorimeter elements.

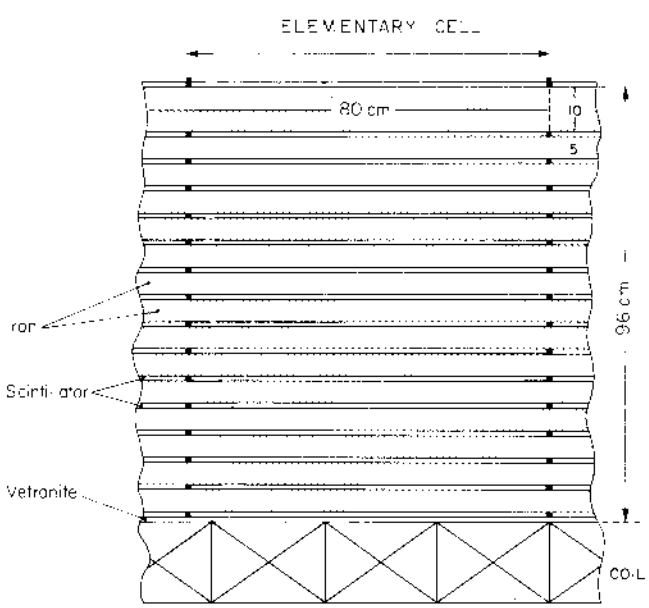

Figure 7.2. Basic iron scintillator sandwich of 'C' piece calorimeter.

With such a construction of the Central Part and End-caps, the calorimeter is essentially ϕ symmetric and has a good definition of scattering angle θ so that transverse energies can be calculated and used in triggering.

7.3. LIGHT COLLECTION. The space available for light collection between the 'C' modules and between the elements of the End-Cap is minimal. For this reason and in order to use as few photomultiplier tubes as possible, light will be collected by means of wave-length shifting bars and rods.

In the Central Part, a spacing of several centimetres between the 'C' pieces does not affect the magnetic field appreciably and can be used for light collection. Light from each scintillator plate will be collected via a wave-length shifting bar (plexiglas doped with BBQ) as used by Barish et al.[67]. This method allows great flexibility in sampling the shower as individual bars can be grouped together on to photomultipliers tubes as required. To ensure good uniformity of response, light will be collected from opposite sides of the scintillators, providing automatically a measurement in θ of the shower centroid. Also, as shown in Fig. 7.4, the showers will be sampled over two depths to give some discrimination of showers at small angles to the calorimeter plates. Sampling over two depths will also give a rough measurement of the shower development and will help in the muon identification. Therefore, four photomultiplier tubes will be used in each element of the calorimeter.

We estimate that a minimum ionising particle will produce approximately ten photoelectrons per scintillator, giving a reasonable signature for unaccompanied muons.

For the End-Caps, a different method of light extraction will be used to avoid having gaps between the calorimeter elements. Light will be collected via wave-length shifting rods in the manner developed by the MPI (Munich) group[86]. The rods are perpendicular to the plates and are inserted through holes drilled in the iron and scintillator slabs. Therefore, tracks from the interaction region are never parallel to the rods.

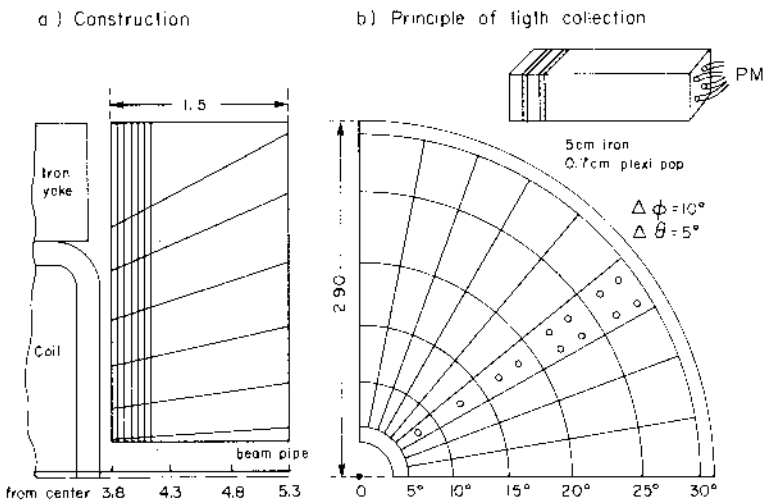

Figure 7.3. Subdivision of end-cap into calorimeter elements.

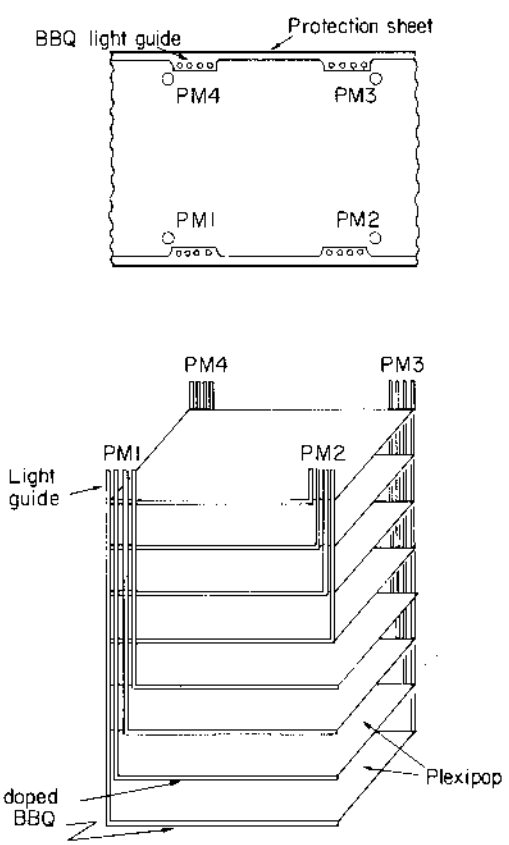

Figure 7.4. Method of light collection for 'C' piece calorimeters using wave-length shifting bars. A sheet of scintillator is read on two edges. The stack is divided in two parts, the bottom layers and the top layers, each one read separately.

7.4. ENERGY RESOLUTION. The energy r. solution of the calorimeter is determined by the frequency with which the shower development is measured and by the extent to which the interacting particles are contained in the calorimeter volume. Our sampling frequency is similar to that of Holder et al. [84] who used a 5 cm iron/0.6 cm scintillator sandwich. (The aluminium coil of the dipole has an absorption thickness corresponding to 6 cm of iron and so is equivalent to an extra calorimeter plate). The electromagnetic calorimeter gives excellent sampling over the equivalent of 15 cm of iron. In Table 7.1, we estimate our energy resolution from that of Holder et al. and by taking into account the following properties of our apparatus:

(i) the increasing plate thickness (with $\frac{1}{\sin\theta}$) for hadrons incident at small angles

(ii) some showers are not fully contained longitudinally. For the Central Part, the total effective thickness of iron is 116 cm, including the electromagnetic calorimeter, the coil and the scintillator. In the End-Caps, where the hadron energy is higher, the equivalent thickness of iron is 160 cm.

(iii) dead spaces due to the gaps between 'C' modules and to the wave-length shifting rods cover about 5% of the solid angle ($5^{\circ} < \theta < 175^{\circ}$).

We estimate that 90% of the incident hadrons will have more than 90% of their shower energy contained in the calorimeter. With decreasing scattering angle, θ, the resolution in the Central Part worsens due to the increasing effective plate thickness. This is partly balanced by the better containment of the shower at small angles to give a net resolution approximately constant with energy. At shower energies above 30 GeV, the energy resolution (σ(r.m.s.)/mean) is about 20%.

7.5. CONCLUSIONS. The parameters of the calorimeter are summarized in Table 7.2. We conclude that, by constructing the 'C' modules of the magnet return yoke as an iron/scintillator sandwich and by adding instrumented End-Caps to the dipole, we can build a hadron calorimeter with an almost complete solid angle coverage for $5^{\circ} < \theta < 175^{\circ}$. The use of wave-length shifters for light collection results in a manageable number of photomultiplier tubes.

The azimuthal symmetry of the calorimeter and its subdivision in θ will allow an unbiased trigger on energy transfer. Furthermore, an unaccompanied muon can be identified by its deposition of minimum ionization in the two sampling depths of the calorimeter.

TABLE 7.1. Estimation of energy resolution $(\frac{\sigma(\text{r.m.s.})}{\text{mean}})$

$\theta = 90^\circ$			$\theta = 45^\circ$		$\theta = 30^\circ$		$\theta = 15^\circ$	
E_h	E_T	$\frac{\Delta E}{E}$ (%)	E_T	$\frac{\Delta E}{E}$ (%)	E_T	$\frac{\Delta E}{E}$ (%)	E_T	$\frac{\Delta E}{E}$ (%)
15	15	26	11	31	7.5	36	4	25
30	30	21	21	22	15	25	8	21
50	50	16	35.5	17	25	20	13	16
75	75	13	53	13	35.5	15	19.5	13

where E_h = incident hadron energy (GeV)

and E_T = incident hadron transverse energy (GeV)

The estimation is based on the energy resolution of Holder et al.[84] $\left|\frac{\Delta E}{E} = \frac{1.9}{\sqrt{E(\text{GeV})}} \quad (\frac{\text{FWHM}}{\text{mean}})\right|$ and Sciulli's presentation of $\frac{\Delta E}{E}$ as a function of shower containment[87].

TABLE 7.2. Calorimeter Parameters

I. CENTRAL PART ($30^{\circ} < \theta < 150^{\circ}$)

Total No. of 'C' modules	16
Weight of 'C' module	52 tons
No. of calorimeter elements for 'C'	10
Subdivision of 'C' in φ	10 parts
Subdivision of 'C' in θ	none
Size of each calorimeter element	88 x 80 x 96 cm^3
Depth of iron in calorimeter	80 cm
Shower sampling	5 cm iron/7 cm scintillator
Surface of scintillator overall	2000 m^2
No. of PM tubes overall	640

II. END-CAPS ($5^{\circ} < \theta < 30^{\circ}$ and $150^{\circ} < \theta < 175^{\circ}$)

Inner radius of end-cap	0.35 m
Outer radius of end-cap	3.0 m
Weight of end-cap	135 tons
No. of calorimeter elements per end-cap	180
Subdivision of end-cap in	36 parts ($\Delta\varphi = 10^{\circ}$)
Subdivision of end-cap in θ	5 parts ($\Delta\theta = 5^{\circ}$)
Depth of iron in calorimeter	125 cm
Shower sampling	5 cm iron/0.7 cm scintillator
Scintillator surface (2 End-Caps)	1000 m^2
No. of PM tubes (2 End-Caps)	360

8. DETECTION OF THE MUONS

INTRODUCTION. The physics aims are outlined in Chapter 2. The two main reasons for identifying muons and measuring their momenta are:

(i) to detect W^o and $W^{\pm}$ through their decays to $\mu^+\mu^-$ and $\mu^+\nu$ respectively

(ii) to complement the electron identification over as large a solid angle as possible. Given the exploratory nature of our experiment, and the anomalies indicated by cosmic rays, it is important to be able to measure the lepton content in two different channels and by two essentially separate pieces of apparatus.

In this chapter we discuss the problem of identifying and measuring single muons from $W^{\pm}$ decay (detection of the W^o is easier as two muons must be identified making backgrounds much less important).

8.1. IDENTIFICATION OF THE MUONS. Muons will be identified through their non-hadronic nature. This fixes a minimum momentum of the identified muons, and we assume

$$p_\mu \geq 3 \text{ GeV/c}$$

(an high energy muon has 1.2 GeV/m ionisation loss in Iron). The two elements of a muon signature are:

- a track traversing all the material of our apparatus (electromagnetic calorimeter, coil, iron yoke, end-caps etc) without interacting.
- a collinearity (taking multiple scattering and measurement errors into account) between the track position and momentum as measured in the Central Detector and the position and direction of the track emerging from the hadron calorimeter. The trajectory of a typical muon is shown in Figure 8.1.

Possible ambiguities in muon identification are:

a) a primary hadron which traverses both calorimeters without interacting;

b) a secondary hadron from the hadronic shower emerges from the iron

c) the observed muon is from pion or kaon decay.

We discuss these three sources of background below.

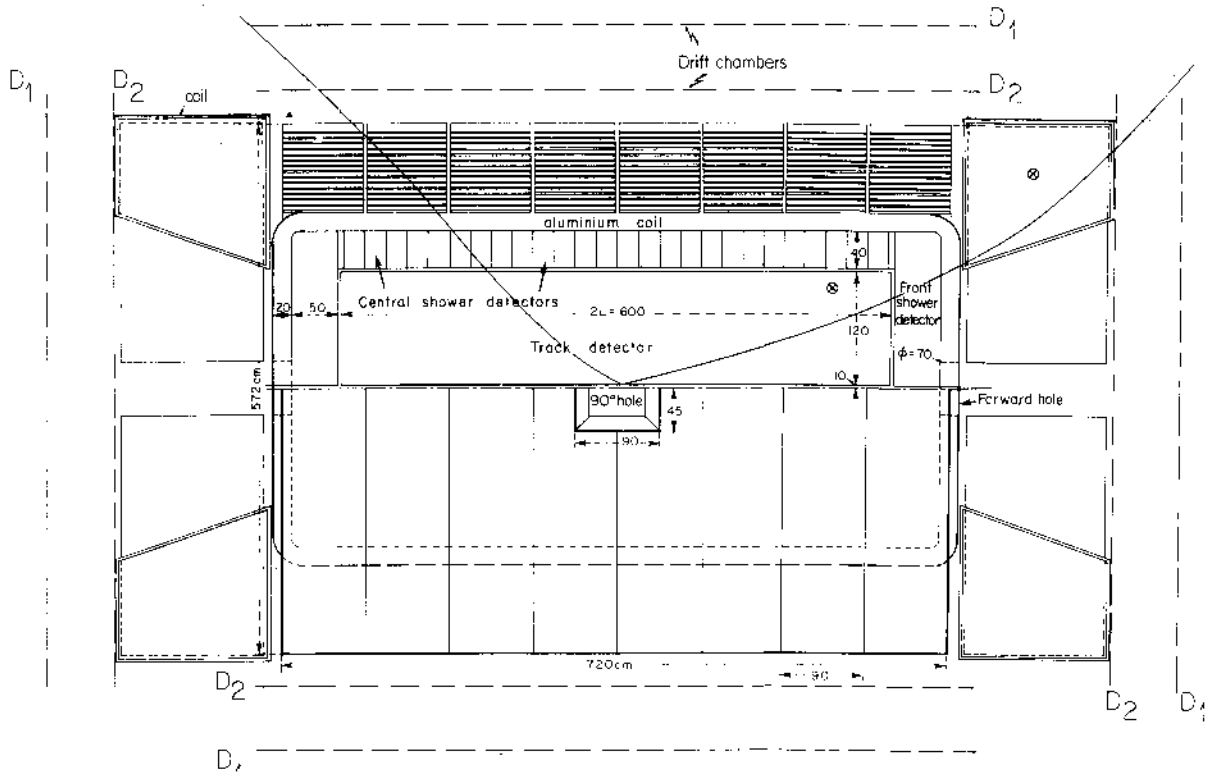

Figure 8.1 A side view of dipole and end-caps with the drift chamber in position, D_1, D_2. Two muon tracks are identified.

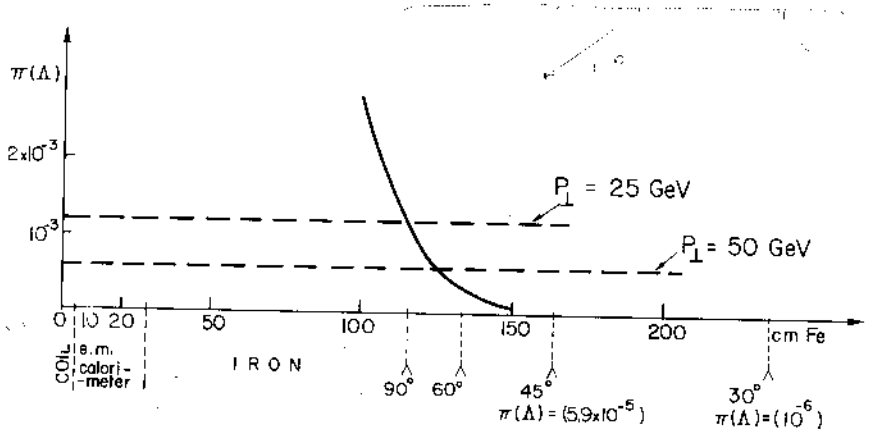

Figure 8.2. Rejection $\pi(\Lambda)$ of non-interacting pions. ($\pi(\Lambda)$ is the probability that a π traverses a thickness Λ of iron without nuclear interactions). In abscissa:thickness Λ of equivalent iron in cm, Λ_{90^o} being the thickness in cm of equivalent iron at $\theta = 90^o$ (e.m. calorimeter + scintillators + iron). For comparison the dotted lines represent the deacy probability of pions at fixed p_T.

a) Let us assume 17 cm of iron for the absorption length λ_{Fe} of a hadron of very high momentum. The probability $\pi(\Lambda)$ of a hadron going through our material without interacting

$$\pi(\Lambda) = e^{-\Lambda/\lambda_{Fe}} \quad ; \quad \Lambda = \Lambda(\theta) = \Lambda_{90^o}/\sin\theta \text{ cm of iron,}$$

Λ_{90^o} being the thickness indicated in Figure 8.2. As we see these rejection factors $\pi(\Lambda)$ stay between 10^{-3} and $< 10^{-4}$. A rejection factor $\pi(\Lambda)$ is therefore not enough to measure the $R = \pi/\mu$ ratio at $\theta > 45^o$, if R stays close to the values measured at lower energies $\sim 10^{+4}$. This means that a further study of this ratio could require in the future the addition of more material (e.g. 1 m iron) in a chosen angular region.

b) As shown in Figure 8.3, on average one particle remains after the shower produced by a 30 GeV hadron has propagated through one metre of iron[88,89]. This punchthrough contamination can be reduced by demanding a pulse height corresponding to minimum ionization in each calorimeter and also by requiring the trajectory of the secondary hadron to match the extrapolation of the track measured in the Central Detector. The former requirement is of no help when the muon is concealed within the development of a jet or accompanied by a hadron at small angles to it[78].

We define therefore a rejection function, Q,

$$Q(\Lambda,p) = N(\Lambda,p)F(p)$$

as a product of $N(\Lambda,p)$, the number of emerging secondary hadrons from a shower initiated by a hadron of momentum p, and the probability F that a hadron emerging after the hadronic cascade from the iron goes just through the $\Delta S_\mu \Delta\Omega_\mu$ region where one could expect a muon of the same momentum, which only undergoes Coulomb scattering. The situation is sketched in Figure 8.4. The rejection probability F is given by:

$$F = \frac{\Delta S_\mu}{\Delta S_H} \frac{\Delta\Omega_\mu}{\Delta\Omega_H}$$

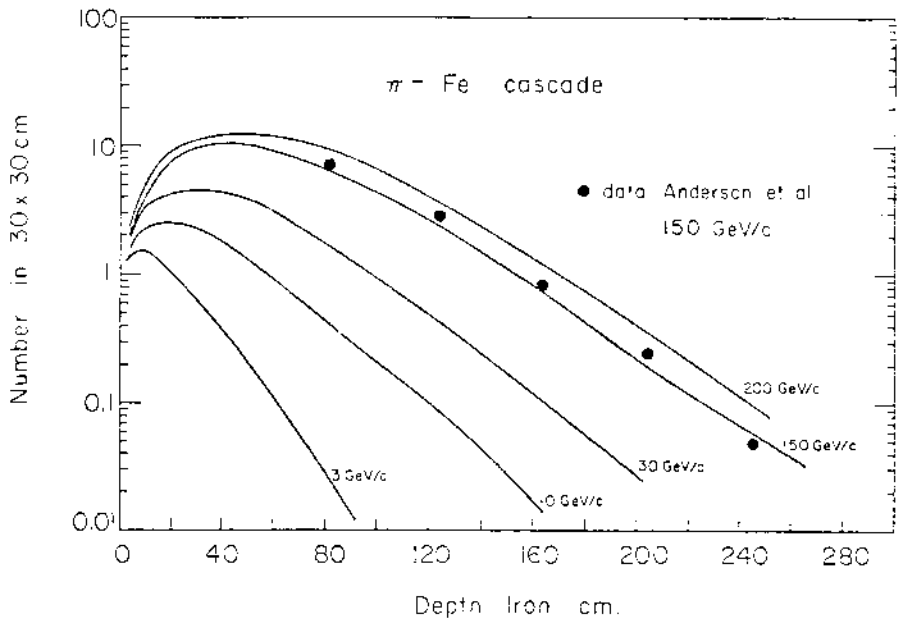

Figure 8.3 Number of hadrons (practically at any distance from initial axis) emerging from the iron thickness indicated in the abscissa (ref. 89, 90).

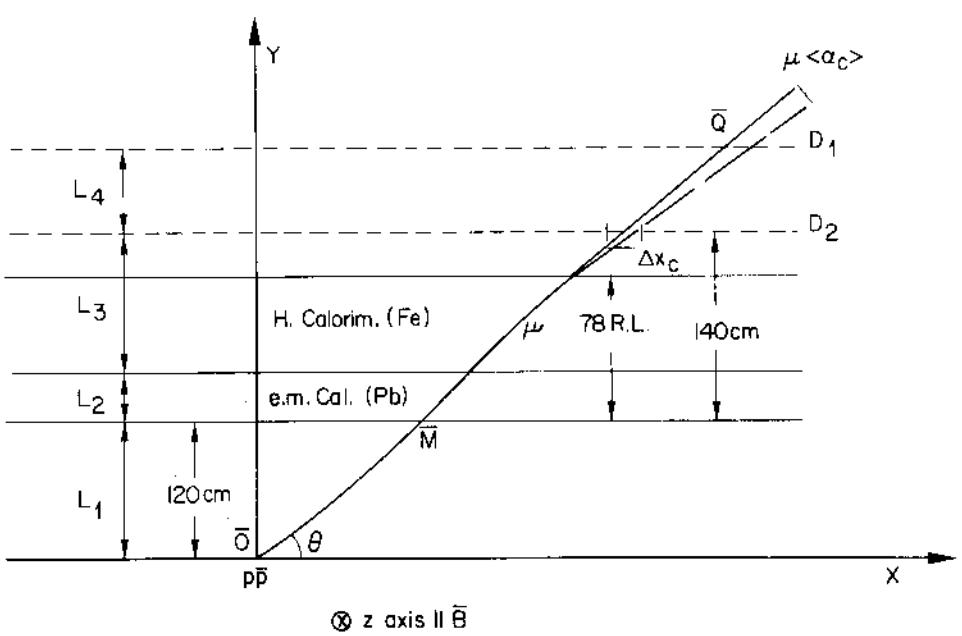

Figure 8.4 Schematic layout for study of the rejection function F(p). A muon traverses drift chambers D_1, D_2 with an indetermination Δx_c Δy_c due to errors reconstructing track $\overline{OM}$ and Coulomb displacement, and Coulomb scattering $\langle \alpha_c \rangle$. One pion emerging from a hadronic shower in iron has a much larger $\langle \alpha_H \rangle$ and Δx_H.

In this expression $\Delta\Omega_\mu \cong \Delta\Omega_c = \langle\alpha_c\rangle^2 =$

$$\left[\frac{1.4 \times 10^{-2}}{p(\text{GeV/c})} \sqrt{78/\sin\theta}\right]^2 = \frac{1.5 \times 10^{-2}}{p^2 \sin\theta} \quad (p \text{ in GeV/c}),$$

ΔS_μ is the area due to the central detector $\Delta x \Delta Z$ uncertainty and to Coulomb scattering. A detailed study of $\Delta\Omega_\mu$, ΔS_μ has been made. ΔS_H, $\Delta\Omega_H$ are the area uncertainty ($\Delta S_H \sim \pi \bar{r}^2$, $\bar{r}$ being the average distance between hadronic particles of the shower) and the angular dispersion (angle respect to primary direction) for an hadronic shower in iron[90]. The evaluation of F has given the encouraging results reported in Figure 8.5.

The Figure clearly shows that for $p_\mu \geq 10$ GeV the rejection factor $N(\Lambda)F$ allows a good separation between real muons and secondary hadrons.

In order to obtain this high rejection Q we must have external to the dipole a good localization of the muon track, with a $\Lambda\theta$, Λx resolution better than the Coulomb uncertainty. This will be discussed in Section 8.2.

c) The $\pi \to \mu + \nu$ decay probability is calculated to be P($\pi \to \mu,\nu$ decay in 1 m length) = .018/p(GeV); e.g. $P \cong 2 \times 10^{-3}$ for p = 10 GeV. This decay probability depends only on p_T as long as $\pi \to \mu\nu$ decays within the angular range $\theta \geq 30^\circ$ are considered (Figure 8.2). We did not consider explicitly the contribution from $K \to \mu\nu$ decay. Its contribution is as important as that of pion decay. In Figure 8.6, the decay probabilities in our apparatus are shown. The probability of $\pi \to \mu\nu$ decay (Figure 8.6) and the probability of the punching through of an intact hadron (Figure 8.2) are therefore our most important rejection functions for good muon identification. As expected the $\pi \to \mu\nu$ decay is more dangerous at the lower θ angles, just where the rejection against punchtrough is more effective (i.e. $\pi(\Lambda)$ is lower).

8.2. EXPERIMENTAL LAYOUT. As discussed above, the muon detector should allow a localization not worse than the Coulomb uncertainty of the most energetic muons coming out from the iron. Considering that this uncertainty for the μ's of 100 GeV is $\sim$ 1 mm and 10^{-3} radian, we have

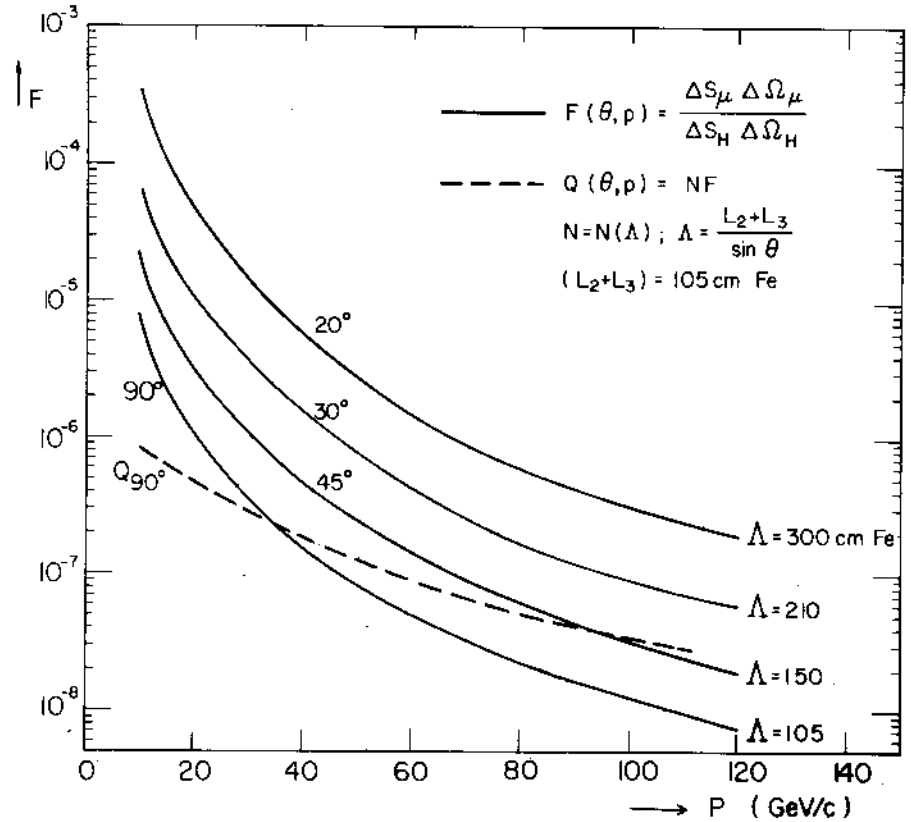

Figure 8.5 Function $F = (\Delta S_c/\Delta S_H)(\Delta\Omega_c/\Delta\Omega_H)$ probability of having a hadron within the "Coulomb telescope" of a muon. $Q = NF(p)$, total probability as above for N hadrons emerging from the iron in a very high energy event.

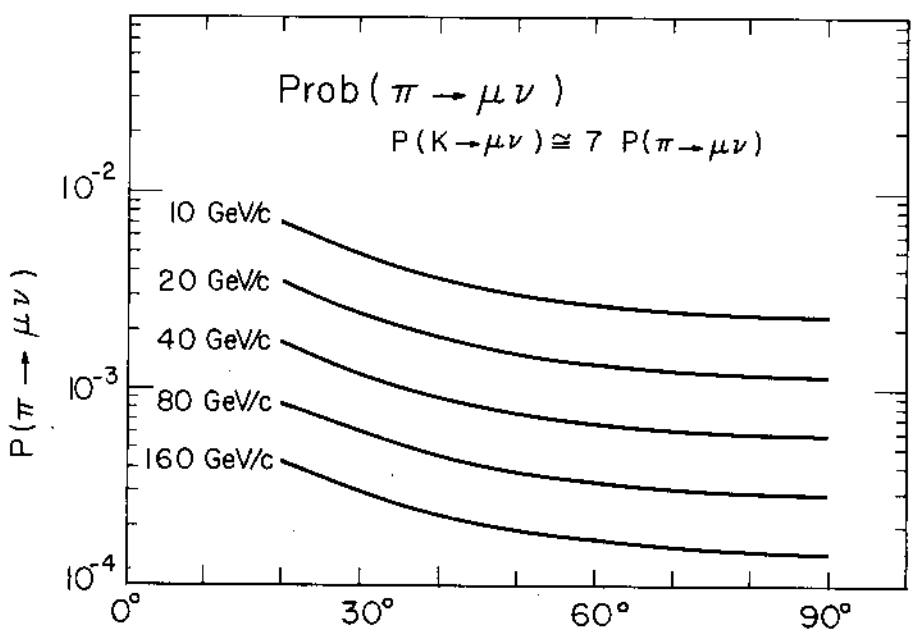

Figure 8.6 Probability of having in our aparatus one decay $\pi \to \mu\nu$ at various angles for a given momentum of the initial pion.

chosen as detectors two layers of drift tubes, as indicated in Figures 8.1 and 8.2. This seems at present a better solution than using extended planes of drift chambers.

The probability to have two tracks instead of one at a relative distance closer than 10 cm may be estimated to be $\lesssim 10^{-1}$, even in the case of jets. We therefore propose drift tubes of $\sim 5 \times 5$ cm^2, 3 - 5 m long. We also consider a similar structure at small angles, where the end-caps are present. At angles $\theta < 20^{\circ}$ the contribution of the magnetized iron to the measurement of the momentum of the particle could be more important than at 90°. This is not considered at present; but in case notice that a coil around the iron, as indicated in Figure 8.1, could give the convenient field direction inside the end caps.

The drift tubes we are considering are of the type already used in other experiments at CERN[91]. In Figure 8.7 we have given the structure of one of the two layers D_1, D_2 , and we have considered four planes for each layer. In this case the precision in position could be $\frac{1}{\sqrt{2}}$ better than in one single drift tube, that is at least $\frac{1}{\sqrt{2}}$ mm. This resolution could improve if using Argon Ethan mixture to optimize drift saturation.

It is not excluded that less than 4 planes of drift tubes, for instance 2, may be sufficient in at least one of the two layers.

The total area to be covered around the dipole and the end-caps is $\lesssim 350$ m^2. Considering two layers and four planes (Figure 8.7) per layer, this gives a total of:

$$2 \times 4 \times 350 \text{ m}^2 \text{ of drift tubes}$$

With an average length of 4 m per drift tube, we estimate a total of $\sim$ 14,000 drift tubes, in the case of 2 x 4 planes. As we said, the number of drift tubes could decrease by a factor ½. Notice that with the arrangement of the drift tubes as shown in Figure 8.7 we can get a timing on the track of 10 ns. This for instance will enable us to remove background of externally produced muons.

In case of an evoluting development of our project, the parts to

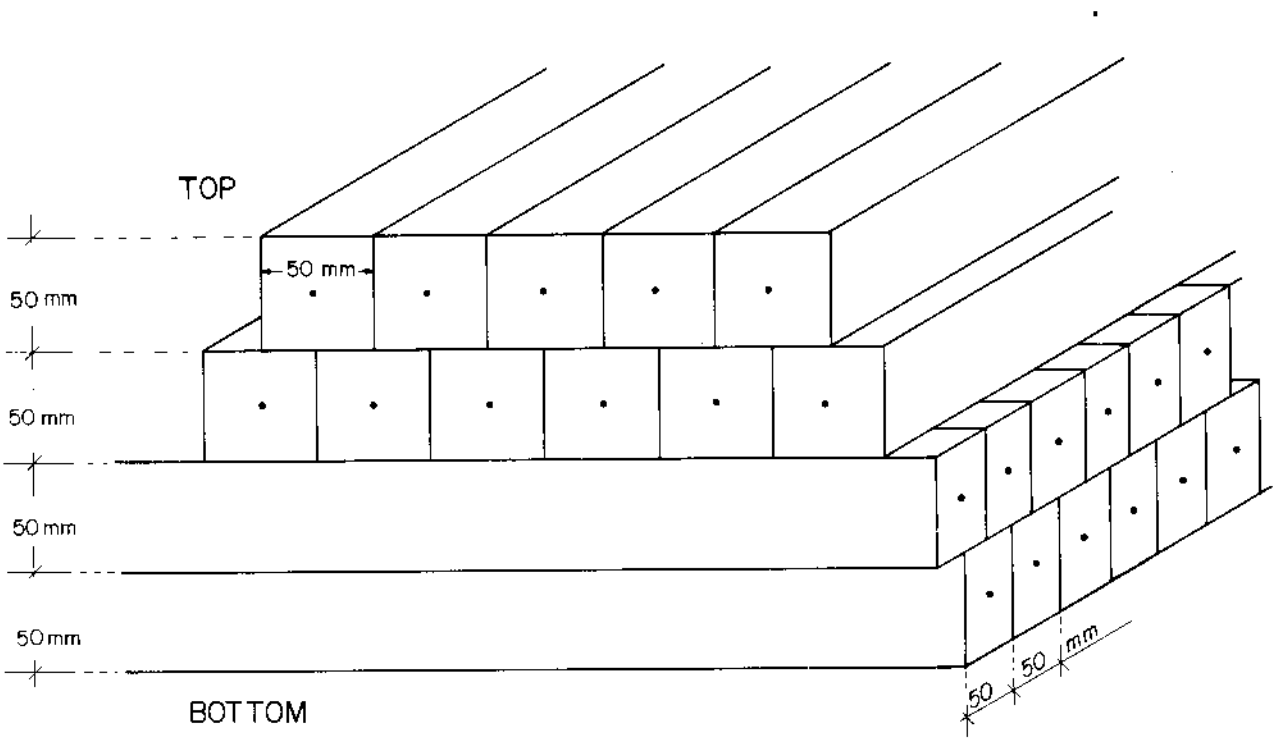

Figure 8.7 The structure of one layer of drift tubes (Fig. 8.1), if the solution of four planes of drift tubes is chosen.

be covered first with drift tubes are the top and the bottom of our dipole

8.3. PRECISION IN MOMENTUM MEASUREMENT. The resolution $\Delta p/p$ for a track inside the Central Detector is given in Figure 5.6. In order to fix the limits on the average resolution of the μ momentum, we recall the following values: for a μ of 50 (100) GeV/c the best resolution is
(1)$\Delta p/p \sim 10$ (20)% at $\theta = 90^{\circ}$, improving down to
(2)$\Delta p/p \sim 2$ (4)% at $\theta = 20^{\circ}$ (see the caption of Figure 5.6).

Further and complementary information on the momentum of a μ may come in principle from the magnetized iron (see Figure 8.1). This information will be poorer than from the Central Detector, as long as we use only the return iron of the dipole, due to the following facts:

- The Coulomb scattering of the particle in the e.m. calorimeter and in the coils ($\gtrsim$ 32 r.ℓ.), and in the iron ($\geq$ 78 r.l.)
- The curvature inside the e.m. calorimeter, which is in the opposite direction to the curvature in the iron.

We shall probably make use of the information from the magnetic field in the iron, from which alone we could get $\Delta p/p \sim 15$-20% in the 50-100 GeV range But in the following we assume that the momentum of the muons has been measured only in the Central Detector. With the resolutions indicated in Figure 5.6, we can therefore expect to get for the experimental mass of the W_o a resolution of:

$$5\% < \frac{\Delta m}{m} < 12\%.$$

Better accuracy shall be obtained in some favourable angular regions ($\theta_{\mu^+} \sim \theta_{\mu^-} \sim 30^{\circ}$) . It is interesting to note that for $W_o \to e^+e^-$ the best resolution will be instead at $\theta \gtrsim 90^{\circ}$. This means that electron and muon detection is complementary in the detection of the weak bosons. The rejection factors $\pi(\Lambda)$, $Q(\Lambda p)$, $P(\pi \to \mu\nu)$ must be compared at all angles and momenta with the expected cross-sections for hadron production and for muon emission in the decay of W_o, $W^{\pm}$. This point is discussed in chapter 13.

9. ANALYSIS OF FORWARD REGIONS.

9.1. PHYSICS MOTIVATION.

This chapter deals with the analysis of the regions which are either badly or not at all covered by the central dipole magnet.
This corresponds to the angular regions:

$$0^\circ < \theta < 5^\circ \quad \text{and} \quad 175^\circ < \theta < 180^\circ$$

where particles can escape the central detector through the holes left in between the coils of the dipole.
This region covers the rapidity range

$$3,2 < |Y| < 6,5$$

which is not the range of particles produced by $W^{\pm}$ or W^{o} decay, but rather the one of spectator jets produced in association with central jets. It is then worthwhile to cover as much as possible of that region, in order to get a full understanding of these events, and also of possible cosmic ray type events.

In fact due to the shape of the beam pipe currently under consideration (a corrugated central part, of 15 cm diameter, possibly elongated on both sides by a pipe of elliptical cross section 7 x 15 cm^2) it is nearly impossible to measure below 0.7° and for safety we shall admit a 1° cut off.

The rapidity gap covered by the forward detector will then reduce to:

$$3.2 < |Y| < 4.5$$

The remaining gap ($4.5 < |Y| < 6.5$) can only be covered with the help of highly specialized instrumentation inside the beam pipe, which is not discussed in this chapter.

Actually, for jet-type events, a Monte Carlo simulation gives the following numbers for the total energy and transverse energy appearing in the regions a,b and c, corresponding respectively to the main detector ($|y| < 3.2$), the forward detector ($3,2 < |y| < 4.5$) and the extreme forward region ($4.5 < |y| < 6.5$)

$\langle E_a \rangle \sim 130$ GeV $\langle E_T \rangle_a \sim 55$ GeV

$\langle E_b \rangle \sim 130$ GeV $\langle E_T \rangle_b \sim 3.6$ GeV

Corresponding numbers, for "ordinary" events are $\langle E \rangle_a$ = 50 GeV and $\langle E \rangle_b$ = 150 GeV, showing that, while a missing energy trigger is not appropriate for jets, the amount of energy going into the forward detector warrants its interest, both for jet-type events and ordinary events.

Consequently, the forward detector should provide, like the central detector, a good measurement of charged particles, π^0's and also $n(\bar{n})$ which represent a non negligible fraction of energy in forward jets.

9.2. DESIGN OF THE FORWARD DETECTOR

The charged particles should normally be analysed by the central detector - in the forward direction the analyzing power of the dipole is maximum ($B_o l^2 \approx 6\ Tm^2$). But due to lateral dimension of the beam pipe and the unavoidable dead space before a particle reaches an active part of the chamber, between 2.2° and 5°, only part of the trajectory is detected leading to reduced accuracy and between 1° and 2,2° a particle leaves the central detector completely undetected.

In order to detect charged particles and measure their momentum with good precision, we implement the detector outside the end caps with planes of chambers able to give a high accuracy measurement of the direction of the forward particles which leave the central detector. Knowing their direction and the vertex position obtained from internal beam parameters and other associated tracks, one can deduce the momenta of the forward particles.

The detection of neutrals is done behind the chambers using calorimeters, combining photon and hadron detection and giving both energy and direction information.

9,3. LAYOUT

Following the preceding scheme the proposed lay out is shown in fig. 9.1.

The charged particle detector is composed of two sets of drift chambers, 1 m apart, located respectively at 5.5 and 6.5 m from the interaction region.

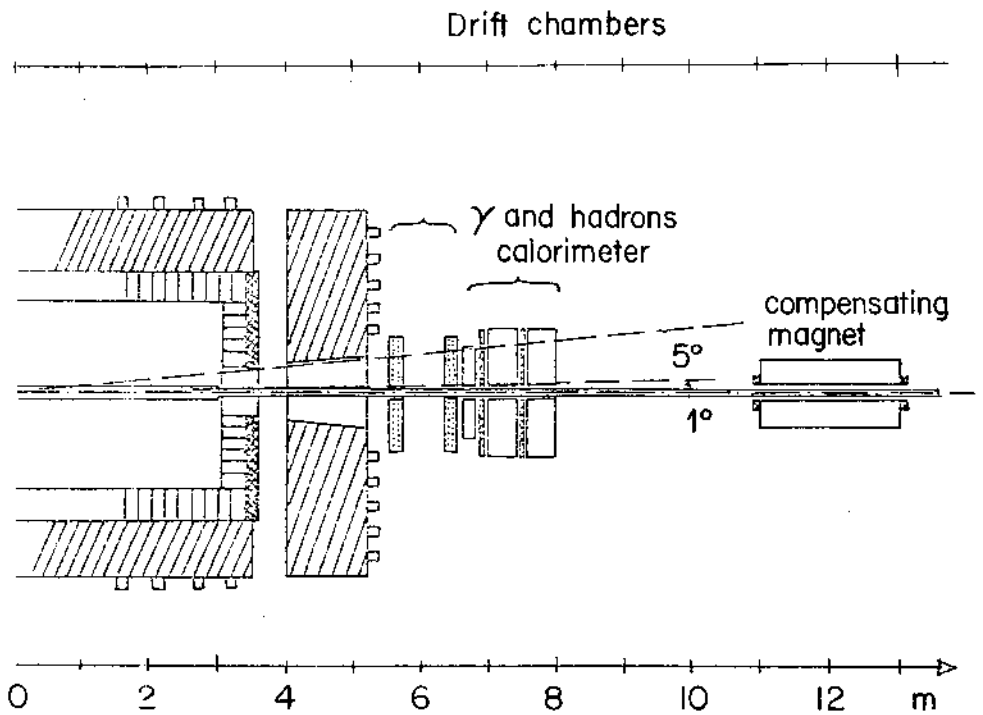

FIG. 9.1. : Horizontal view in the beam plane of the main magnet and the forward detector showing the extension along the beam direction of the main components of the detector.

The chambers will be of type already in use at the I.S.R., i.e half hexagons of 1.6 m external diameter made of 12 planes of wires . The wires are 1 cm apart and grouped in three cells of 4 wires each, along the horizontal direction and the two directions at ± 60° from it. With a lever arm of 1 m between chambers the angular accuracy is very good ($\sim 10^{-4}$ rad).

The forward calorimeter is of the type lead and iron-scintillator sandwich with the possibility of introducing two layers of proportional chambers (Fig. 9.2.).

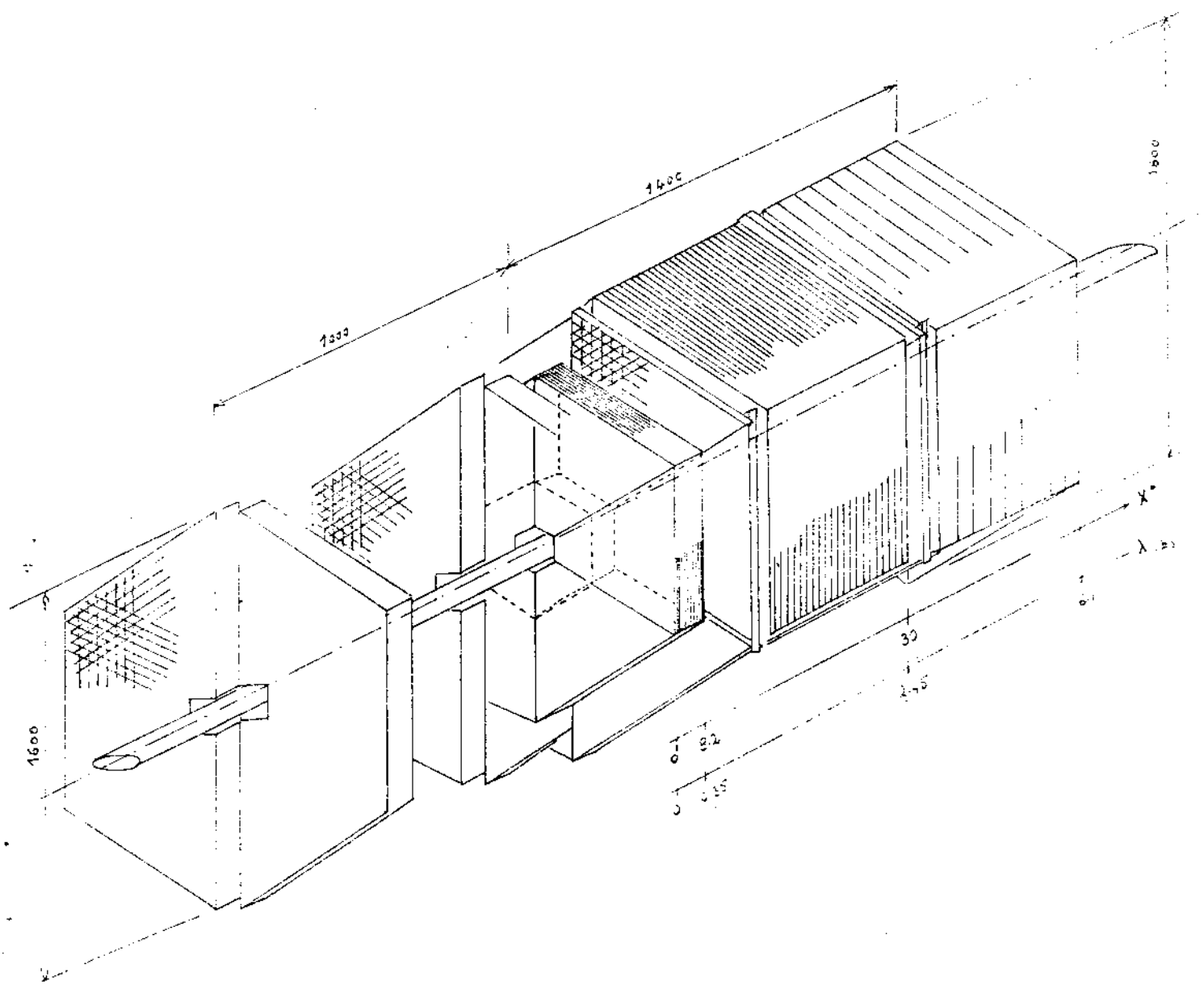

FIG. 9.2. : Cut away diagram of the forward detector showing the drift planes and the different calorimeter slices.

The first slice, in front of the proportional chambers is 8 radiation length thick and is made of 2 mm thick lead plates and 2 mm thick plexipop layers. The following slice up to 30 X_o, is made of 5 mm thick iron plates and 2 mm thick plexipop, the last part is made of iron (or aluminium) plates 5 cm thick and 8 mm plexipop layers, up to 6 λ (absorbtion length) for the full calorimeter.

The first plane of chambers after 8 X_o, will give both information on the centroïd of the shower, (5 mm expected) and on the amount of energy deposited in each shower. The space information and the determination of energy sharing between two close showers allows then the evaluation of π^o direction, the total energy being obtained by the calorimeter.

The second plane of chambers, after 30 X_o and 2.8λ , collects only hadronic showers and allows evaluation of position of centroïd although with only fair accuracy (this could be improved by using a material of lower Z than iron, such as aluminium).

The calorimeter is moreover separated in six sectors in ϕ (60° opening angle) and 2 sectors in θ : the central part covers $1^o < \theta < 2.2^o$, the external $2.2^o < \theta < 5^o$. Each sector has a separate read out. This is intended to decrease the probability of multiple hits inside the same cell. With this set up the mean number of hits is about 0.5 / sector giving a probability less than 0.09 for recording more than 1 hit in a given sector.

The diameter of calorimeter increases from 1.40 to 1.90 m along a total length of 1.40 m (if in iron) thus the forward detector ends at about 8 m from the intersection region.

2.4. PERFORMANCE

The forward charged particle detector yields [illegible] accuracy of about 3 on [illegible] parameters in the region where tracks could be measured in both planes.

Typical error values based on numbers and precision given in the text are listed in table 1.

$\theta°$	1	3	5
Y	4.7	3.6	3.2
$\frac{\Delta p}{p}$ (%)	12.6 P_t (GeV)	4.2 P_t (GeV)	2.5 P_t (GeV)
$\Delta\phi$ (10^{-3} rad)	2	0.6	0.4
$\Delta\theta$ (10^{-3} rad)	2.1 P_t (GeV)	2.1 P_t (GeV)	2.1 P_t (GeV)
ΔY	0.28 P_t (GeV)	0.09 P_t (GeV)	0.06 P_t (GeV)

TABLE 9.1.

The electromagnetic calorimeter should have the same accuracy as that foreseen in the central detector (chapter 6).

$$\frac{\Delta E}{E} = \frac{0.1}{\sqrt{E_{GeV}}} \text{ with high energy limit } \frac{\Delta E}{E} = 0.03$$

for a $\pi°$ at 3° typical errors should be :

$$\Delta\phi = 15 \text{ mrad} \qquad \Delta\theta = 0.75 \text{ mrad} \qquad \Delta Y = 0.15$$

The precision of the hadronic calorimetry benefits from the fine sampling in the first part of the calorimeter ; it could be improved if necessary by playing with the back part of the calorimeter (finer sampling and/or lighter material) with the present design, typical errors around 3° should be

$$\frac{\Delta E}{E} = \frac{0.7}{\sqrt{E_{GeV}}}$$

$\Delta\phi$ = 50 mrad $\Delta\theta$ = 5 mrad ΔY = 0.3

The combination of the three detectors should then give an adequate coverage of the forward region,

10. LUMINOSITY MEASUREMENT

The well known method originally proposed by Van der Meer[92] of displacing vertically the ISR beams in order to determine the luminosity can be easily extended to the case of the $\bar{p}p$ collider[68].

We recall that at the ISR where two coasting beams intersect in the horizontal plane at an angle α, the luminosity is given by the expression:

$$L_{ISR} = \frac{c}{(2\pi R)^2 \; h \; \tan\frac{\alpha}{2}} \; N_1 N_2 \qquad (1)$$

where c is the speed of the particles, $N_1 \cdot N_2$ are the number of particles in each of the two beams and R is the average radius. The only parameter which cannot be measured trivially is h, the 'effective height.'

In the case of the $\bar{p}p$ collider, the beams are bunched and they collide head-on. The luminosity is there given by the formula [68]

$$L_{p\bar{p}} = \frac{c}{2\pi \; R \; A} \; N_1 N_2 \qquad (2)$$

where the important quantity is now A, which is the 'effective area' of the collision. We remark that the length of the bunch does not enter directly in Eq (2) and this is due to the simple fact that two particles heading against each other always meet, no matter how long the collision volume is chosen. A similar argument ensures that in Eq (1) the luminosity does not depend on the width of the two beams.

Let us indicate with $i_1(x,y)$ and $i_2(x,y)$ the normalized current density profile of the two beams. The effective area A is then given by the expression:

$$\frac{1}{A} = \frac{\iint i_1(x,y) \; i_2(x,y) \; dx \; dy}{\iint i_1(x,y) \; dx \; dy \; . \; \iint i_2(x,y) \; dx \; dy} \qquad (3)$$

where the integrals extend from $-\infty$ to $+\infty$. The event rate I in a counter telescope looking at the (whole) interaction diamond is given by the simple expression:

$$I = \frac{c}{A} = \frac{c \iint i_1(x,y) \; i_2(x,y) \; dx \; dy}{\iint i_1(x,y) \; dx \; dy \iint i_2(x,y) \; dx \; dy} \qquad (4)$$

where c is the geometry dependent constant and A is the effective area. Following Van der Meer, we displace one of the two beams by amounts Δx, Δy in the x,y directions, respectively. The event rate becomes then $I(\Delta x,\Delta y)$. It is easy to show that the effective area is given by the integration:

$$A = \frac{\iint I(\Delta x,\Delta y)\, d\Delta x\, d\Delta y}{I(0,0)}$$

This is the so called generalized Van der Meer method[68].

An additional simplification is possible provided beam profiles are factorizable in their x, y components, as in the case of absence of appreciable couplings between the two modes. Then $i_{1,2}(x,y) \simeq i_{1,2}(x)\, i'_{1,2}(y)$ and the effective area A is given by:

$$\frac{1}{A} = \frac{1}{(w \cdot h)}$$

where w, h are the effective width and height given by:

$$w = \frac{\int i_1(x)\, i_2(x)dx}{\int i_1(x)dx \int i_2(x)dx}$$

$$h = \frac{\int i'_1(y)\, i'_2(y)dy}{\int i'_1(y)dy \int i'_2(y)dy}$$

They can be determined separately with two Van der Meer scans in the vertical and horizontal planes.

In order to achieve a physical separation of the beams electrostatic fields must be employed. The procedure requires the use of a pair of electrostatic deflectors. In our case, at E_o = 270 GeV and $E_y/\pi = 10 \times 10^{-6}/\beta\gamma$ rad·m = 3.47×10^{-8} rad·m, the angular divergence for 2 s.d. points and β_y = 40 m is given by:

$$\theta_y = \sqrt{\left(\frac{E_y}{\pi}\right) / \beta_y} = 2.95 \times 10^{-5} \text{ rad}$$

The electric deflection angle θ_{ed} produced by a field E over a length ℓ is given by:

$$\theta_{ed} = 10^{-9} \frac{E\ell}{2\beta E_o} \qquad \text{(units GeV, Volt)}$$

Setting $\theta_{ed} = \theta_y$ for a confortable 4 s.d. separation between the two beams, we get $E \cdot \ell \simeq 2 \times 10^9 E_o \theta_y = 1.59 \times 10^7$ Volt, equivalent to about 10 m of an electrostatic field at 16 kV/cm (1.6×10^6 V/m).

The small telescopes of counters subtending angles of about 10^{-3} rad at the end of each side of the straight section are used to count elastically scattered protons. The total cross section is determined by extrapolation to the forward direction and the Optical Theorem.

11. TRIGGER

11.1 Experimental signatures

The various detector components we have described will give us the possibility of requiring very specific experimental signatures for the recorded events.

(a) High transverse energy. Our calorimeters (electromagnetic and hadronic) cover the angular region from 5 to 175°. Very little transverse energy could escape at low angle and a trigger above a transverse energy cut, if set high enough, can reduce the trigger rate to any preset number. Rates are estimated in section 13 below (table 13.5). It may be seen that with a trigger on a transverse energy greater than 40 GeV (i.e. two 20 GeV/c P_T jets), the rate will not exceed one in every five seconds, even if we take into account the effect of the resolution of the hadronic calorimeter (a factor 4 in trigger rate in this region[33].)

More refined characterization can be made. For instance, checks can be done on transverse momentum imbalance between the two halves of the detector, numbers of elements recording more than a preset energy, disproportion between electromagnetic and hadronic charges etc.

(b) Electron. A high energy electron could be characterized by a signal in the first layer of scintillator of a "gondola", a sizeable electromagnetic energy and no energy release in the associated hadron calorimeter. The modest rejection factor obtained in that way (5 to 10) may be sufficient at trigger level if combined with transverse energy cut. Taking into account the ratios between successive layers of the shower counter can increase, if necessary, the rejection to about 50.

(c) Muon. A muon of more than 1 GeV/c transverse momentum could be identified by the requirement of a minimum ionizing particle in most layers of the electromagnetic and hadron calorimeters, and a local coincidence with the muon chambers. In addition, we could impose that hits in the two separate planes of muon chambers project an approximate road to the interaction region, at least in the projection along the beams.

(d) Quarks or abnormal ionization particles will be identified by the pulse height of the sense wires of the central detector. A large number of low pulse heights can form a rough trigger which could, in connection with another requirement, give reasonable rates.

When combined together, these triggers can be very powerful. For instance, the leptonic decay of W^o's or ordinary vector mesons can be selected efficiently with a two-electron or two-muon trigger. e-μ coincidence could be a signature of heavy leptons or flavoured objects. A high transverse energy electron or a single muon with no transverse energy seen in the detector, would signal $W^{\pm}$ candidates.

Requiring a large global transverse energy is an unbiased way to trigger on multi jet hadronic interactions.

Triggering on very large multiplicities (e.g. most of the "gondola" scintillators hit) will enrich our sample in abnormal events, such as the "Centauro's" hinted at by cosmic rays.

Quarks may be looked for in pairs or in association with some dramatic characteristics of the event.

These examples show the selectivity and the versatility of the triggers we can implement with our detector. In addition we will run part of the time with an interaction trigger where we will record "minimum bias" events which will be very useful, both for the understanding of the apparatus and for having a clear view in the new energy regime.

11.2 Background

In addition to the normal hadronic events, we will have to reject the following obvious types of background.

(a) Cosmic ray. The rate in the detector is of the order of 4000 per second. This is easily cut down to a negligible amount by the combination of timing (5 ns beam gate giving a rejection 10^3), requirement that the particles come from the interaction region, presence of particles in the forward cone, etc.

(b) Machine background and beam gas interactions. We would request a vacuum of 10^{-10} torr close to the interaction region. Beam gas rate over 50 m is then 1.4×10^{-3} per beam crossing. Limiting apertures far from the interaction region will scrape particles on the verge of being lost. In addition, we will install two shielding walls on each side of the apparatus which should complement the natural shielding provided by the hadron calorimeter. It will help in keeping neutron background small. Some muons will presumably also be trapped in the lattice. Note that all these backgrounds are in time with the beam crossing.

Most of these sources will give a relatively low amount of energy, which will not trigger the apparatus. The additional requirement that tracks come from the interaction region will help rejecting them.

(c) Multiple interactions. At full luminosity, there is a 2% chance of having more than one interaction per beam crossing. This type of event will be favoured by the trigger described above, especially multiplicity and total large angle energy triggers. However, transverse energy triggers are not very much affected: for instance, if we require a 20 GeV transverse energy jet, a double interaction event can pass the cut if both interactions have produced 10 GeV transverse energy jets. However, the probability of having a 10 GeV jet is 0.5×10^{-5} per beam crossing and the combined probability is very small. It is easy to reject these events off-line, since particles emerge from two different vertices.

11.3 Triggering scheme

The main triggering task of our apparatus can be characterized as follows. We would like at the same time, to record "extraordinary" events with minimum dead time in order to make full use of luminosity and also record as many nearly normal events as possible in order to make full use of the machine time. On the other hand, a typical event may have 13 000 16-bit words and with present techniques, it seems difficult to store such an event into a buffer in less than 2 ms. The recording speed will be limited to 40 events a second. A reasonable use of the luminosity would require a selection factor of one in 10^3 which is relatively high.

In order to deal with these problems, we propose to use two concepts for the organization of the trigger logic:

(a) Multilevel trigger. In order to be able to get sufficiently high rejection, we will take full advantage of the bunched structure of the machine and organize our trigger in 3 levels.

- Level 0 will be simply a beam gate which will strobe the pulse height from the phototubes and eliminate most cosmic rays.
- A level 1 decision could take up to 4 μs using analog information from the phototubes and some chamber information. The decision will be to accept or reject the beam crossing. In the latter case, relevant memories will be cleared in the remaining 0.6 μs before the next beam crossing.
- A level 2 decision would then be made in, say, 100 μs, using more sophisticated logical devices. If at level 1, 99% of events are rejected, the remaining 500 Hz rate will introduce a dead time of 5%. If the decision is positive, the information will be retained and transferred into a "first in first out" buffer in about 2 ms.

(b) Parallel processors. In order not to miss "extraordinary" events such a W's because of excessive dead time, we propose to have two parallel chains of decision. One chain will be devoted to "extraordinary" events that we could call the "high priority" chain, and another one the "low priority" chain which handles "ordinary events (and possibly "extra-ordinary" events when available). This concept is close to the one of parallel processors in computers, with one processor dedicated only to high priority requests.

The implementation of this scheme is possible because á cut on transverse energy is very powerful in restricting the flow in the "high priority" channel to any predetermined level. This concept offers considerable safety since attempts to decrease trigger threshold that we will make for low priority events, will not spoil the trigger efficiency for high priority ones.

A possible way to implement these two principles could be the following:

- To each digitizer we attach two memories instead of one through a "toggle switch" (Fig. 11.1). At a given time, one memory is used for low and high priority events and when it is busy, the other memory is used for high priority events.

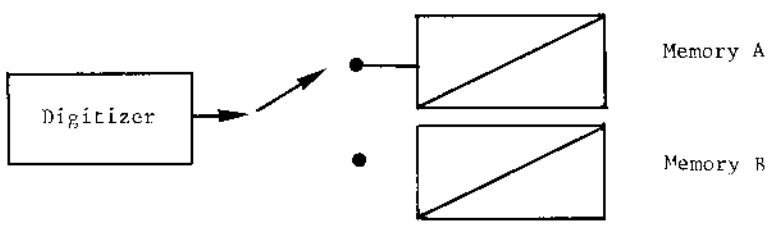

Figure 11.1 . Schematics of two memory scheme.

- The time sequence that could be used is schematized in Fig. 11.2. The two parallel chains of decision are shown in the centre of the figure. Let us distinguish two cases:

(a) The level 2 low priority chain is available. Immediately after beam crossing acceptance and digitization of the current event digitizers are switched to the other memories. In this way search for extraordinary events can go on during level 2 processing. Note that in this particular scheme, digitizing will have to be done in less than 4.0 μs.

(b) Level 2 low priority processor is busy. In this case events which are classified as "low priority" at the end of level 1 are rejected. Only "high priority" events are accepted. Since there is no more memory available the clock and beam gate are stopped, and the information is held in the memory. Only after processing and, if applicable, transfer to the buffer (or after the low priority level 2 processor has finished) the clock is re-started, memories are cleared, and a new beam crossing can be analyzed.

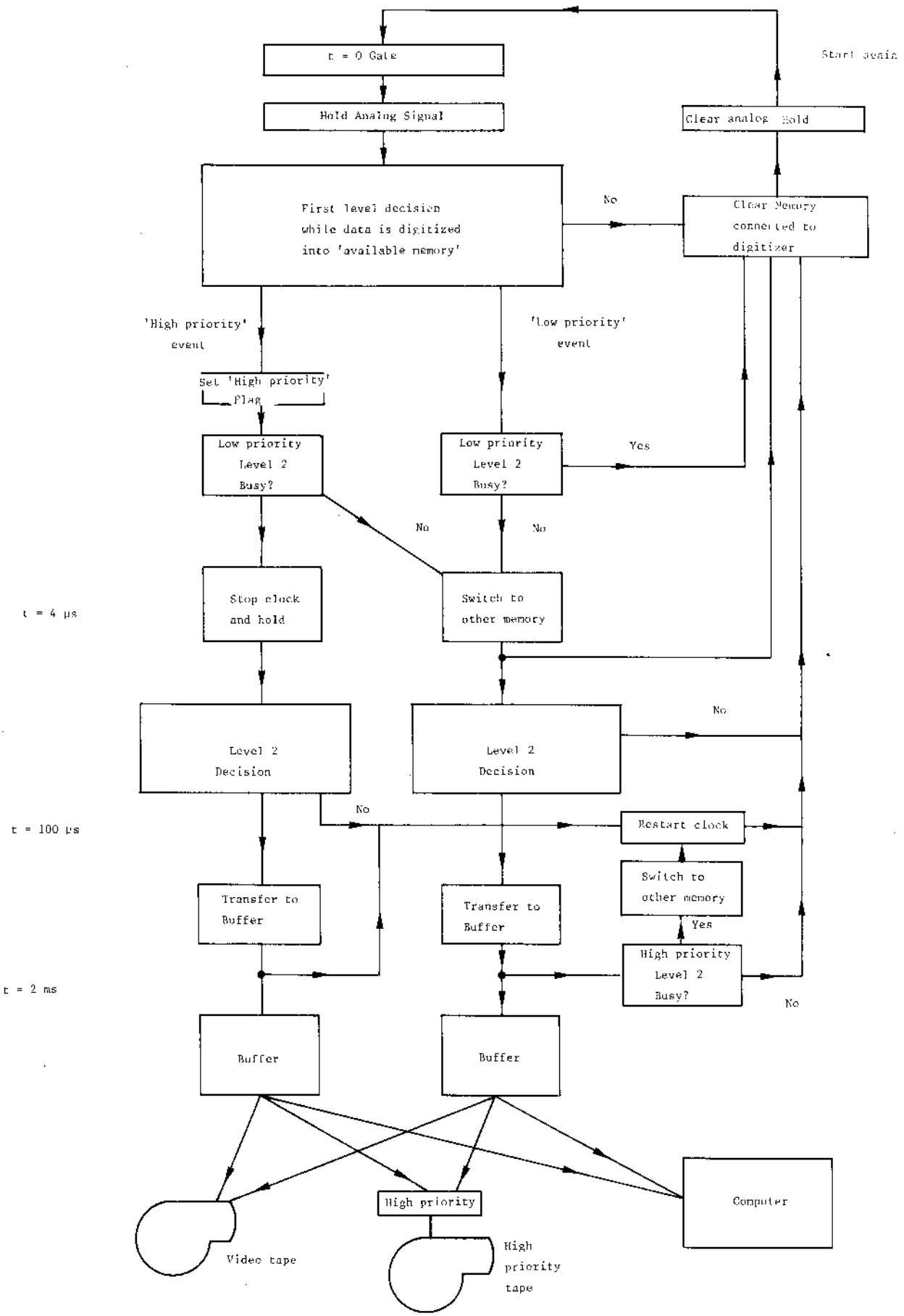

Figure 11.2. General flow diagram.

11.4 Level one processor

Let us sketch what could be the level one processor. We visualize it mainly as an analog processor treating pulse height data from the phototubes. Figure 11.3 gives the schematics of a possible scheme.

We have about 2000 phototubes for which the information is sampled and held. They are processed in two different ways:

- A rough muon trigger is generated by grouping layers which are aligned to the interaction region. We will require a minimum ionizing particle in most layers and a local coincidence with the muon chambers.
- We will also be able to trigger on quantities of the type:

$$\Sigma_i W_i E_i$$

where i is the index of the phototube, E_i the energy seen by it, and W_i a programmable weight (which could be negative). This operation is performed by an analog multiplier (see Fig. 11.3)

Such an operation is quite powerful since it allows triggering, for instance, on total energy, transverse energy, transverse energy imbalance between left and right, etc. Other possibilities would be to trigger on the greatest of all $W_i E_i$ (using a linear amplifier with a diode in the feedback loop) or on a minimum number of $W_i E_i$. We will have several (say 5) parallel processors of this type, in order to be able to run simultaneously with many triggers, or to combine them.

Some information can also be obtained from the central detector chambers at the end of level 1 processing time. We plan to have at least the following two outputs from each of the channels:

- An analog output which could be summed by regions in the detector and integrated. In this way we will have information on the "activity" in various parts of the detector and in particular know whether tracks are present close to the interaction region.
- A latch or counter recording the pulses significantly below minimum ionizing. Although in most cases there would be spurious pulses due, for instance, to cross talk or large pulse tails, requiring a large number of them (100 or more of the 200 expected for a track)

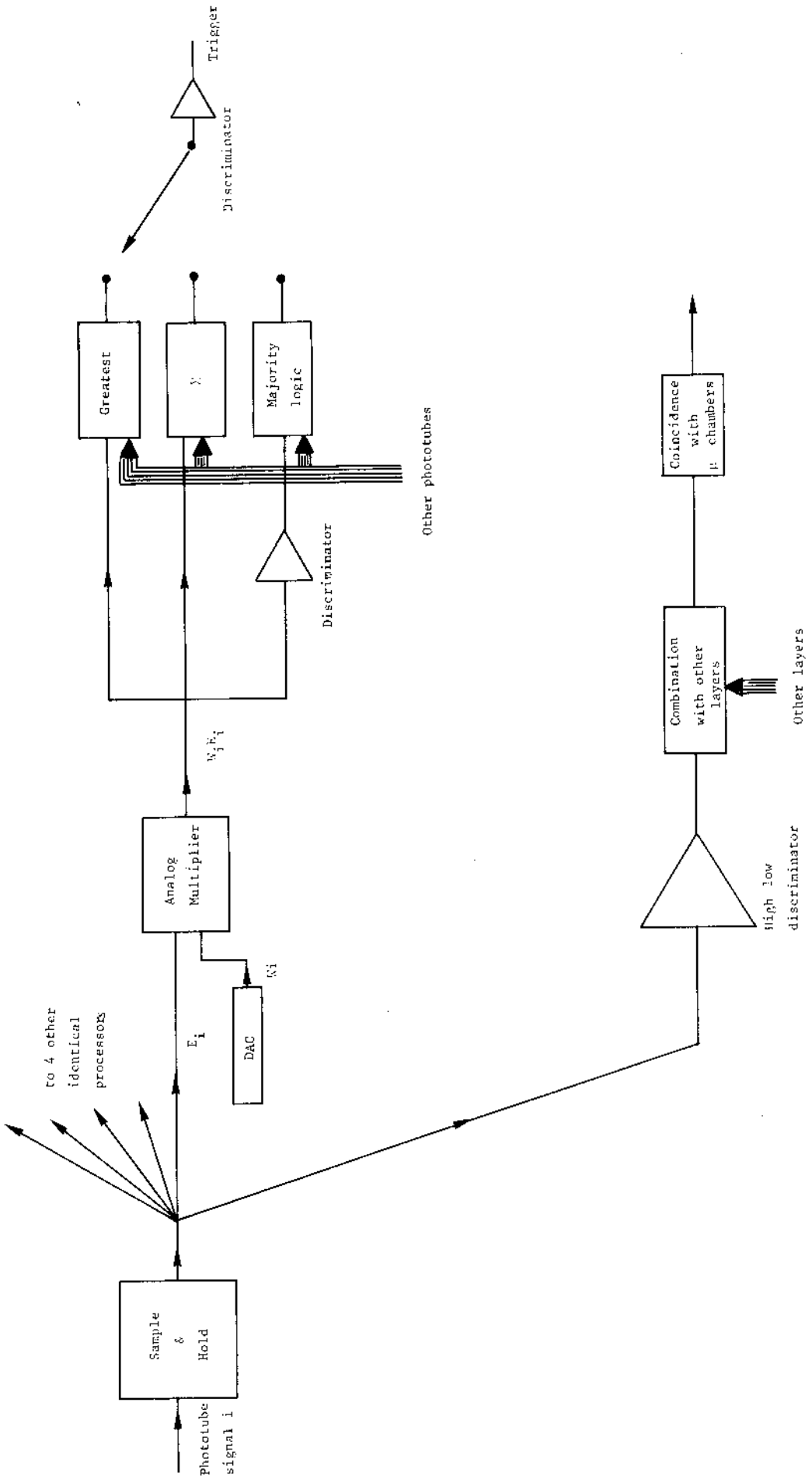

Figure 11.3. Schematics of level one photomultiplier logic

on successive wires may be a sufficient level one quark trigger, if combined with abnormal pulse height in one of the scintillators of the first layer.

11.5 Level two processors

At this level, we will have access to the digital information and we could have more sophisticated checks. Let us, however, emphasize that this is probably not necessary for "extraordinary" events which have obvious signatures such as 30 GeV transverse energy. Refined triggers will only help us to reduce thresholds for our "bread and butter" events or tighten difficult triggers such as muon and quark triggers. Let us list a few ideas which could be implemented.

Phototube information can be reprocessed in order to combine successive layers. In this way an e, π^0, or hadron signal can be generated and threshold for an electron transverse energy reduced.

Chamber information can also be treated in more detail. We have in particular investigated the possibility of using a few wires of the central chambers for recognizing the vertex. The simplest way may be to look along the beam, in which projection the tracks are straight and the vertex position known. Ratio of pulse heights with look up tables provides the current division coordinates which could then be scanned for straight tracks pointing to the vertex. Other potential triggers could be association of quark candidate points into tracks, check that muon track candidate points to vertex, etc.

12. DATA ACQUISITION SYSTEM

12.1. INTRODUCTION. The large amount of information generated at each event by the central detector, and the potentially high trigger rate of the potentially high trigger rate of the physical reaction, demand unconventional data acquisition system solutions.

A high data-rate and high capacity mass-storage device has to be used, while suitable computing power has to assure the first step of the data processing for the production of data summary tape of selected events.

In Figure 12.1 the block diagram of the data acquisition system is presented. The type of computers and the technique adopted for the mass-storage device are only indicative, the discussion on their definitive choice will continue.

Three distinct processor share the main functions of the data acquisition system. During the data taking a standard minicomputer (e.g. HP21MXE) transfers the data from the CAMAC system to the mass-storage, while data samples are sent to the analysis processor (e.g. NORD10/50) and to a second minicomputer (e.g. HP21MEX) used for the control of the apparatus. During the off-line session, data flow from the mass storage to the processing computer where data summary-tape are produced, while the test and calibration of the apparatus can be continued by the control computer.

12.2. DATA READOUT. The information content of a single detection can be represented by 48 bits (Table 12.1, organized in 6 bytes of 8 bits each, giving the hit wire number, the drift times (first and last), the wire-end pulse heights and an additional byte to keep account of the wire multiplicity and the data structure. Assuming that a typical event has 18 charged tracks (3 tracks * 6 units of rapidity) and that the average number of detections per track is 200, then the total data coming from the central detector are about 1.7×10^5 bits. Including the calorimeters data, a full event will be represented by 2×10^5 bits ($\sim$ 13000 16 bits words).

At a CAMAC transfer rate of 1 word in 2 μs, an average of 30 events/sec can be collected by the acquisition computer. To reduce

the effective readout dead time and in view of implementation of higher data transfer rates, all the CAMAC crates are read in parallel by autonomous intelligent controllers an data are temporarily stored in memory modules. This local crate processing power can also be used to structure the data in a suitable way to minimize the time of sorting operations during the analysis phase in the off-line session.

12.3. MASS STORAGE. The mass storage device has to deal with a data-rate of the order of 1 Megabyte/sec. Although 6250 Bpi magnetic tape units will soon be available for the minicomputer system, the expected data volume makes their use unpractical (tape can be filled at the rate of 1 tape in 130 seconds).

Video tape or optical holographic techniques are thus necessary to cope with the high data-rate while maintaining reasonable data compactness. In Table 12.2 some of the performance characteristics of the mass-storage device are compared.

A detailed study has to follow for the choice and the impementation of such a mass storage device.

12.4. APPARATUS CONTROL. A second standard minicomputer (e.g. HP2MXE), running a real time executive system, assures continuous control of the apparatus technical parameters, and interfaces the experimenter to the rest of the acquisition-storage system.

Periodic measurements of each detector element efficiency are made; either on-line with the statistics of the data samples received from the acquisition computer, or off-line by simulating physical processes in the central detector and in the calorimeters.

Other tasks of this processors are the on-line event data display, the log-booking of the data acquisition and machine conditions, hardware parameter setting and calibration, module tests and software development. 'Mini-experiments' based on a small subset of the data can have place in this stage with independent production of data summary tapes.

12.5. DATA PROCESSING. The last level of the event trigger takes place in the off-line phase, play-backing the data from the mass-storage to the medium size computer (e.g. NORD10/50).

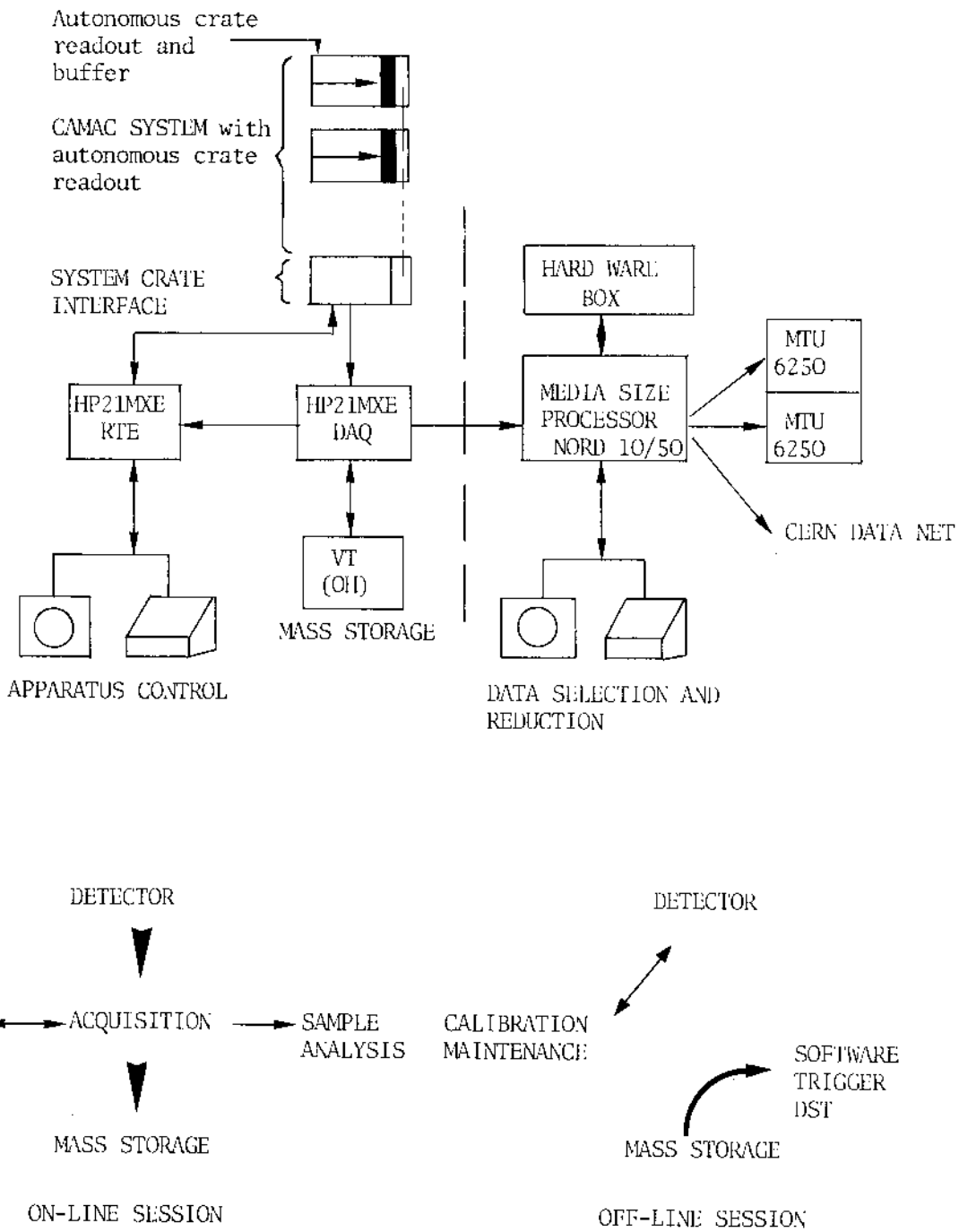

Figure 12.1 Data acquisition system

Different 'experiments' can be runned on the antiproton-proton data bank of the mass storage; events are selected on the basis of energetical and geometrical conditions and the redundant information ca be reduced in rpoducing the data summary tapes.

Hardware bixes and interactive praphic facilities are foreseen as well to speed up the pattern recognition programs and for the visual search of unusual events.

Finally, during the data acquisition, sample events are analyzed on-line by the data processing computer to monitor the experimental apparatus behaviour with the evaluation of physical parameters characteristics to the studied reaction and the machine conditions.

TABLE 12.1. Events information.

Single deviation information:

Wire chamber	8 Bits
Drift times	16 Bits (8+8)
Pulse heights	16 Bits (8+8)
Data flag	8 Bits
Total information/detection	48 Bits

Central detector information:

No. Bits/detection	48
No. Detections/track	$\sim$ 200
No. Tracks/event	$\sim$ 18
Product	1.7×10^5 Bits
calorimeters	$.2 \times 10^5$ Bits
Total event size	2×10^5 Bits (1.3×10^4 16 Bit word)

TABLE 12.2. Mass storage

	Density Bits/In^2	Rate Byte/sec (Ev/sec)	Capacity Byte/Reel (Ev/Reel)	Filling Time per Reel
6250 BpI MTU	$1.1x10^5$	10^6 (40)	$1.3x10^8$ ($5.2x10^3$)	130 sec
VT	10^6	$.72x10^6$ (29)	$9.3x10^9$ ($3.7x10^5$)	3430 m
OH optical holographic	$2x10^7$	$.6x10^6$ (24)	10^4 ($4x10^6$)	46420 m

13. RATES, RESOLUTION AND BACKGROUND

13.1 Assumptions

It is obviously difficult to estimate rates and backgrounds for an experiment which will run in a new energy domain. The assumptions made for this section are our best guesses from indications of cosmic ray, and ISR experiments and present theoretical expectations. It is not unlikely that what we consider today as a background for our physics programme will turn out to be much bigger than expected and be one of the fascinating outcomes of the experiment.

In this section, we will focus on our two main physics objectives, namely the search for intermediate bosons and the study of the dynamics of hadron constituents through large p_T scattering. In order to estimate rates, we have followed [94] the present theoretical "orthodoxy".

Partons are identified to quarks and for their distributions inside the nucleon, we have taken the parametrization of Donnachie-Landshoff. We have supposed the existence of only four quarks and of three colours No asymptotic freedom effects have been included, since they are small.

For the production of W's, we have taken matrix elements from the Weinberg-Salam model with $\sin^2\theta_W = 0.3$. The mass of $W^{\pm}$ and W^o are then 69 GeV/c^2 and 82.5 GeV/c.

For the production of hadronic jets, we have taken for consistency, the vector gluon model which is expected to dominate at high p_T.

The decay of the jet into hadrons, has been parametrised in a Monte-Carlo program [95] in the usual fashion (limited transverse momentum, $(1-Z)^2$ distribution for quark fragmentation).

For single particle production, the coupling constant of the jet model is fixed to reproduce the $p_T = 8$ GeV/c measurement of inclusive π^o production by the CCRS collaboration [96] at the ISR. This is five times as big as the estimate of Peierls et al.[18] who chose a different quark fragmentation function (1-Z). According to our present understanding this represents an upper limit for hadron production and is therefore appropriate for background calculation. When computing jet rates [19] on the other hand, we have taken the more conservative normalisation of Peierls et al.

The integrated luminosity has been chosen arbitrarily to 10^{36} cm^2. For instance, this could correspond to 1000 hours of running at a peak luminosity of 10^{30} with a ratio 0.6 between peak and average luminosity, and a 50% global efficiency factor (e.g. down time of the apparatus, deadtime, inefficiency in analysis etc.).

13.2 Leptonic decay of charged W

Fig. 13.1 gives the p_T distribution of the charged lepton for either one of the two reactions

$$\bar{p}p \to W^- + X \quad \text{or} \quad \bar{p}p \to W^- + X$$
$$\qquad\quad \hookrightarrow e^- \bar{\nu} \qquad\qquad\quad \hookrightarrow \mu^- \bar{\nu}$$

at $\sqrt{s}$ = 540 GeV. We have distinguished between leptons going along the $\bar{p}$ beam ("forward" leptons) and those going in the opposite way and between three angular regions:

$40^\circ < \theta < 90^\circ$ and $25^\circ < \theta < 40^\circ$ corresponding to the "barrel" part of our detector, and

$5^\circ < \theta < 25^\circ$ which is covered by our "end-caps".

The "Jacobian" peak is clearly seen, at least for the first two angular ranges. Our experimental resolution will degrade these peaks very little. For electrons, it will be completely dominated by systematic errors and be at the level $\Delta p_T/p_T \sim 2 \div 3\%$ r.m.s (sect. 6.3.1). For muons, it will vary over the angular region. Assuming that the accuracy of the central detector is dominated by systematics at the level of 100 μ r.m.s. on the sagitta, the resolutions are (sect. 5.4.3):

$40^\circ < \theta < 90^\circ$ $\qquad \frac{\Delta p_\perp}{p_\perp} \sim 16\%$ r.m.s. (for a muon of more than 30° with respect to the magnetic field)

$25^\circ < \theta < 40^\circ$ $\qquad \frac{\Delta p_\perp}{p_\perp} \sim 8\%$ r.m.s

$5^\circ < \theta < 25^\circ$ $\qquad \frac{\Delta p_\perp}{p_\perp} \sim 5\%$ r.m.s .

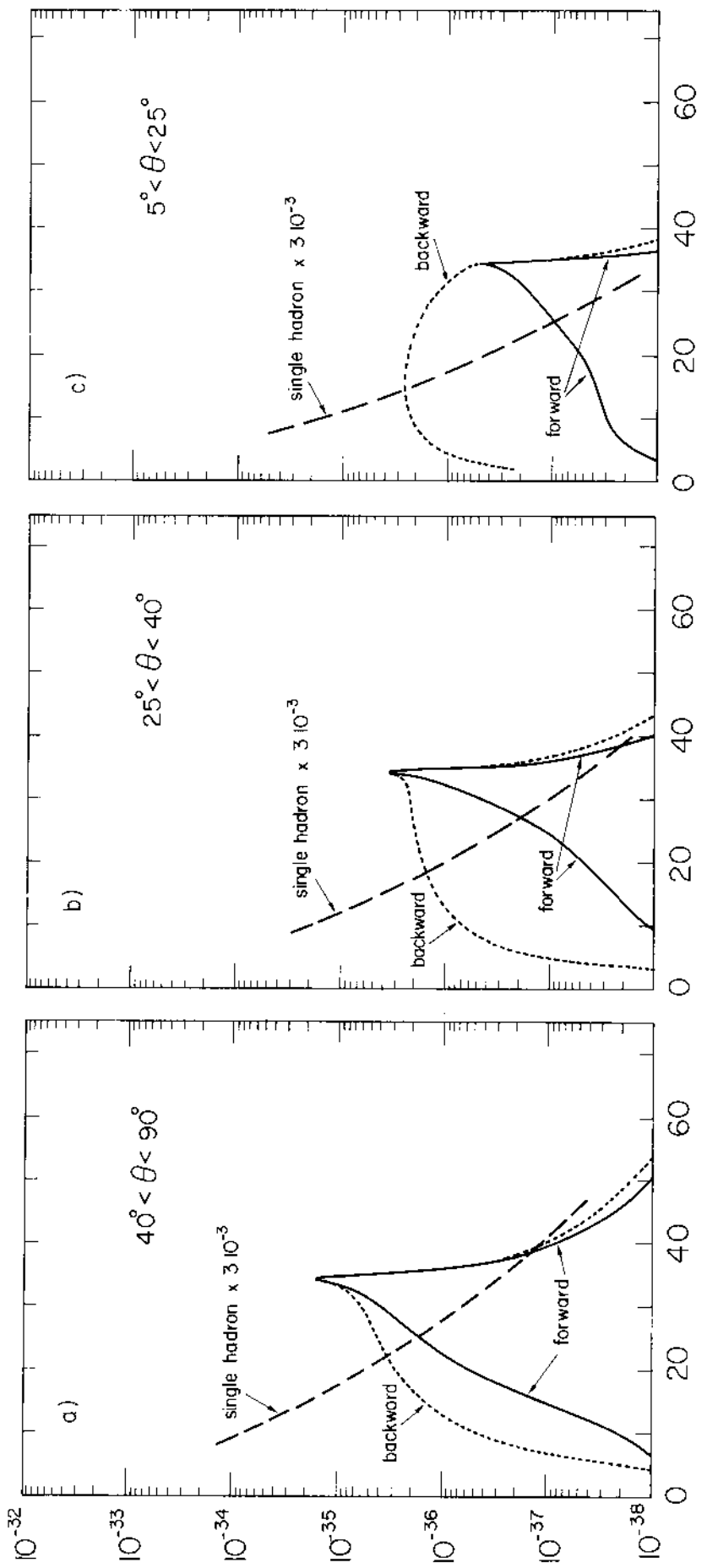

Figure 13.1. B $d\sigma/dp_T$ for $p\bar{p} \rightarrow W^- + X$ (or equivalent $e^-\nu$). For three regions: (a) $40^\circ < \theta < 90^\circ$, (b) $25^\circ < \theta < 40^\circ$ and (c) $5^\circ < \theta < 25^\circ$. Full lines refer to forward lepton, that is a lepton minus going along the antiproton direction. Dashed lines refer to backward region. Dashed lines indicate the estimate of the muon background ($\sim$ hadron distribution x $3\ 10^{-3}$). The electron background will be three times smaller.

Another cause of the smearing out of the peak, would be production of the W with large momentum. Experiments [18] at Fermilab indicate a stabilization of the mean transverse momentum at 1.5 GeV/c at large dimuon mass. If this remains the case for the W, the jacobian peaks will not be degraded substantially. Even with a transverse momentum of 6.5 GeV/c (coming from a scaling as $\sqrt{M_{ee}}$) the peaks will still be seen [94] We are therefore confident that the p_T distribution will allow us to determine the mass of charged W.

Fig. 13.1 also shows the estimated background for muons. In sect. 8, we have seen that two effects are dominant. At $p_T \sim 35$ GeV, π-μ and K-μ decays will contribute at the level of $2\ 10^{-3}$ and punch through will contribute another 10^{-3} giving a proportion of hadrons wrongly identified as μ's of $3\ 10^{-3}$. For electrons, we expect a hadron rejection three times as good (sect.6.3.2). Dalitz pairs and conversion in the beam pipe, contribute at the few 10^{-4} level because of the parent - daughter p_T relation. To reduce the contamination of hadrons we may be obliged to make a cut $p_T \sim 20$ GeV/c.

Another possible technique for reducing the background may also be used. With the combination of the charged particle detector, shower counter and hadron transverse calorimeter, we measure the energy flow over the range $5^o < \theta < 175^o$. A W will be characterised by a large transverse energy imbalance. For an hadronic event to simulate such a configuration, it should be such that a high transverse momentum jet is produced and decays in only one energetic particle (e.g. $p_T \gtrsim 10$ GeV) which fakes a direct lepton. The other jet gives most of its energy in the forward or backward direction ($|y| > 3$). The first condition already decreases the hadronic cross section to the level of the W $\rightarrow$ lepton ν cross section. The second condition is very stringent as shown in fig. 13.2, a scatter plot of the transverse energy in one hemisphere versus the transverse energy in the other hemisphere for jets and W's (see caption for details). Although this plot assumes 100% acceptance over our detector, and the rejection is model dependent, we can, however, conclude that this transverse energy imbalance condition is a very powerful tool. It may allow to decrease the p_T cut to 10 GeV/c and get significantly higher efficiency for the study of forward backward asymmetry which is more pronounced for low p_T (fig. 13.1). Note that it is absolutely essential for this selection to be fully operative to have complete coverage down to an angle of 5^o.

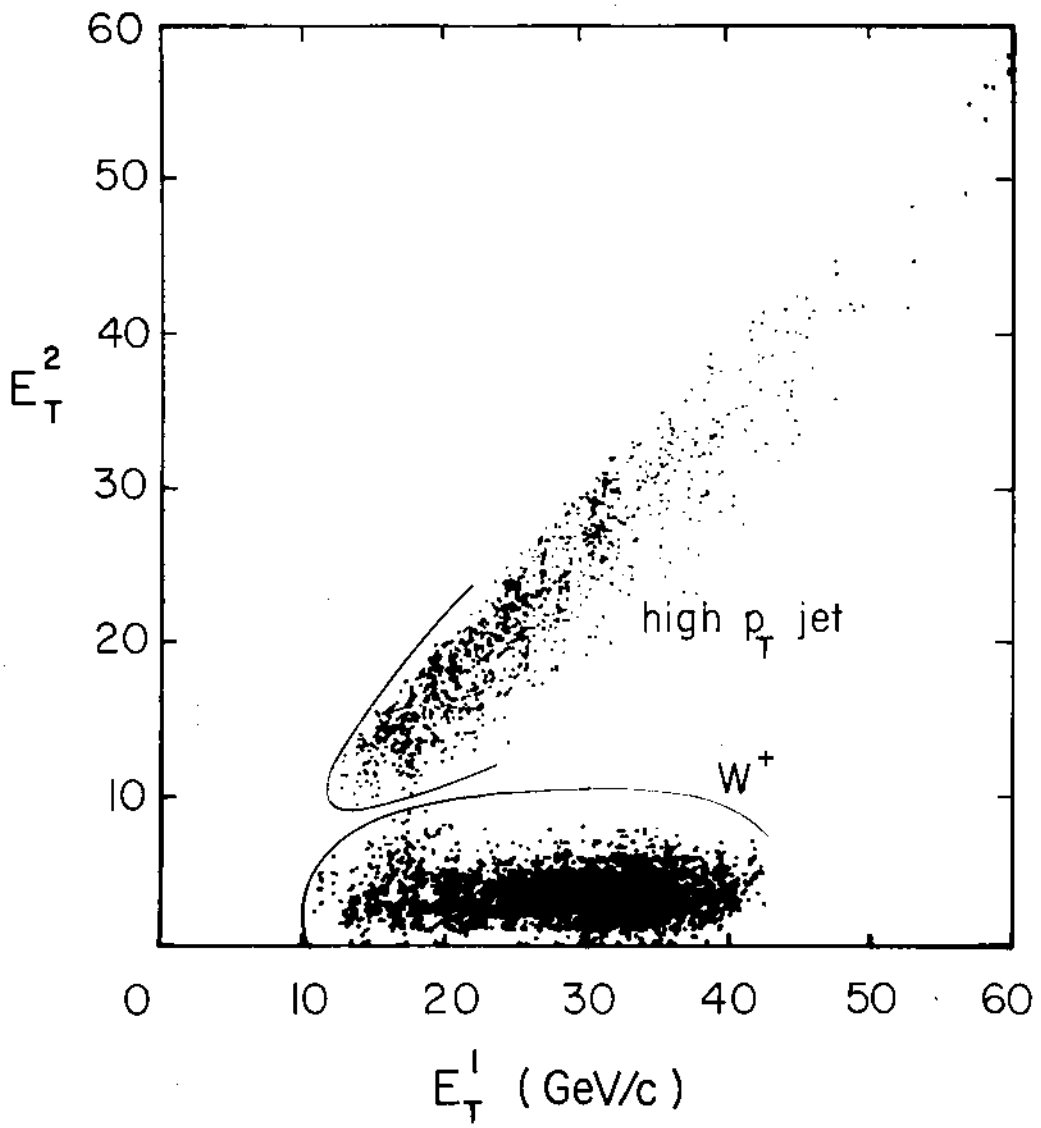

Fig. 13.2 Monte-Carlo simulation of events in our detector, assuming 100% acceptance for $5^o < \theta < 175^o$. A lepton with $p_T > 10$ GeV/c has been found. One computes $E_T = \sum E_T^i$, sum of the transverse energies of all the particles with $5^o < \theta < 175^o$ in the lepton hemisphere (i.e. $|\phi_i - \phi_{lept}| < 90^o$) and in the opposite one, hence two quantities called E_T^1 and E_T^2 which are plotted one versus the other on the figure ($E_T^1 > E_T^2$). The bottom cluster corresponds to $W^{\pm} \to \ell^{\pm}\nu$ production (high p_T neutrino missing). The points close to the diagonal correspond to high p_T jets where a fast π,K ($p_T > 10$) gives rise to a lepton. The two cluster widths include a gaussian error distribution: $\sigma = \Delta E_T/E_T = 100\%/\sqrt{E}$ on each E_T determination.

In order to estimate the rates, we finally need the detection efficiency for leptons in our apparatus. The muons are identified with an efficiency close to 100% (say 95%) over the solid angle covered by the muon chambers. Since we have eight layers of muon chambers, dead space is negligible. However, the muon is not measured accurately if its angle with respect to the magnetic field is too small. We do not know the exact dependence of our accuracy with this angle (sect. 5.4.3). However, we can safely assume that there is no problem above an angle of 30° and the efficiency are computed cutting out events below this angle.

A similar cut should be applied to electrons since it is the momentum resolution which reduces hadron feed through from a few percent to 10^{-3}. For simplicity we take the same angular criterion. In addition, the many cuts involved in this electron analysis will decrease the electron efficiency to 80%. All these considerations result in the efficiencies shown in table 13.1 and rates given in table 13.2.

Therefore if the charged W exists at a mass around 70 GeV/c and is produced according to expectation, our detector will be able to detect more than 700 unambiguous decays ($W^{\pm} \rightarrow \mu^{\pm}$, $e^{\pm}$) per 10^{36} integrated luminosity. At a mass of 200 GeV/c this rate would be divided by 5.

13.3 Leptonic decay of neutral W

The leptonic decays of the neutral W^{o} are much easier to detect since two charged leptons are produced. The only experimental difficulty comes from the fact that the two leptons are coplanar with the beam but uncorrelated in polar angle (for W^{o} mass below 120 GeV/c). In order to detect both of them with good efficiency, it is important to have a large solid angle apparatus such as ours. Table 13.3 gives raw rates for detecting two leptons in the "barrel" of our detector and in the whole detector. Fig. 13.3 shows that our acceptance as function of the mass is fairly flat.

The W^{o} will appear very strikingly in the invariant mass spectrum of the two leptons. Its natural width is expected to be 1.2 GeV/c. When detected in electrons, our mass resolution will be 1.5% r.m.s., that is 1.2 GeV at 80 GeV. With muons, it will depend on the muon configuration and will be 7% on average.

Table 13.1

Efficiencies

	$40^\circ < \theta < 90^\circ$		$25^\circ < \theta < 40^\circ$		$5^\circ < \theta < 25^\circ$	
	Forward	Backward	Forward	Backward	Forward	Backward
Cut in $p_T > 20$ GeV	97%	84%	97%	69%	81%	47%
($p_T > 10$ GeV)	(100%)	(99%)	(99%)	(95%)	(94%)	(82%)
Cut in angle with respect to magnetic field	83%	83%	100%	100%	100%	100%
Efficiency of detection for μ	95%	95%	95%	95%	95%	95%
Total efficiency(*) $W^- \to \mu^- \bar{\nu}$	76% (79%)	66% (78%)	92% (94%)	66% (90%)	77% (89%)	45% (78%)
Efficiency of detection for e	80%	80%	80%	80%	80%	80%
Total efficiency(*) $W^- \to e^- \bar{\nu}$	64% (66%)	56% (65%)	78% (80%)	55% (76%)	65% (75%)	38% (66%)

(*) Numbers in brackets for $p_T > 10$ GeV cut which appears feasible with transverse energy imbalance cut.

Table 13.2

Rates for $\bar{p}p \to W^- + W$, $W \to e\bar{\nu}$

	$40^\circ < \theta < 90^\circ$		$25^\circ < \theta < 40^\circ$		$5^\circ < \theta < 25^\circ$		Total
	Forward	Backward	Forward	Backward	Forward	Backward	
Raw rates	62	110	9	46	2	60	289
$\bar{p}p \to W^- + X^{(*)}$, $W \to \mu\bar{\nu}$ measured in detector	47 (49)	72 (86)	8 (8)	30 (41)	2 (2)	27 (47)	186 (233)
μ background$^{(**)}$ $p_T > 20$ GeV	20	20	4.5	4.5	1.5	1.5	52
$\bar{p}p \to W^- + X^{(*)}$, $W \to e\bar{\nu}$ measured in detector	40 (41)	62 (71)	6 (6)	25 (35)	2 (2)	23 (40)	158 (195)
e background$^{(**)}$ $p_T > 20$ GeV	6.5	6.5	2	2	.5	.5	18

Integrated luminosity 10^{36} cm^2

$\sqrt{s} = 540$ GeV/c

Weinberg-Salam model $\sin^2\theta_W = 0.3$

(*) $p_T > 20$ GeV/c cut - numbers in brackets: $p_T > 10$ GeV/c cut.

(**) No transverse momentum imbalance cut!

Table 13.3

$W^0 \to \ell^+\ell^-$

	Barrel $25^0 < \theta < 155^0$		End cap + barrel $5^0 < \theta < 155^0$	
	2 leptons	1 lepton only	2 leptons	1 lepton only
$\bar{p}p \to W^0 + X$ $\quad \hookrightarrow \ell^+\ell^-$ raw rates	49 (62%)	26 (33%)	77 (97%)	2 (3%)
Rates with 90% efficiency	44 (56%)	23 (29%)	69 (87%)	2 (3%)

10^{36} integral luminosity

Figures in brackets are global efficiency

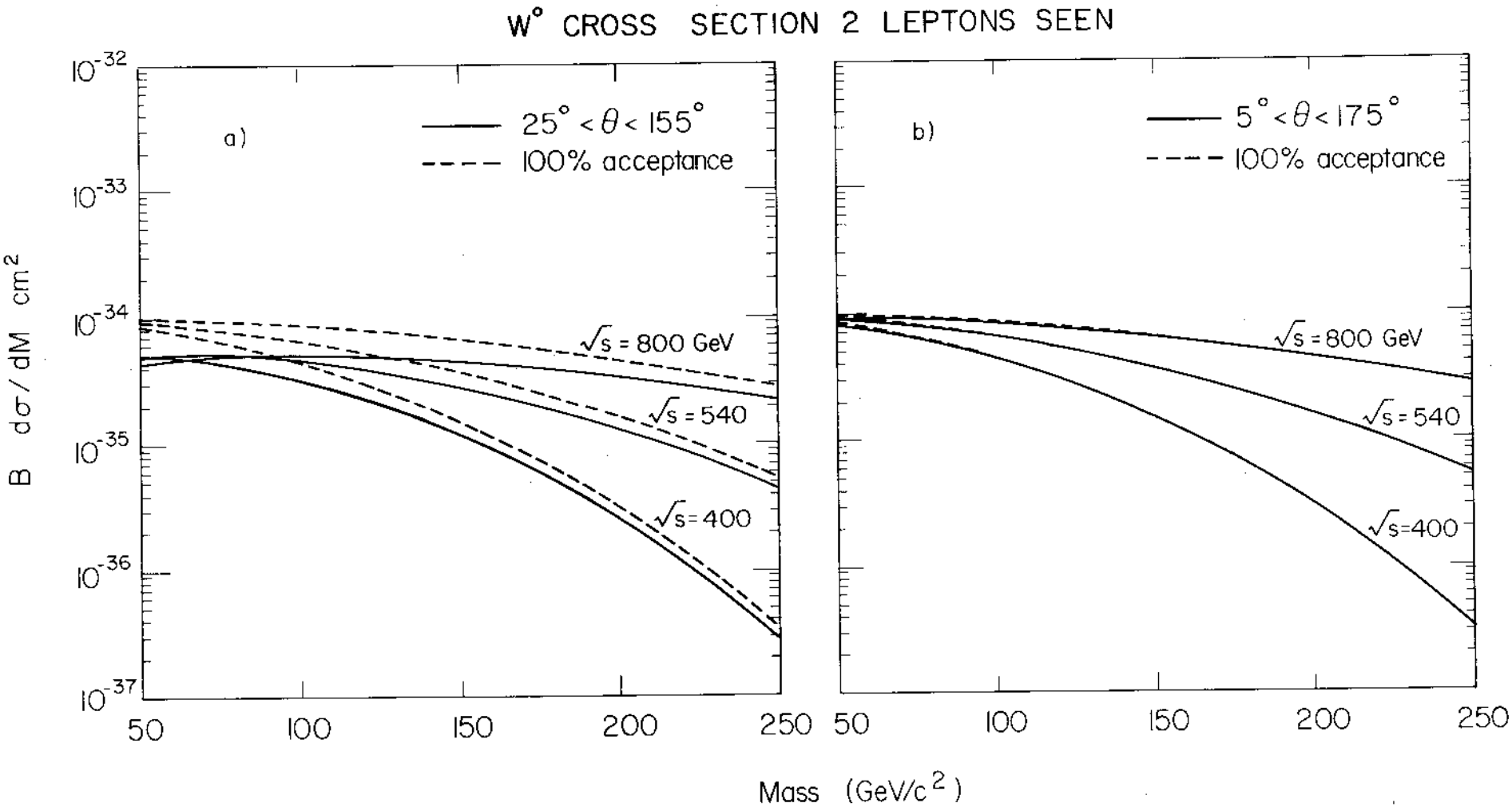

Figure 13.3. Acceptance of $W^0 \to e^+e^-$ as a function of its mass. Dashed lines give theoretical cross-sections with 100% acceptance. Full lines give experimental cross-sections:

a) For the 'barrel' part of our detector $25^o < \theta < 155^o$. b) For our complete detector $5^o < \theta < 155^o$.

There is obviously no problem of background from hadronic origin since two leptons are required. Drell Yan background is completely negligible (fig. 2.2). Only three events above 40 GeV/c^2 will be produced for 10^{36} cm^2 integrated luminosity. Massive vector mesons will also have the same experimental signature. Their cross section may be significantly smaller than that of the W^o if we believe the M^{-3} scaling law of Gaisser et al[43] (fig. 2.18 and table 13.4). The way to distinguish a W^o from an ordinary vector meson will be to observe a charge asymmetry. Unfortunately in the Weinberg-Salam model with $\sin^2\theta_w$ close to 0.25, the W^o coupling to electron is nearly axial and there is no asymmetry in the peak (fig. 2.5). Strong asymmetries will exist on the lower side of the resonance through interference with the Drell Yan amplitude. The rate may not permit detecting such an asymmetry.

Efficiencies will be similar or higher than those obtained for single leptons. Cuts on each individual lepton may be wider and the hole in the magnetic detection at 90^o is unimportant. Only a few percent of W^o will have the two leptons in this "hole" and when only one is in the bad region, the mass can still be reconstructed (neglecting the transverse momentum of the W^o). An efficiency of 90% is probably within reach. This leads to the rates shown in table 13.3.

We see that our detector has 87% efficiency for detection of a W^o of 80 GeV/c^2 giving 140 events total ($W^o \to e^+e^-$ and $\mu^+\mu^-$) for 10^{36} cm^2 integrated luminosity. A W^o of 150 GeV/c^2 will have a rate roughly two times smaller. These rates show that even if we are wrong in our theoretical expectations by a factor 10 or if the collider misses its design luminosity by the same factor 10, we have a good chance to detect the W^o if it exists below 150 GeV/c because of our good resolution and the very low background.

13.4 Hadronic decays of W's

The hadronic decay rates of W^o are roughly twenty times larger than those quoted in table 13.3. With these channels we are operating of a total of 4500 events for 10^{36} cm^2 integrated luminosity.

We expect a resolution on the W mass of 3.2 GeV/c^2 r.m.s. It is completely dominated by confusion between slow particles in the jet and ordinary beam fragments[19].

Table 13.4

Massive vector meson rates

	$V \to \ell^+\ell^-$	
Mv	Bv Ev	$\int \mathcal{L} = 10^{36}$
9.5	$6\ 10^{-33}$	5400
15	$1.5\ 10^{-33}$	1350
30	$1.9\ 10^{-34}$	171
70	$1.5\ 10^{-35}$	13

Assumptions:

- scaling according $\frac{1}{M^3}$ [43],
- cross section flat over 6 units of rapidity,
- 90% dilepton efficiency.

Table 13.5

Jet cross section and rate above given p_T

p_T	σ_{jet} $p_T^{jet} > p_T$	Probability both jets in apparatus	Rates for 10^{36} cm^2
5	$1.2\ 10^{-29}$	87%	10^7
10	10^{-30}	97%	10^6
15	$1.9\ 10^{-31}$	100%	$8\ 10^5$
20	$4.7\ 10^{-32}$	100%	$5\ 10^4$
30	$5.4\ 10^{-33}$	100%	$5\ 10^3$
40	$8\ 10^{-34}$	100%	$8\ 10^2$

However, as shown in fig. 2.7. the signal to background may be of the order of 1 and we will have to rely on the large number of events, on the presence of charmed and strange particles or on parity violation to single out the signal.

Even if this does not allow a proof of the existence of the W's, which will probably come from their leptonic decays, it can give their branching ratio into leptons. This counts the number of quarks and heavy leptons of mass smaller than the W.

13.5 Hadronic jets

Fig. 13.4 and table 13.5 give the estimate obtained with a vector gluon model [19] for rates above a given p_T. If such a p_T^{-4} component exists, our detector will be able to explore jet production up to 40 GeV/c with still several hundred events.

13.6 Conclusion

We have shown that our detector is well suited to the study of large p_T jets and to the search for W mesons. Its large solid angle gives a very high efficiency of detection. Moreover, its excellent lepton rejection, and its measurement of energy on more than six units of rapidity allows us to suppress background in lepton decays of the W and study very efficiently asymmetries which are biggest at relatively low p_T.

We would like to stress finally that we have designed our detector not only to have excellent efficiency for large angle physics. The choice of a dipole allows us to cover more than six units of rapidity (9 with forward detectors). Its good pattern recognition features and the complete measurement of energy flow over all this energy region will allow us to study very rapidly any surprise which may show up at the $\bar{p}p$ collider energy.

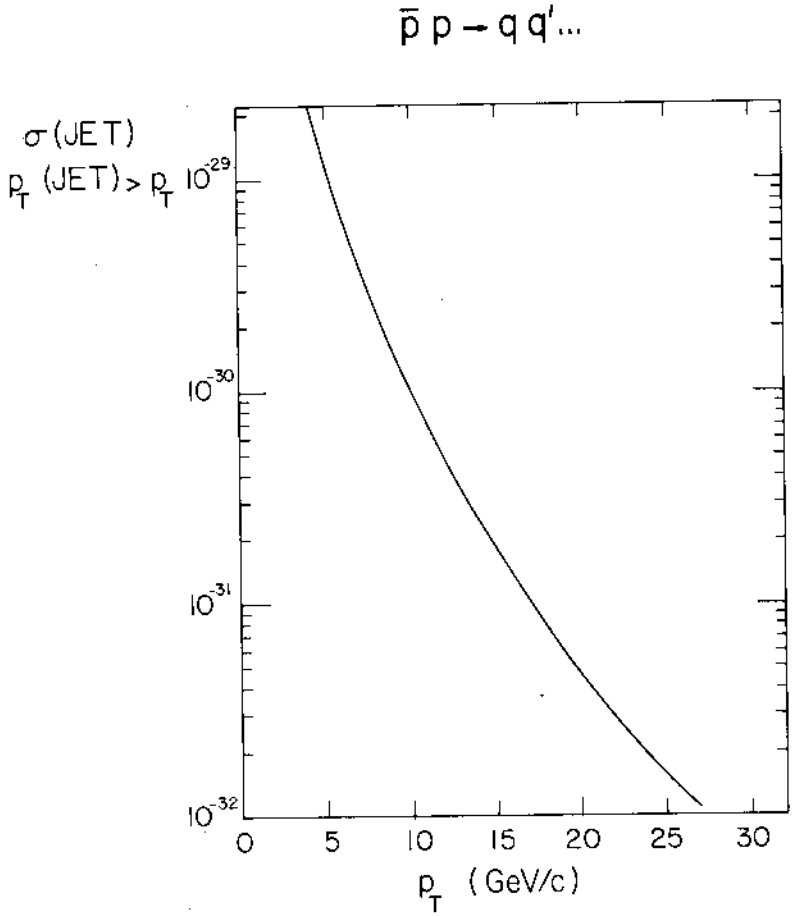

Figure 13.4. Integral cross-section for hadronic jets above given p_T.

14. Interaction with the SPS

14.1 Running time

We are fully aware that the $\bar{p}p$ collider programme represents a burden for other SPS users. On the other hand, its fundamental physics interest deserves a reasonable but significant amount of machine time. We propose that 20% of the available machine time is allocated to the $\bar{p}$ physics programme, that is about 1 000 hours per year, starting mid 1980 (500 hours in 1980 mainly for setting-up).

The distribution of this time is still an open question. Clearly one would like to match, if at all possible, the production time of $\bar{p}$ and the luminosity lifetime in order to be able to run continuously with $\bar{p}$ during complete periods. This will minimize setting-up times and maximize our physics output.

14.2 Assembly and maintenance

When designing our apparatus, we tried to minimize disturbances to SPS normal or collider operation. In particular we have attempted to simplify the assembly and the maintenance of the detector as much as possible.

(a) Assembly and major repairs

It is clear that the assembly and debugging of the detector is a major operation which, if done in the SPS tunnel, will require painful shutdowns. We propose, therefore, to be able to roll the experimental apparatus in and out of the SPS tunnel within a few days (Ref. 1, 2). This would require an assembly hall to be dug close to the experimental area and at the level of the tunnel. One could then visualize the operations as follows.

- When the detector is out of the SPS tunnel, proper shielding would allow work to be carried out in the assembly area. This would be extremely useful for the assembly and the initial debugging of our equipment. The detector could also be stored there during normal SPS cycles, allowing additions and major repairs to be done, and subtracting it from heavy irradiation.

- During the $\bar{p}$ periods, the detector could be rolled in. Only a minimal amount of shielding is necessary and this may allow us to locate our electronics racks fairly close to the detector and still have continuous access to them.

We are discussing the technical problems involved with Mr G. Brianti and his collaborators. If this scheme is adopted the apparatus will have to carry its own section of beam pipe with the necessary valves. We are studying problems related to connections of signal cables.

In particular we are investigating ways of minimizing their number (multiplexing), making them very flexible or easy to disconnect.

If this solution of rolling the detector in and out cannot be adopted for technical or financial reasons, our detector is modular enough to be assembled in place relatively quickly (presumably after an initial assembly outside). Essentially C's will be completely equipped with scintillators and thoroughly tested before being lowered down into the SPS tunnel and installed.

(b) Maintenance

When the detector is in the SPS tunnel, we will have to maintain our equipment within very limited controlled access periods. In order to minimize the complexity of our interventions we have decided to follow the following principles.

- Maximum use of passive elements. Note that the C's and the "gondolas" are essentially passive and we do not see what could break down in their mechanical structure once they are installed. Sensitivity to radiation of the scintillators is also very small.

- Easy access and standardized elements. Phototubes are easily accessed because they are located outside the magnet. In order to reach the central detector, the two halves of the magnet will have to be moved apart. This could be done with proper design within, say, less than one hour. Preamplifiers or capacitors which will sit on the central detector can then be exchanged. We will attempt to minimize sense wire breaking through proper design (e.g. 40μ diameter) and electrical protection (tripping circuits). In the event of this happening, we could

take out the broken wire by its two extremities and go on running. In case of more severe damage, the relevant section of the detector could be exchanged with a spare section already flushed with the proper gas and running can be resumed immediately after the intervention.

- Redundancy. We have a large number of separate cells in our detector and, if necessary, we can go on running even if one "gondola" is dead or a few wires are not working.

14.3 Civil engineering requests

It is obviously much too early to put forward detailed requests in terms of experimental area and assembly hall, and particularly before the feasibility of assembly hall at tunnel level is fully studied. However, in order to fix ideas, we could quote the following numbers.

(a) Experimental area

Minimum length	12.5	m
Minimum height	9	m
Minimum width	12	m in order to be able to open the magnet and not to block the passage.

A $\geq$ 4 m diameter tunnel at 90^{o} on one side would be very useful for the full instrumentation of one 90^{o} window.

The total weight of the detector is 1500 t. Only limited lifting capability (a few tons) is necessary if there is an adjacent assembly area.

(b) Assembly area

Whether or not this is combined with the experimental area, its horizontal dimensions should be significantly bigger (by at least 3 m) than the dimensions quoted above, in order to have room to dismantle the apparatus.

We would need a crane of 60 tons since individual C's weigh $\sim$ 55 tons. End caps (270 tons per side) will also be segmented appropriately.

14.4 Compensation and low beta section

As discussed in section 4, we will build compensating magnets for our detector. They will turn on synchronously with the main magnet at the running energy. Effect on betatron functions and tunes will be admissible.

Our experiment requires as low β as feasible at the interaction point in order to maximize the luminosity. Note that at least initially, we will not occupy the 28 m presently planned between the quadrupoles and it may be advantageous to bring them closer, to be able to reach lower values of β.

Finally our detector is not very sensitive to the exact length of the interaction region if it is below 1 m.

14.5 Vacuum and background

In order to keep the beam gas interactions at a reasonable level, we estimate that the local vacuum in the beam tube should be kept at 10^{-10} torr over $\pm$ 25 m around the interaction region.

In addition, the limiting aperture of the machine should be located far from the interaction region and special care should be taken (even during normal SPS running) not to irradiate the interaction area too much.

REFERENCES

[1] C. Rubbia, P. McIntyre and D. Cline: "Producing massive neutral intermediate vector bosons with existing accelerators". Proceedings of the International Neutrino Conference, Aachen 1976, H. Faissner, H. Reithler and P. Zerwas, editors p. 683.

[2] F. Bonaudi, S. Van der Meer and B. Pope: "Antiprotons in the SPS" CERN/DG-2, 11 January 1977.

[3] S. Van der Meer et al., Report in preparation.

[4] C. Rubbia: "Luminosity lifetime due to beam-gas scattering". CERN-$p\bar{p}$ Note, Oct. 27, 1977.

[5] T. Wilson, to appear in Ref.[2].

E. Keil, Private communication;

R. Billinge et al., CERN/ISR/ES/GE/GS-76-50;

A. Hutton, CERN/ISR/TH 77-66.

[6] C. Rubbia: "Luminosity estimates for SPS as a $p\bar{p}$ collider" CERN-$p\bar{p}$ Note 35, Oct. 26, 1977.

[7] F. Halzen: "Hadron collisions above 10 TeV or guessing particle physics at New Accelerators". Invited talk at the VIIth International Colloquium on Multi-particle Reactions, Tutzing, Germany (June 1976).

[8] M. Gell-Mann, Rev. Mod. Phys. 31 (1959) 834.

[9] High energy neutrino experiments have set a limit of > 20 GeV for any non locality at the vertex. See for instance D. Cline in Proceedings of 1977 International Syposium on Lepton and Photons, Hamburg, Germany (Aug. 1977).

[10] See for instance P. Musset in Proceedings of 1977 International Symposium on Lepton and Photons, Hamburg, Germany (Aug. 1977)

[11] A. Salam, "Elementary Particle Theory" edited by N. Svortholm, 1968 page 367 and S. Weinberg, Phys. Rev. Letters 13 (1967) 1264.

[12] See for instance J. Bjorken in Proceedings of Summer Institute on Particle Physics, August 2-13, 1976. SLAC, Report No 198. Also R.M. Barnett, in "Particle and Fields 76", Proceedings APS/DPF conference Brookhaven BNL 50598 (1976).

[13] G. Quigg, Rev. Mod. Phys. 49 (1977) 297;

F. Halzen, Wisconsin preprint COO-573 (Oct. 76);

M. Chase and W.J. Stirling, unpublished;

P.V. Landshoff: "Parton physics and hunting the W with hadron beams", In Proceedings Varenna Summer School, July 1977 (North Holland Publisher).

R. Palmer et al., Phys. Rev. D14 (1976) 118;

J. Finjord, Nordita preprint 76/22 (1976);

Yu. A. Golukhov et al., Soviet J. Nucl. Phys. 18 (1979) 203.

Okun-Voloshin, ITEP preprint 111 (1976) see also refs [1] and [18].

[14] I. Hinchcliffe and C.H. Llewellyn Smith, Oxford University, Theoretical Physics Preprint 36/77 (1977).

[15] J. Ellis and M.K. Gaillard, CERN 76-18, Yellow Report, p. 65 (1976), see also ref. [13].

[16] B. Sadoulet, CERN-$p\bar{p}$ Note 47 (1978).

[17] D. Linglin, CERN-$p\bar{p}$ Note 17 (1977).

[18] R.F. Peierls et al., Phys. Rev. 16 (1977) 1397.

A. Kernan, CERN-$p\bar{p}$ Note 29, (1977).

[19] M. Della Negra, CERN-$p\bar{p}$ Note 43 (1978).

[20] A.P. Linde, JETP Letters 23 (1976) 73;

S. Weinberg, Phys. Rev. Letters 36 (1976) 294

[21] H. Georgi et al., Harward Preprint, HUTP-77/A084 (December 1977).

[22] C. Rubbia, CERN-$p\bar{p}$ Note (1978).

[23] R. Blankenbecler, S.J. Brodsky and F.J. Gunion, Phys. Letters 39B (1972) 649 and Phys. Rev. D6 (1972) 2652;

S.M. Berman, J.D. Bjorken and J.B. Kogut, Phys. Rev. D4 (1971) 3388;

S.D. Ellis and M.B. Kislinger, Phys. Rev. D9 (1974) 2027.

A. Kernan, CERN-$p\bar{p}$ Note 29 (1977);

M. Jacob, CERN-$p\bar{p}$ Note 25 (1977).

[24] For a recent summary see for example P. Darriulat: "Large Transverse Momentum Hadronic Processes", Tbilissi talk, 1976, and G.C. Fox, "Proceedings Particles and Fields" 1976, Brookhaven.

D. Sivers, S. Brodsky and K. Blankenbecler, Phys. Reports 23C (1976) 1.

[25] R.F. Peierls, T.L. Trueman and L.L. Wang, "Estimates of Production Cross sections and Distributions for W-Bosons and Hadronic Jets in High Energy pp and $p\bar{p}$ Collisions", BNL-22628.

[26] R.D. Field and R.P. Feyman, Phys. Rev. D15 (1977) 2590.

[27] S. Pakvasa, D. Parashar and S.F. Tuan, Phys. Rev. D10 (1974) 2124.

[28] See for example S.J. Brodsky and J.F. Gunion, Proceedings of the VII International Colloquium on Multiparticle Reactions, Tutzing, Germany (1976), and SLAC-PUB-1820 (1976).

[29] J.D. Bjorken, SLAC-PUB 1756 (1976);

A. Casher, J. Kogut and L. Susskind, Phys. Rev. Letters 31 (1937) 792.

[30] R.P. Feynman: "Quark Jets", invited talk at the VIII International Symposium on Multiparticle Dynamics, June 1977, and R.P. Feynman and R.D. Field, paper in preparation.

[31] S.J. Brodsky: "Jet Production and the Dynamical Role of Colour", Proceedings of the 1977 Rencontre de Moriond;

S.J. Brodsky and N. Weiss: "The Retention of Quantum Number by Quark and Multiquark Jets", SLAC-PUB 1926 (1977).

[32] M. Jacob: "Hadron Physics at the $p\bar{p}$ Collider", CERN-$p\bar{p}$ Note 01 (1977);

P.V. Landshoff, CERN Preprint TH 2227 (1976)

[33] C. Bromberg et al., Phys. Rev. Letters 38 (1977) 1447.

[34] S. Pokorsky and L. Van Hove, Nucl. Phys. B86 (1975) 243.

[35] G.L. Klane: "Gluon Interactions on Hadron Physics at Isabelle" UM-HE-77-45, University of Michigan, Preprint, 1977;

G.L. Klane and York-Peng Yao "Studying Gluon Properties Experimentally", UM-HE-77-44, University of Michigan, Preprint 1977.

[36] L. Lederman, Proceeding of the EPS Conference, Budapest, July 1977.

[37] C. Quigg, Rev. Mod. Phys. 49 (1977) 297.

[38] H. Fritzsch and P. Minkowski, CERN Preprint TH 2400, Oct. 1977

[39] F. Halzen and S. Matsuda, "Hadroproduction of Quark Flavors", CERN Preprint TH 2354.

[40] A. Donnachie and P.V. Landshoff, Nucl. Phys. B112 (1976) 233.

[41] M.J. Corden et al., Phys. Lett. 68B (1977) 96.

[42] J.H. Cobb et al., Phys. Lett. 68B (1977) 101.

[43] T.K. Gaisser, F. Halzen and E.A. Paschos, Phys. Rev. D15 (1977) 2572.

[44] W. Willis et al., to be published.

[45] M. Jacob, private communication.

[46] W. Thomé et al., Nucl. Phys. B129 (1977) 365.

[47] U. Amaldi et al., Phys. Lett. 66B (1977) 390;
G. Matthiae, CERN-$p\bar{p}$ Note 12 (1977).

[48] K. Guettler et al., Phys. Lett. 64B (1976) 111.

[49] G.B. Yodh, "Unusual Interactions above 100 TeV: A review of cosmic ray experiments with emulsion chambers, invited talk, Brookhaven Symposium on Prospects of Strong Interaction Physics at Isabelle (April 1977).

[50] L. Baksay et al., Phys. Lett. 61B (1976) 89.

[51] See for example F.S. Hengey and J. Pumplin, Nucl. Phys. B117 (1976) 337.

[52] M. Della Negra et al., Phys. Lett. 65B (1976) 394.

[53] H. De Kerret et al., Phys. Lett. 68B (1977) 385.

[54] Experimental Studies of double-pomeron exchange are reviewed by A. Kernan, Proceedings of the XII Rencontre de Moriond, vol.II, p. 87.

[55] F.E. Low, Proceedings of the XII Rencontre de Moriond, vol. III, p. 135.

[56] J. Ellis, ISR Discussion Meeting 22, 18 May 1977.

[57] C.M. G. Lattes et al., Proceedings of the 13th International Cosmic Rays Conference, Denver 1973, Vol. 4, p. 2671.
C.M.G. et al., Proceedings of the 14th International Cosmic Rays Conference, Munich 1974, Vol. 7, p. 2387.

[58] H. Ali et al., Proceedings 1960, Rochester Conference, p. 829.

[59] Brazil-Japan Emulsion chamber collaboration, Proceedings Hobart Conference on Cosmic Radiation (1971) 2773 and C.K.J. Report 13, Tokyo (1974).

[60] V.S. Aseikin et al., in Proceedings Moscow Conference on Cosmic Radiation (Oct. 1974) in press.

[61] R. Wilson, CERN-$p\bar{p}$ Note, to be published

[62] B. Sadoulet CERN-$p\bar{p}$ Note 11 (1977)

[63] P. G. Innocenti, G. Salvini, P. Strolin, "The magnetic field", report at the 2nd $p\bar{p}$ study week (July 1977)

[64] Original idea due to C. Rubbia; for details see Ref. 72

[65] W. B. Atwood et al., Preprint SLAC TN-76-7 (1976)

[66] C. Rubbia and G. Salvini CERN-$p\bar{p}$ Note 41 (1977)

[67] B. Barish et al., Preprint, CALT 68 - 623

[68] C. Rubbia, CERN-$p\bar{p}$ Note 38 (1977)

[69] Some recent developments in computation of two-dimensional fields in iron magnets. C. Iselin Proceedings 3rd International Conference on Magnet Technology, Hamburg (May 1970)

[70] Selection of formula concerning proton storage rings, G. Guignard CERN 77-10, (June 1977)

[71] SPS low-beta for use with MISR. P. J. Bryant, E.N.J. Wilson, private communication

[72] Experimental results on drift chambers with image readout, CERN-$p\bar{p}$ Note 45, to be published.

[73] A short study of the charged coupled device CCD 321, P. Davies, B. Hallgren and H. Verweij, CERN-$p\bar{p}$ Note 31, (June 1977)

[74] Electronics for central detector, C. Rubbia, CERN-$p\bar{p}$ Note 44, to be published

[75] R606 technical paper on multi-sense wire chambers, to be published

[76] a) Comments on charged particle detectors for the $p\bar{p}$ large solid angle detector, B. Sadoulet, CERN-$p\bar{p}$ Note 16, (June 1977)
b) Space charge effects in projection chambers, B.Sadoulet and F. Sauli, CERN-$p\bar{p}$ Note 46, to be published

[77] Uncertainties in track momentum and direction due to multiple scattering and measurement errors, R. L. Gluckstern, NIM 24 (1963) 381.

[78] G. Salvini, CERN-$p\bar{p}$ Note 40